UNIVERSITY OF NAIROBI

UTILIZATION OF KWALE ILMENITE ORE IN PRODUCTION OF

REFRACTORY FIREBRICKS

BY

MAKOKHA JOHN WANJALA

I56/64538/2010

Thesis Submitted to the Board of Postgraduate Studies for Examination in

Partial Fulfillment of Requirements for Award of the Degree of Master of

Science in Chemistry of the University of Nairobi

2015

Declaration

I declare that this thesis is my original work and has not been submitted elsewhere for examination, award of a degree or publication. Where other peoples work, or my own work has been used, this has properly been acknowledged and referenced in accordance with the University of Nairobi's requirements.

Signature.. Date..03/09/2015

Makokha John Wanjala

I56/64538/2010

Department of Chemistry

University of Nairobi

This thesis was submitted for examination with our approval as research supervisors

	Signature	Date

Prof. D.K. Kariuki   07/09/2015

Department of Chemistry

University of Nairobi

P.O. Box 30197-00100, Nairobi, Kenya.

kkariuki@uonbi.ac.ke

Mr. Gitobu Paul Mwitari   3/9/2015
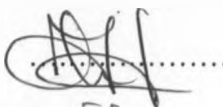
Research Technology & Innovation Department

Kenya Industrial Research & Development Institute

P.O. Box 30650-00100, Nairobi, Kenya.

pmwitari@gmail.com

Dedication

This thesis is dedicated to my beloved family and parents for their steadfast support throughout my studies.

Acknowledgements

Abstract

In this study, Kwale Ilmenite Ore, Eburru Kaolin, Eburru Fireclay and Mukurweini Ball Clay were used to formulate refractory firebricks for incinerator internal lining. The effects of particle size distribution, water to binder to grog ratio, curing and Kwale Ilmenite Ore on the compressive strength, bulk density and apparent porosity of firebricks were investigated.

Atomic Absorption and X-Ray Diffraction Spectrophotometric analysis were used to determine the elemental oxide and mineral phase composition of the samples respectively. 2.5 % iron III oxide by weight was used as the basis for formulation of grog and binder. 100 parts Eburru Kaolin, 100 parts Eburru Fireclay and 33 parts Mukurweini Ball Clay was used as the grog formulation while 3 parts of Mukurweini Ball Clay and 2 parts of Eburru Kaolin was used for binder formulation. % Kwale Ilmenite Ore, particle size distribution, grog to binder ratio, % water and curing were varied in formulations. The firebricks were pressed at 50 tons with a hold time of 1 minute, dried away from direct sunlight for 3 days, fired at 1200 ^{O}C for 12 hours and cooled to 24 ^{O}C for 48 hours in the furnace. The compressive strength at room temperature, bulk density and apparent porosity were determined for different formulations.

Eburru Kaolin was found to contain 24.74% Al_2O_3, 72.64 % SiO_2 and 0.71% iron III oxide; Eburru Fireclay 26.63% Al_2O_3, 66.40% SiO_2 and 2.78% Fe_2O_3; Mukurweini Ball Clay 36.85% Al_2O_3, 55.38% SiO_2 and 3.86% Fe_2O_3 and Kwale Ilmenite Ore 44.60 % TiO_2 and 53.20 % Fe_2O_3. 2 parts of Kwale Ilmenite Ore, 43 parts of Mukurweini Ball Clay, 100 parts of Eburru Kaolin and 100 parts of Eburru Fireclay by dry weight produced firebricks with optimal chemical composition 27.53 % Al_2O_3, 65.87 % SiO_2, 3.43 % TiO_2, 2.08 % Fe_2O_3 and 1.09 % others. Particle size distribution of 2 parts coarse, 1 part medium and 2 parts fines, water to grog to binder ratio of 7:13:30 by weight gave the optimal bulk density, compressive strength at room temperature and apparent porosity of 1. 64g/cm^3, 20.0 N/mm^2 and 36.87 % respectively. 3.43% Kwale Ilmenite Ore formulated firebricks gave optimal bulk density, compressive strength and apparent porosity of 1.59g/cm^3, 20.6N/mm^2 and 36.45% respectively. The compressive strength increased from 20.0 to 20.6N/mm^2 and apparent porosity reduced from 3.87% to 3.45 %. This was attributed to the presence of Kwale Ilmenite Ore in the formulation.

Table of Contents

List of Tables

List of Figures

Abbreviations, Acronyms and Symbols

Abbreviations

AE: Acoustic Emission

AU: Acousto Ultrasonic

GDP   : Gross Domestic Product

IPCC   : Intergovernmental Panel on Climate Change

LDS (%): Percentage Linear Drying Shrinkage

LFS (%): Percentage Linear Firing Shrinkage

LOI: Loss on Ignition

MTP   : Medium Term Plan

MTS: Mori Tanaka Scheme Theory.

NDE: Non Destructive Evaluation.

NF: Near Field Distance.

PCE: Pyrometric Cone Equivalent

PM: Particulate Matters

SCS: Self-Consistent Scheme Theory

US: Ultrasonic Testing.

VOC: Volatile Organic Compounds

WA (%): Percentage Water Absorption

Symbols

D_{size}: Average grain size

D : Diffusion coefficient ($m^2 s^{-1}$)

C_m : Concentration solubility (gm^{-3})

C_s : Saturation solubility (gm^{-3})

δ : Effective boundary layer thickness (m)

J : Dissolution rate

D_{size}: Grain size

σ : Strength

E : Young's modulus of a porous specimen

E_0 : Young's modulus of a fully dense specimen

[E] : Intrinsic modulus

G : Shear modulus of a porous specimen

G_0 : Shear modulus of a fully dense Specimen

K : Bulk modulus of a porous specimen

K_0 : Bulk modulus of a fully dense specimen

K_{ic}:   Fracture of toughness

P   :   Pore volume fraction

P   :   Volume fraction porosity

P_{crit}: Critical Porosity

V   : Ultrasonic velocity

V   :   Longitudinal ultrasonic velocity

V_s :   Shear ultrasonic velocity

α :   Aspect ratio

σ :   Modulus of rupture of a porous specimen

σ_0 :   Modulus of rupture of a fully dense specimen

ρ :   Bulk density

υ :   Poisson's ratio

ξ :   Porosity interaction coefficient

Chapter 1

INTRODUCTION

1.1 Background

Refractory firebricks are ceramic materials that withstand high melting temperatures while maintaining their structural properties. They also prevent equipment corrosion and resist destructive influences such as abrasion, rapid changes in temperature and pressure, corrosion by slags and fluxes, erosion by molten slags, withstand load at service conditions, resist contamination of the material with which it comes into contact, maintain sufficient dimensional stability at high temperature after or during repeated thermal cycling, conserve heat et cetera [Chukwudu, 2008].

Refractory firebricks are vital for the manufacturing industry. They are used as lining in high temperature applications such as kilns, furnaces, ovens, incinerators etc. Currently, Kenya spends approximately 3 billion shillings annually to import refractories mostly from India and China for its cement, metal smelting and sugar processing industries [Kenya Institute of Public Policy and Research Analysis, 2013]. The historical trends of trade in Kenya show that Kenya still imports 100 % firebricks since independence, despite availability of raw materials and technology, to sustain its manufacturing industrial sector. According to Kenya Central Bureau of Statistics, 2014, Kenya has a potential of cutting down firebricks imports to 20% and increase exports by 15 % in a span of 10 years.

Ceramic Production Industry is one of the underperforming industries in Kenya, with almost zero annual production [Kenya Central Bureau of Statistics, 2014]. The existing Ceramic Industries in

Kenya are distributors of imported ceramic wares. Advancement of Ceramic Technology in Kenya is being pioneered by Kenya Industrial Research and Development Institute at its Ceramic Pilot Plant Laboratory. One important characteristic of the Ceramic Industry is that it is basic to the successful operation of many other industries. For example, refractory firebricks are a basic component of Metallurgical and Cement Processing Industries [Krishna et al, 2013].

The main consumers of the firebricks in Kenya are Cement, Sugar, Incineration and Metal Processing Industries. East African Portland Cement alone consumes approximately 1200 tons of firebricks annually for production of cement [Government of Kenya, Ministry of Industrialization, 2013].   The waste incineration consumption currently is approximated at 450 tons annually. The demand of refractory firebricks is bound to increase tremendously owing to the increased growth of Kenya's manufacturing sector [World Bank, 2013]. The boom in the building and construction industry in Kenya has led to increased volume of utilization of cement and consequently increasing demand on firebricks. The current requirement by the Government of Kenya of every hospital and county to have an incinerator will also see the demand of firebricks go up. Production of firebricks in Kenya will catalyze achievement of Vision 2030 [Government of Kenya, Ministry of Industrialization, 2013].

The principal raw materials used in the production of firebricks are Al_2O_3-SiO_2 clays. Rarely do single raw material meet the desirable ceramic properties, hence a range of raw materials are utilized to achieve desirable chemical composition of the refractory firebricks [Harbison, 2005]. The raw materials used in formulation of firebricks are generally clays of kaolin family. According to the Ministry of Environment and Natural Resources, [2006], Kenya is endowed with vast deposits of kaolin, fireclay and ball clays that can be exploited for production of firebricks. The kaolin and fireclay are found in Nakuru County at Eburru Complex while the Ball

2

Clays are found in Nyeri County in Mukurweini sub-county. There has been no economical utilization of these clays locally [Government of Kenya, Ministry of Environment and Natural Resources, 2006].

Ball clays are fine grained, highly plastic with a kaolinite structure. These clays are often referred to us plastic clays because they possess great plasticity and are chiefly used in ceramic mixes to improve plasticity [Grimshaw, 1991]. They contain up to several weight percentage of decayed biological organic matter and as such, they are commonly dark in color. Mineralogical and chemical differences between ball clays and kaolin are minor since both are kaolinitic in nature, containing quartz as the major impurity and Fe_2O_3 as minor impurities [Matsui et al, 1991]. Localized seams in the same deposits have variations in composition including the quantity of the major mineral, accessory minerals and carbonaceous materials such as lignite. Their primary role is to impart plasticity and aid rheological stability during the shaping process.

1.1.1. Production

There are three main firebrick manufacturing processes: soft mud, stiff mud and dry press method. In the stiff mud process water in the range of 10 to 15 % is added into the clay to produce plasticity while in the soft mud process clays are mixed with too much water above 30% to be extruded by stiff-mud process. In the dry press method, clays are mixed with less than 10% water [Harbison, 2005]. Most firebricks are made from blends of two or more clays. The visible inorganic and organic extraneous matters are removed first. The clays are then taken through beneficiation process where they are dissolved in water and free SiO_2, Fe_2O_3, K_2O and Na_2O are reduced. Fe_2O_3, K_2O and Na_2O dissolve in water while SiO_2 being dense is separated by gravity method. This process leads to Al_2O_3 increase and drastic reduction of Fe_2O_3, K_2O and Na_2O. The

clays can then be mixed in appropriate mixing ratio and used to produce grog that aids the firebrick in withstanding thermal stresses during firing [Rahman, 2012].

Production of refractories requires utilization of chemically controlled raw materials, processing and fabrication parameters in order to achieve desired physical, mechanical and chemical properties. Refractories are composed of thermally stable inorganic mineral aggregates, a binder phase and additives to enhance certain mechanical properties. The main types of refractories are firebricks castables, ceramic fiber and insulating bricks that are made in varying combinations and shapes for diverse applications [Gandi et al, 1979].

In production of firebricks, particles of ground clay must include a range of graded sizes, each in appropriate proportion. The clays are typically ground in a dry pan, which is a rotating pan-shaped grinding mill having slotted openings in the bottom. The batches are screened to the desired sizes and thoroughly mixed with binder and a small but closely controlled amount of water. Normally, firebricks are processed by dry method where the raw materials are mixed directly with deionized water to produce a homogenous plastic body. In some cases, the homogenous mixture is allowed to age. Aging refers to change in rheology and plasticity within the body leading to change in particle–particle interactions which helps to distribute moisture evenly through the body. The moistened batch is then fed to a mechanically or hydraulically operated press in which the brick is formed under pressure [Matsui et al, 1991].

In a modification of power-press process, certain physical properties are enhanced by the application of high vacuum during the forming of the brick. Firebricks made this way typically have a more homogenous texture and are harder, stronger, less porous and denser than those made without a vacuum. As a consequence they are more resistant to impregnation and corrosion

by slags and penetration by gasses [Reed, 1987]. In making extruded firebrick, clays are ground in a dry pan, mixed wet or dry, brought to proper consistency in a pug mill, and extruded through the die of an auger machine in the form of a stiff column. The air is removed from the clay before extrusion by a Dearing system within the auger machine chamber. The column is cut into brick by means of wire. The firebricks are then typically repressed to give them sharp corners and edges and smooth surfaces. Many intricate special shapes are formed in vertical piercing-and-forming presses, in which blanks from the extrusion machine are completely reshaped [Kingery et al, 1991].

Firebricks formed by any of the processes described above are dried in tunnel or humidity driers and fired. The rate of heating, peak temperatures, soaking time and the atmosphere in the kiln affect chemical reactions and the microstructural development in the ceramic body and consequently are important in the processing of firebricks. The temperature of firing depends upon the maturity temperatures of the clays, and often upon the service for which the firebricks are intended. In firing the firebrick, several necessary ends are accomplished, these include free and combined water are driven off, iron and sulfur compounds and organic matter are oxidized, and gasses formed are eliminated, mineral transformations and changes in volume are effected, and finally, the particles of clay are ceramically-bonded together into mechanically strong brick [Reed, 1987].

The most versatile and consumed refractories in the industry are firebricks. They comprise about 75 % of the production of refractories on a volume basis globally and are essentially alumina-silicates with minor proportions of other minerals. As defined by the American Society for Testing Materials, ASTM [Chukwudu, 2008], there are generally five standard classes of

5

firebricks; these are super-duty, high-duty, medium-duty, low-duty and semi-silica as shown in Table 1 below.

Table 1: Classification of Firebricks

Brick	%SiO_2	% Al_2O_3	% of other Constituents	PCE (^{O}F)
Super duty	49-53	40-44	5-7	3175-3200
High duty	50-60	35-40	5-9	3075-3175
Medium duty	60-70	26-36	5-9	2975-3075
Low duty	60-70	23-33	6-10	2770-2900

[Source: Harbison, 2005]

The Al_2O_3-SiO_2 content influences the pH of the firebrick and determines the application environment of the firebricks [Reed, 1987].

1.1.2. Properties of Firebricks

An understanding of properties of refractories is fundamental to the development, improvement, quality control and selection of linings for high temperature applications. Various applications of refractory materials in different types of industries require diversified properties to meet the physico-chemical and thermal requirements at different phases of uses. In some industrial units more than one phase are present e.g. in steel-making vessels slag /metal /gases are simultaneously present in the vessel at high temperatures. In the heat treating furnaces solid/reducing or oxidizing gases are simultaneously present [Chukwudu, 2008].

Chemical composition, bulk density, apparent porosity, apparent specific gravity and strength at ambient temperatures are used as control parameters in the manufacturing and quality control process. The elemental oxide and phase composition of the clays and firebricks can be

determined by the X-ray diffraction analysis. X-ray diffraction method works with the principle that every crystal has characteristic diffraction angle of incident rays that gives the method its versatility. These parameters determine applicability of the final end product. The chemical composition serves as a basis for the classification of firebricks, while density, porosity and strength for quality evaluation of the brick. Bulk density and apparent porosity are determined by the boiling water method. This method assumes that when the firebrick is boiled in water for a period of not less than two hours, all the pores will absorb water. The soaked weight, suspended weight and dry weight are related and can be used to determine apparent porosity and bulk density, see equations 2.38 and 2.39. Bulk density, apparent porosity and strength are affected by the type and quality of raw materials, the size and the fit of the particles, moisture content at the time of pressing, pressure at mold, temperature, duration of firing and the rate of cooling. A product's room temperature strength is an important indicator of its ability to withstand abrasion and impact in low temperature applications and to withstand handling and shipping [Harbison, 2005].

The strength of firebricks at ambient temperatures may provide little or no indication of their strength at furnace operating temperatures [Matsui et al, 1991]. At elevated temperatures hot modulus of rupture, hot crushing strength, creep behavior, refractoriness under load, spalling resistance, dimensional changes and thermal conductivity are determined.

1.2. Statement of the Problem

There has been no local production of firebricks in Kenya despite immense potential of local capacity. The attempt to shift from the import substituted strategy adopted immediately after independence to export oriented manufacturing in the mid 1980's has been of insignificant progress. Kenya's manufacturing sector contribution to GDP has stagnated at about 10 % [African Economic Outlook, 2014]. The performance of manufacturing sector in terms of contribution to Gross Domestic Product, GDP, has remained below the first Medium Term Plan, MTP, and Vision 2030 targets. For example, the sectors contribution to GDP reduced from 10.8 % in 2008 to 9.2 % in the year 2012 [Government of Kenya Ministry of Industrialization, 2013]. The key challenges facing the sector include low value addition, limited diversification, and high costs of production and influx of counterfeits [Kenya Ministry of Devolution and Planning, 2013].

Production of firebricks locally will add value to the clays which mostly do not support sustainable agriculture. Refractory firebricks are a basic necessity for any economy. They account for approximately 80% of total refractories imports in Kenya for its industrial process utilization. The total import costs are estimated at Kshs. 3 billion per annum [Kenya Central Bureau of Statistics, 2013]. In the year 2008-2009, Kenya imported approximately 36 metric tons of firebricks from India alone at an approximate cost of Kshs. 3.6 tons. In the year 2009-2010, the imports of firebricks from India increased to 293 tons. The 8 fold import increment was attributed to Kenya's growing industrial demand, cement industry emerging the major consumer of firebricks accounting for 47 %. The remaining 53 % was consumed in ceramic, sugar, metallurgy, incineration and others [Kenya Central Bureau of Statistics, 2012].

8

Most of local incineration facilities in Kenya are broken down due to warn-out refractory firebrick lining [Step-by-Step Group, 2004; Intermediate Technology Consultants, 2004; Environmental Liaison, Education and Action for Development, 2005]. The renovation and repair of existing incineration facilities in Kenya has been costly due to expensive imported firebricks. A case study at Nairobi Dandora Landfill indicates that all waste including harmful hospital waste is burnt open air. Dandora landfill, the main pollutant of Nairobi River, emits enormous amounts of CH_4 (g), the most lethal green house. The Intergovernmental Panel on Climate Change, IPCC, study determined that methane in earth's atmosphere was a harmful greenhouse gas with a global warming potential of 34 times compared to CO_2 (g) over a 100-year period. As a result, waste incineration has potential to reduce greenhouse gas effect compared to landfill waste disposal method.

There has been no in-depth research on raw materials for production of refractories in Kenya. There is need to locally produce firebricks for the incinerator lining. Catalytic incineration is one of the viable solutions to global warming and waste management. The renovation and repair of existing incineration facilities in Kenya has been in deplorable condition. The problems have been aggravated by the expensive and general purpose firebricks that make incinerator line replacement unreachable and ineffective.

Although availability of raw materials poses challenge on large scale production of firebricks, small scale production of firebricks for incineration facility can be achieved. An in-depth understanding of: chemical composition; particle size distribution, amount of water and grog; firing schedule, micro-structural development; and their influence on the material properties of ceramic firebricks as well as their control by formulation and processing conditions; are important if optimal material properties of firebricks are to be achieved.

1.3. Objectives

The objective of the project was to formulate refractory firebrick using locally available Kwale Ilmenite Ore, Eburru Kaolin, Eburru Fireclay and Mukurweini Ball Clay to be utilized as incinerator lining.

The specific objectives were to:

1. Characterize raw materials.

2. Formulate the firebrick.

3. Characterize the sample firebricks.

4. Correlate the mechanical properties of firebricks with processing conditions.

1.4.Justification and Significance of the Study

This study is devoted to investigation of Kwale Ilmenite Ore, Eburru Kaolin, Eburru Fireclay and Mukurweini Ball Clay as possible source of raw material for production of incinerator firebricks. The firebricks will enhance catalytic breakdown of organic compounds to less harmful CO_2 and H_2O. TiO_2 present in Kwale Ilmenite Ore aids in catalytic breakdown of harmful organic incinerator emission to CO_2 and H_2O.

Kenya is endowed with clays that can be utilized in firebricks production. There are substantial deposits of Mukurweini ball clay, Eburru Kaolins and Eburru Fireclays that can be economically utilized for production of refractory firebricks. The Mukurweini ball clays in Nyeri County deposits are estimated to be occupying more than 1000 000 hectares while Eburru Kaolins and Fireclays in Nakuru County are estimated at an approximate area of 100 000 hectares with approximate yield of 1.5 tons/ m^2. Furthermore, the possibilities of recycling waste firebricks as a source of grog will ensure sustainability of raw materials and mitigate environmental impacts due to quarrying in Kenya. Grog is the main input in the formulation of firebricks. Recycling of waste firebricks will tremendously cut the cost of energy and help in sustaining refractory firebrick industry.

Catalytic waste incineration provides one of the viable avenues to significantly reduce global warming. The proposed policy responses to global warming include mitigation by emissions reduction, adaptation to its effects and building systems resilient to its effects. Kenya is party to the United Nations Framework Convention on Climate Change, UNFCCC, whose ultimate objective is to prevent dangerous anthropogenic climate change. Parties to the UNFCCC have adopted a range of policies designed to reduce greenhouse gas emissions and to assist in adaption to global warming. Parties to the UNFCCC have agreed that deep cuts in emissions are required,

11

and that future global warming should be limited to below 2.0 °C relative to the pre-industrial level. The reports published in 2011 by the United Nations Environment Program and the International Energy Agency suggests that efforts as of the early 21st century to reduce emissions may be inadequate to meet the UNFCCC's 2 °C target. Emissions of greenhouse gasses grew 2.2 % per annum between 2000 and 2010, compared with 1.3 % per annum from 1970 to 2000.

The manufacturing sector has high yet untapped potential to contribute to employment and GDP growth [Government of Kenya Ministry of Industrialization, 2013; African Economic Outlook, 2014]. Production of firebricks in Kenya presents a lucrative opportunity to create employment, add value to natural resources and spur GDP growth. This research will come up with formulation of refractory firebrick from locally available raw materials to be utilized as a lining in incinerator. The research results will be used to local capacity in firebrick production. Characterization of firebrick raw materials will open up more avenues, especially in commercial application, for the utilization of clays to ensure local production sustainability. Sustainable Firebrick Industry in Kenya will enhance value addition on local resources; mushrooming of local SME's and waste management. Value addition and local SME's will create jobs and hasten economic growth. Proper waste disposal will improve on ambient air quality and raise standards of living.

Chapter 2

LITERATURE REVIEW

2.1. Refractories

The broad variety of pyro-processing applications across manufacturing industry demands great diversity in the supply of refractory materials. Many of these materials have been developed specifically to meet the service condition of a particular process. The characteristic properties of each refractory class are a function of both raw materials and methods used to manufacture the refractory products [Harbison, 2005]. Primarily refractories are classified as basic, high-alumina, silica, fireclay and insulating. There are also classes of special refractories which include silicon carbide, graphite, zircon, zirconia, fused castables and several others. Most refractories are supplied as preformed shapes. However, they are also manufactured in the form of special purpose clays, bonding mortars, and monolithics, such as hydraulic setting castables, plastic refractories, ramming mixes, and gunning mixes. A variety of processed refractory grains and powders are also available for certain applications [Boccaccini & Boccaccini, 1997].

2.1.1. Raw Materials

Refractory firebricks raw materials consist essentially of hydrated aluminum silicates with minor proportions of other minerals. The general chemical formula for these aluminum silicates is $Al_2O_3.2SiO_2.2H_2O$. However, even the purest clays contain small amounts of other constituents such as compounds of Fe, Ca, Mg, Ti, Na, K, Li and usually some free SiO_2 [Kingery et al, 1991]. The raw materials of importance as refractories are flint and semi-flint clays, plastic and semi-plastic clays and kaolins. Flint clay also known as hard clay derives its name from its

extreme hardness. It is the principal component of the most super-duty and high-duty firebrick. Most flint clays break with a conchoidal, or shell like fracture. Their plasticities and drying shrinkage, after they have been ground and mixed with water, are very low; their firing shrinkages are moderate. The best clays of these types have low impurities and have a Pyrometric Cone Equivalent, PCE, of cone 33 to 34-35 [Reed, 1987].

Plastic and semi-plastic refractory clays vary considerably in refractoriness, plasticity and bonding strength. Drying and firing shrinkages are usually fairly high. The PCE of clays of these types ranges from Cone 29 to Cone 33, for the most refractory varieties and from Cone 26 to Cone 29 for many types of clay of high plasticity and excellent bonding power [Kshama et al, 1992]. Most commercial deposits of flint and plastic refractory clay occur in sedimentary strata in association with coal beds [Harbison, 2005]. Kaolins consist essentially of the mineral kaolinite. They usually are moderately plastic and have extremely high drying and firing shrinkages. Siliceous kaolins shrink less and bauxitic kaolins shrink more than kaolins which consist almost wholly of kaolinite. Refractory kaolins generally have a PCE of Cone 33 to 35; less pure varieties with a PCE of Cone 29 to 32 are common [Levin et al, 1979].

Clays exist in different types, with each type showing characteristic chemical and physical properties. Due to this wide variety of properties, clays can be selected to create a set of properties designed to fit closely with desired requirements [Papargyris & Cooke, 1996, Peacor et al, 1999]. Clays provide via their plasticity, the necessary green strength after the ceramic material has been dried and have the property of fusing when fired [Kim & Carty, 1998]. Clays also contribute substantially to the color of the ceramic product. The plasticity developed by clays when water is added to them is unique, and no other material gives such high plasticity. It

is this property plus the fact that clays are cheap source of the chemicals required to take part in high temperature reactions which has made clays the basis of ceramic industry.

Plasticity arises due to particle-particle interactions and is influenced mostly by particle size, distribution, and particle morphology. The small size, plate-like nature of crystals and the high specific surface area of clay particles are responsible for the high plasticity and many of the important properties of clay minerals compared to other raw materials like silica which has poor plasticity. Kaolin is white in color although it is colored pink-orange-red due to presence of iron oxide, giving it a distinct rust hue. Lighter concentrations yield white, yellow or light orange colors. The clay mineral kaolinite has a 1:1 sheet silicate structure composed of $[Si_2O_5]^{2-}$ and gibbsite $[Al_2 (OH)_4]^{2+}$ layers [Kingery, 1967; Carty & Senapati, 1998]. Silica on the other hand has a tetrahedron structure. Kaolins commonly consist of 20 -80 % kaolinite, 10-25% mica, 6 - 65% quartz and traces of other minerals; silimanite, andalusite and kyanite, of the general chemical formula $Al_2O_3.SiO_2$.

2.2. Firebricks Formulation

2.2.1. Mineralogical Composition of Ceramic

The physical properties of a ceramic material at any given temperature are fixed by the mineralogical composition [Nyongesa, 1994]. One of the most important purposes for which firebricks are fired is to give them permanent mechanical strength, by causing adjacent particles to sinter. The strength of the ceramic bond is dependent upon the chemical composition as well as upon the time and temperature of firing. The accessory constituents of a refractory which occur in only small amounts play an important role in the development of the ceramic bond [Schneider et al, 2008].

Refractory firebricks mainly consist of Al_2O_3 and SiO_2 with minor proportions of oxides of alkali and alkali earth metals. During the firing of firebricks, mineral dissociation or transformation occurs; such minerals as kaolinite or diaspore dissociate, and quartz is transformed wholly or in part into other forms [Levin et al, 1979]. Crystal growth and chemical reactions occur also in the solid state, resulting in the formation of a strong ceramic bond between particles. However, solid-state reactions are believed to have less influence upon the bonding of silica-alumina brick than does the formation of a liquid phase. In the firing of firebricks, a small amount of liquid can be expected to form in groundmass at a temperature hundreds of degrees below which complete fusion would occur. As temperature increases, the liquid takes other materials present into solution thereby increasing in amount [Shi, 1999].

The most stable and important phase formed during firing of Al_2O_3-SiO_2 firebricks is mullite, $3Al_2O_3.2SiO_2$, that has a melting point of about 1850 ^{O}C. Mullite is formed from the minerals

kaolinite, $Al_2O_3.2SIO_2.2H_2O$, and silimanite, $Al_2O_3.SiO_2$ as shown in figure 1 below [Harbison 2005].
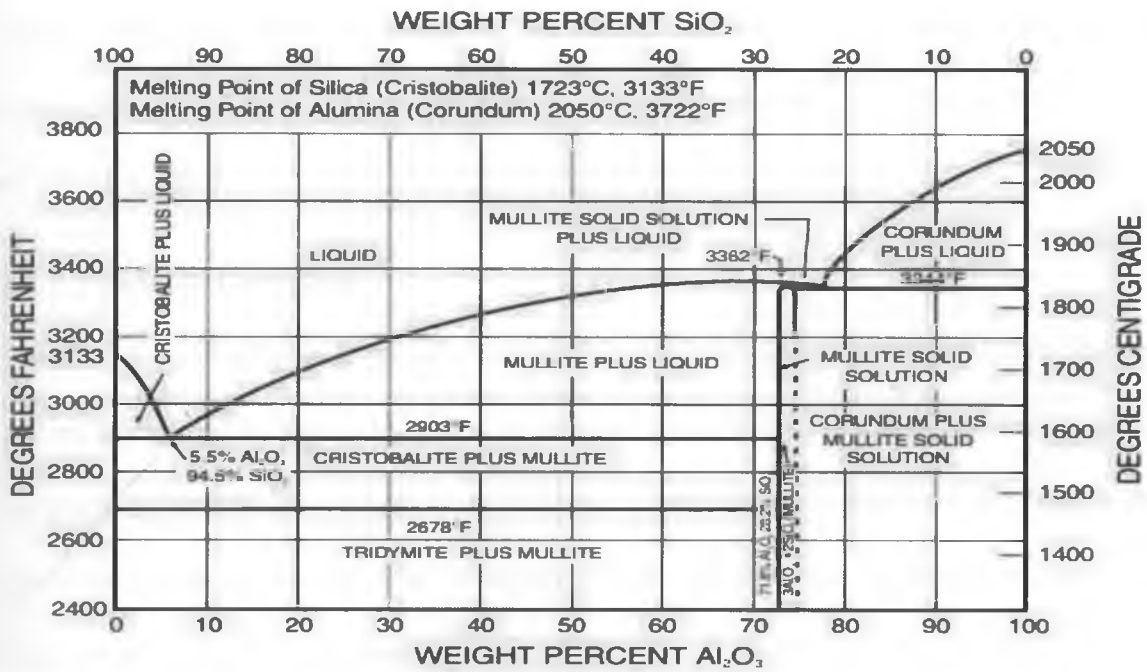
Figure 1: Alumina-Silica Phase System

On heating $Al_2O_3. 2SiO_2.2H_2O$, it loses most of its water at about 400 to 525 ^{O}C depending on the particle size with the formation of a semi-crystalline compound meta-kaolin, $2Al_2O_3.4SiO_2$ in an endothermic reaction [Bergeron & Risbud, 1984] as shown in equation 2.1 below.

$2Al_2O_3.2SiO_2.2H_2O \xrightarrow{400\ ^O C\ to\ 525\ ^O C} 2Al_2O_3.4SiO_2(s) + 4H_2O\ (g)$.............................2.1

When meta-kaolin is heated to about 925 ^{O}C, an exothermic reaction takes place in which some of the silica migrates out of meta-kaolin. in a cubic spinel type phase of $2Al_2O_3.3SiO_2$. The silica set free, as shown in equation 2.2, is poorly crystallized that it cannot be identified as crystalline material by X-ray diffraction spectrophotometer.

$2Al_2O_3.4SiO_2(s) \xrightarrow{(925\ ^\circ C)} 2Al_2O_3.3SiO_2(s) + SiO_2\ (l)$.................................2.2

At a temperature range of 1050 to 1100 ^{O}C the spinel-type phase begins to breakdown and releases more SiO_2. A phase resembling mullite and of uncertain composition forms, that contains more silica than the composition $3Al_2O_3.2SiO_2$. The released silica appears to be cristobalite that gives well-defined X-ray diffraction pattern. Above 1200 ^{O}C, cristobalite and mullite continue to develop and the mullite formed at 1400 ^{O}C or above is believed to have the composition of $3Al_2O_3.2SiO_2$ with no excess SiO_2 [Chakraborty and Ghosh, 1977; Schneider et al, 2008].

2.2.2. Firebrick Corrosion

The alkali and alkaline earth metals concentrations contribute to the degradation of the firebricks. According to micro-chemical studies, cations of alkali and alkaline earth metals are able to enter the mullite structure from the service condition, though in small quantities. Because of the size of the alkali cation, it may be only incorporated into the thermally expanded mullite structure at high temperature [Karl & Mark D. A., 2002; Ngai et al, 2002]. The alkalis first diffuse into glassy phases, until they reach the saturation, then crystalline compounds such as cristobalite, mullite and quartz will dissolve forming new phases such as nepheline, $Na_2O.Al_2O_3.2SiO_2$, and leucite, $K_2O.Al_2O_3.4SiO_2$. Between 760 and 930 ^{O}C cristobalite liquefies completely, above 930 ^{O}C other crystalline compounds dissolve, and leucite, kaliophilite and high alumina compounds are formed. Between 1000 and 1050 ^{O}C starts the formation of α-corundum and alkali aluminates [Ngai et al, 2002; Geith et al, 2001, Viswabaskavan et al, 2002]. The concentration of alkalis and alumina content influence the effect of the slag attack in the firebrick. Zimmermann & Julien, [2007] observed that reactions change according to the alumina and soda concentrations. For alkali content lower than 10%, due to alkalis and hematite action, mullite liquefies at 1175 ^{O}C. Formation of iron-alumina oxide, $Fe_2O_3Al_2O_3$, and nepheline phase is present, taking the

corundum from the grains in the firebrick; this nepheline phase melts at 1253 ^{O}C. For high alkali content, mullite is liquefied completely in a melt at 1235 ^{O}C, needles crystallization is induced by alumina present in the melt. The alkalis react with the acidic SiO_2, while single grains of the Al_2O_3 were seen to be more resistant to alkali. However it does not mean that a high Al_2O_3 firebrick is a better material than a brick with less Al_2O_3 content. Stjernberg and others in 2010 observed in tests between 700 and 1150 ^{O}C that the basic oxide Na_2O reacts with mullite and SiO_2 to form the alkali feldspathoid, nepheline. They also showed that the amount of nepheline phase decreases at higher temperature. At 1230 ^{O}C nepheline partially disintegrates to an amorphous phase. It is assumed that the formation of feldspathoid such as nepheline, kalsilite, $K_2O.Al_2O_3.2SiO_2$ and leucite contributes to the degradation of the firebricks. Those phases are formed when alkali metal reacts with alumino-silicates. Previous work of Narita and coworkers in 1981 showed that the wear of firebrick was mainly due to the formation of kalsilite in accordance with the reaction equation 2.3 below and its expansion, calculated volume change of 6%.

$$6K + 3Al_2O_3.2SiO_2 + 4SiO_2 + 3CO \longrightarrow 3(K_2O.Al_2O_3.2SiO_2) + 3C\ldots\ldots\ldots 2.3$$

Table 2: Phase Transformation Volume Increments

Mineral Phase	Volume Increase (%)
Nepheline, $Na_2O.Al_2O_3.2SiO_2$	6
Kaliophilite, $K_2O.Al_2O_3.2SiO_2$	6
Leucite, $K_2O.Al_2O_3.4SiO_2$	10

[Source: Geith et al, 2001]

Hayashi and Shibuno in 1979 observed that alkali vapor forms liquid phase by the reaction with glass and cristobalite in the brick besides the formation of alkali alumino-silicates causing the deterioration of brick and may accelerate the wear. The behavior of lithium has been studied also; although it has no significant effects as sodium or potassium. The lithium alumino-silicate eucryptite, $Li_2O.Al_2O_3.2SiO_2$, has been tested due to its interesting thermal expansion behavior at high temperatures [Winker, 1953]. There are two polymorphic modifications of eucryptite; at low temperature α-eucryptite is formed in nature; at high temperatures, 972 ^{O}C ± 10 ^{O}C, α-eucryptite transforms into β-eucryptite, with the same structure as high temperature quartz [Hummel, 1951].

The oxygen partial pressure in a refractory firebrick lined enclosure may vary in service leading to a change of valence of some components, in particular iron oxide, in the refractories and or slag. This can significantly affect the refractories corrosion resistance. Consider the influence of atmosphere on corrosion resistance of Al_2O_3-SiO_2 refractories containing, or in contact with, iron oxide [Zhang & Lee, 2000]. In strongly reducing conditions a liquid will develop at 1210 ^{O}C when a firebrick consisting initially of tridymite or cristobalite and mullite absorbs a small amount of iron oxide. If, however, the brick is higher in alumina and originally consists of mullite and corundum, a liquid will not form until 1380 ^{O}C is reached, even after a considerable amount of iron oxide has been absorbed by the brick. In air, the lowest temperatures of liquid formation for bricks of the same compositions as above are considerably higher. On addition of iron oxide, firebrick develops a liquid phase only after a temperature of 1380 ^{O}C or higher is reached, while a higher alumina brick with absorbed iron oxide withstands temperatures at least as high as 1460 ^{O}C before liquefying [Levin et al, 1964; Jacques & Bouchetou, 2006].

Two of the crystalline phases present in Al_2O_3-SiO_2 refractories, mullite and corundum, can accommodate iron ions in their lattices, but only in the ferric state, Fe^{+3}. Under reducing conditions, where the iron in the oxide phases is present almost exclusively as Fe^{+2}, and incorporation of the Fe in the crystalline phases cannot take place. Hence, even small amounts of iron oxide absorbed cause a liquid to develop at temperatures above 1210 ^{O}C and 1380 ^{O}C, depending on the Al_2O_3/SiO_2 ratio of the original brick. In air, on the other hand, a substantial proportion of iron is present as Fe^{+3}. Hence moderate amounts of iron oxides can be absorbed by Al_2O_3-SiO_2 refractories without formation of a liquid phase [Zhang & Lee, 2000].

Al_2O_3-SiO_2 made refractories have better corrosion resistance in oxidizing than in reducing atmosphere. It therefore can be deduced that carbon in Al_2O_3-SiO_2-Cs refractories may have different effects on the corrosion resistance of Al_2O_3 -SiO_2 grain phases, depending on the local reducing conditions. If carbon only reduces Fe_2O_3 in the refractories or slag to FeO, then Al_2O_3-SiO_2 grains resistance to slag attack will be decreased. However, if carbon further reduces FeO to metallic Fe, the liquid formation temperature and the slag viscosity will increase thereby improving the resistance of the Al_2O_3-SiO_2 grains to slag attack.

Pure alumina reacts with the iron oxides to form hercynite, an Al_2O_3-Fe_2O_3 spinel, with a high melting point, 1780 ^{O}C. Formation of hercynite has the disadvantage of causing a drastic change in volume that can cause spalling of firebrick [Jacques & Bouchetou, 2006; Zhang & Lee, 2000]. Alumina and high alumina refractories are sensitive to corrosion by iron oxides because of formation of low melting compounds; iron oxide is more corrosive as the content of alumina in the refractory is lower; and alumina refractories have different degrees of resistance to corrosion by iron oxides depending on the oxygen potential.

2.2.3. Parameters Affecting the Creep Behavior of Al_2O_3-SiO_2 Firebricks

Although a lot of information is available on the effect of additives, corrosion process and thermo-chemical behavior of refractories, little data exists on the creep response of these materials. Dimensional stability at high temperatures is a major concern in case of firebricks, especially when they are subjected to a load or stress as well. Under the mentioned conditions, these materials undergo significant creep: a process known as a time-dependent irreversible strain [Stjernberg et al, 2010]. In addition to the application temperature and stress, the modifications in microstructure can also affect the creep resistance of refractories. Most commercial refractories are made from porous and permeable aggregates having some impurities in their grain boundaries. These impurities, such as siliceous and alkaline materials, separate the crystals of major phases [Kim & Carty, 1998].

In the study on the effects of microstructure on creep [Kamran & Allaire, 2000]found out that the cracks were nucleated and propagated in andalusite, while their propagation were stopped on reaching the mullite phase, thus andalusite is more susceptible to cracks than mullite, leading to lower creep resistance of andalusite, $Al_2O_3.SiO_2$, compared to mullite, $3Al_2O_3.2SiO_2$. The researchers, also found out that tiellite constituting ≈42 wt. % TiO_2 + ≈51 wt. % Al_2O_3 + ≈7 wt. % FeO, is most likely responsible for lowering the creep resistance. In order to have a better understanding of the mentioned findings, and also the effects of refractories structure on their creep behavior, it is essential to take into account all micro-structural parameters affecting the creep process of ceramic materials.

The diffusion rate of materials structure can be respectively promoted or limited depending on whether their lattice is open or closed [Sherby & Lytton, 1956; Sherby & Burke, 1968]. Although mullite and andalusite have different compositions, their crystalline structures are

orthorhombic. The only difference arises from their crystallographic constants as shown in Table 3 below. Considering that mullite and andalusite are formed of Al_2O_3 octahedral parallel to c, each Al_2O_3 has an O-O edge of approximately 2.9 Å and 5.6 Å length, c value respectively for mullite and andalusite as shown in table 3 below.

Table 3: Crystallographic Data of Mullite and Andalusite

	Crystallographic Data (Å)		
	a	b	c
Mullite	7.5785	7.6817	2.8864
Andalusite	7.7942	7.8985	5.5590

[Source: Peacor et al, 1999]

It is obvious, the c value for andalusite, 5.5590, is twice as much as that of mullite, 2.8864. In other words, mullite is twice more closely packed compared to andalusite resulting in much lower diffusion rate of creep. This implies that the diffusion rate or creep rate in the open lattice of andalusite is at least twice that of mullite [Peacor et al, 1999]. It should be mentioned that the density of mullite and andalusite are 3.15-3.26g/cm^3 and 3.13- 3.16 g/cm^3 respectively [Kamran & Allaire, 2000]. As the creep phenomenon and its characteristics are always discussed with respect to diffusion process, another major conclusion from the previous explanation is that there is a specific element having much higher diffusion rate in andalusite than mullite. This specific element, responsible for occurring and /or controlling creep is not known yet; though it is believed that it is most likely silicon [Peacor et al, 1999]. Generally, any element responsible for the occurrence of creep can be easily determined by calculating the activation energy of creep [Hertzberg, 1967]. Consequently, preventing or limiting the diffusion of this element can control the creep process.

Phases having higher melting points exhibit higher creep resistance at a given temperature. For example, compared to metals, firebricks have higher creep resistance due to their high melting point. For this reason, creep becomes the dominant deformation mechanism at temperatures above $0.3T_m$, where T_m is the melting temperature for metals and above $0.5T_m$ for ceramics [Gandi et al, 1979]. In the case of a multi-phase material such as refractories, the controlling factor in creep process is therefore a phase with lower melting point, which then forms a continuous phase or a non-crystalline glassy phase during creep. As mentioned, compared to solids, the diffusion rate is much higher in a liquid phase leading to deformation of these phases more easily. The low melting phase can be a phase already existing in the raw material as impurities, e.g. alkaline compounds, hematite or iron oxide [Jokanovic & Spasic, 1992]. Regarding the effect of melting temperature on mullite and andalusite on creep behavior, mullite has a high melting point compared to andalusite, 1920 ^{O}C and 1868 ^{O}C, respectively [Carniglia & Barna, 1992]. The differences in melting point of these two phases explain the higher creep resistance as well. The temperature promotes the diffusion and creep process according to Equation 2.4.

$$D = D_0 \exp(-\frac{\Delta H_c}{RT})$$
                                                                                        2.4

Where D is diffusivity, D_0 is the diffusivity constant, ΔH_c is the activation energy for creep, R is the gas constant and T is the absolute temperature [Schneider et al, 1994].

The chemical stability of a phase affects its creep behavior. The higher the stability of a phase, the higher its creep resistance. Mullite has a very high significant stability at high temperature compared to andalusite. This is attributed to the dense lattice of mullite and its high melting point. Compared to andalusite, higher stability of mullite is reasonable, since it is formed when

andalusite starts transforming to mullite at high temperatures. The higher stability of mullite is also because of the interlocked mullite needles [Kamran & Allaire 2000; Schneider et al, 1994]. Increasing the number of grain boundaries i.e. smaller grains, the creep rate is also increased [Carniglia & Barna, 1992]. With respect to grain boundary morphology, an elongated grain can hold up the crack. In this way, the life or creep resistance of refractories is increased by long waiting time required for crack to go through such grains. In general the creep rate is related to the grain diameter as shown in equation 2.5 below.

$$\dot{Y} = 1/d^3 \hspace{8cm} 2.5$$

Where d is the grain diameter. Equation 2.5 is only applicable to the crystalline parts or crystalline phases of firebricks. Compared to ceramics, presence of pre-existed pores in refractories, the effect of porosity on creep process is much more pronounced. There are three steps of fracture development in materials: micro-crack nucleation; crack growth; and crack coalescence leading to rupture. The first step involves the longest time in terms of the life of materials undergoing creep phenomenon since the crack nucleation is very sluggish. The other two steps, cracks growth and their coalescence, take place much faster. Porosity reduces the life of refractories by accelerating the first step of the creep [Jokanovic & Spasic, 1992].

Another micro-structure defect that affects the creep resistance of refractories is Stacking Fault Energy, SFE. This is a phenomenon that occurs only in crystalline parts of the refractories, e.g. individual crystalline grains or phases such as andalusite, mullite, silica etc. In general, materials possessing higher SFE show higher creep rate [Hertzberg, 1967]. The creep resistance of ceramic materials could be enhanced significantly by the addition of a second phase [Kamran & Allaire, 2000]. Chan and Page in 1993 reported that in the presence of relatively small amount of second

phases, the crack grows more slowly before the occurrence of creep rapture. The creep behavior of multiphase materials like refractories is generally complicated because each phase has a proportional contribution to the total deformation. The hardness or softness of the second phase can strongly influence the creep rate of refractories. As an example, among fused silica, 40 % Al_2O_3 alumino-silicate, 60 % Al_2O_3 alumino-silicate, tabular alumina and zircon refractories, the latter exhibited the highest temperature stability. This resulted in the highest hot modulus of rupture and greatest creep resistance which was attributed to the properties brought about by using a hard phase such as ZrO_2.

2.3.Sintering

The densification of a ceramic material when heat is applied is referred to as sintering. It is essentially removal of the pores between the starting particles, accompanied by shrinkage of the component, combined with fusion and strong bonding between particles [Arato et al, 1995]. For sintering to occur there must be a mechanism for material transport and a source of energy to activate and sustain the material transport means. Conventional sintering occurs by a variety of mechanisms e.g. vapor phase, solid state, liquid state and reactive liquid state.

Table 4: Sintering Mechanisms

Type of sintering	Material transport mechanism	Energy
Vapor phase	Evaporation-condensation	Difference in vapor phase
Solid state	Diffusion	Difference in free energy or chemical potential
Liquid phase	Viscous flow, diffusion	Capillary pressure, surface tension
Reactive liquid	Viscous flow, solution precipitation	Capillary pressure, surface tension

[Source: Richerson, 1982]

The primary mechanisms for material transport are diffusion and viscous flow as summarized in Table 4 above. Each sintering mechanism can work alone or in combination with other mechanisms to achieve densification. Heat is the primary source of energy, in conjunction with energy gradients due to particle-particle contact and surface tension. Modified densification processes that can also achieve strong bonding in ceramics include hot pressing, reaction sintering, chemical vapor deposition etc.

2.3.1. Vapor-Phase Sintering

In vapor-phase sintering, as shown in Figure 2 below [Arato *et al*, 1995], the driving energy is the difference in vapor pressure as a function of surface curvature.
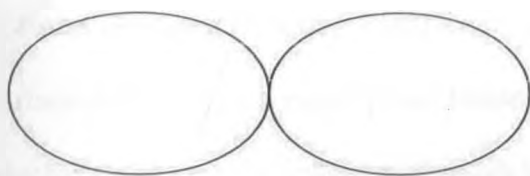
Adjacent particles in contact
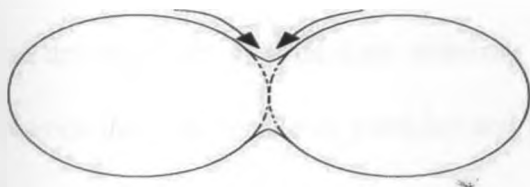
Neck formation by vapour phase material transport
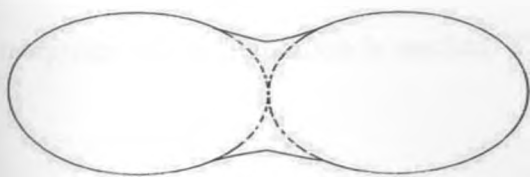
Completion of vapour phase material transport: Particles bonded, pore shape changed but no shrinkage

Figure 2: Vapor Phase Material Transport

The material is transported from the surface of the particles that have a positive radius of curvature and a relatively high vapor pressure, to the contact region between particles that has a negative radius of curvature and a much lower vapor pressure as illustrated in Figure 2 above. In general, the smaller the particles, the greater the positive radius of curvature and the greater the driving force for vapor phase transport. Vapor phase transport changes the shape of the pores and achieves bonding between adjacent particles and thus it increases the material strength and decreases the permeability due to open porosity. However, on its own, it does not result in shrinkage and cannot produce densification. It must be accompanied by other mechanisms that provide bulk material transport or transport of pores to external surfaces to achieve densification.

2.3.2. Solid-State Sintering

Solid-state sintering involves material transport by diffusion. Diffusion can consist of movement of atoms or vacancies along a surface or grain boundary or through the volume of the material. Surface diffusion, like vapor-phase transport, does not result in shrinkage but volume diffusion, whether along grain boundary or through lattice dislocations, results in shrinkage as illustrated in Figure 3 below [Ting & Lin, 1994].

The driving force in solid-state sintering is the difference in free energy or chemical potential between the free surface or particles and the points of contact between adjacent particles. Solid state sintering can be divided into three stages: initial, intermediate and final [Arato et al, 1995]. In the initial stage, the interface formation and neck growth between primary particles occurs till an equilibrium configuration is reached. This stage involves no grain growth.

The second or intermediate stage of sintering starts when grain growth begins. During this stage of sintering, the grain boundary forms extensively resulting in a network of interconnected grains and pores.

L_1	Adjacent particles in contact
L_2	Neck formation by diffusion
L_3	Distance between particles centres decreased ($L_3 < L_2 < L_1$), particles bonded, pore size decreased
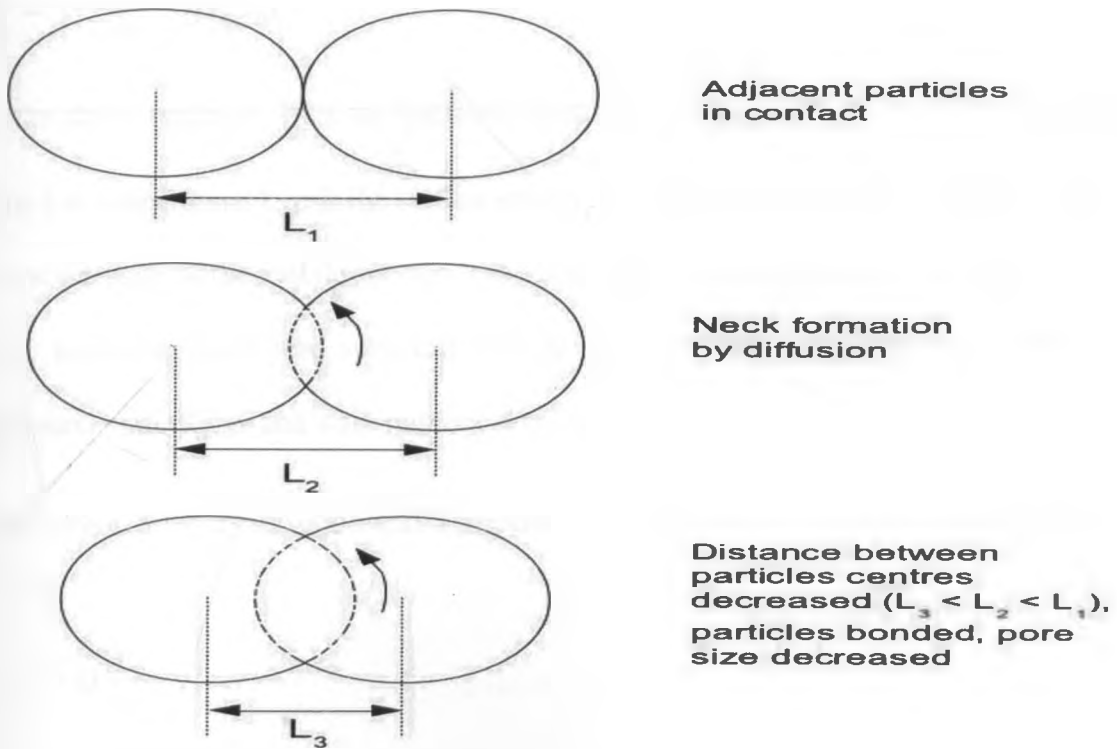
Figure 3: Solid Phase Material Transport

As pores become isolated, the intermediate stage of sintering ends and the third or the final stage of sintering begins. Density increases slightly but the microstructure develops very rapidly in this stage of sintering. A number of researchers such as Singh in 1996, Ting & Lin in 1994a, Ting & Lin in 1994b modeled the different stages and predicting the morphology of the structure and the kinetics of the densification.

2.3.3. Solid-State Sintering Models and Theories

There are three stages in the commonly used solid-state sintering model and theory i.e. Initial stage, intermediate and final stage. In the initial stage of sintering, the proposed expression describing the densification processes has the form of Equation 2.6 below [Ting & Lin, 1994a].

$$\frac{\Delta L}{L0} = \{\frac{K_1 \mu \Omega D^p}{kT}\}D_{size}^{-d}t^q \qquad\qquad 2.6$$

In the above equation, $\frac{\Delta L}{L0}$ is the fractional linear shrinkage, equivalent to the sintering rate, after time t at temperature T, μ is the surface energy, Ω is the atomic volume of the diffusing vacancy, D the diffusity of the mobile species, k the Boltzmann constant, D_{size} the average particle or grain size, assuming equal size spherical starting particles, and d is a constant depending on the diffusion path. K_1, p, and q are numerical constants.

D is affected by composition and Temperature according to Fick's first law given by Equation 2.7.

$$J = -D\frac{\partial c}{\partial x} \qquad\qquad 2.7$$

Where $\frac{\partial c}{\partial x}$ is the concentration gradient and J, the flux, quantity per unit time per unit area.

Equation 2.6 above holds for a variety of shapes of particles and it is apparent from both Equations 2.6 and 2.7 that the rate of shrinkage increases with increasing temperature and with decreasing particle radius. Not apparent, in Equation 2.6, but highly important to the final properties, are the uniformity of particle packing, the particle shape, and the particle size distribution. If particle packing is not uniform in the green ware, it will be difficult to reduce the porosity to the required standards during sintering. A high concentration of elongated or flattened particles may result in bridging during forming, producing large or irregularly shaped pores that

are difficult to remove during sintering. On the other hand, particles that are all of one size do not pack efficiently; they form compacts with large pores and high volume fraction porosity. Compared to other stages of sintering, the total shrinkage in the initial stage of sintering is limited [Shi, 1999]. In the Intermediate and Final Stages of Sintering, the grain size, D_{size}, is a function of time and sintering equation can be expressed as [Ting & Lin, 1994a].

$$R(t) = K_2 \frac{D_{size}(t)}{D_{size(0)}^{dj}} \qquad 2.8$$

Where R (t) denotes a general relative shrinkage at time t, $D_{size\,(0)}$ is the original particle size, K_2 a constant, and dj is a constant dependent on the diffusion path. Equation 2.8 does not however, take into account the effect of particle size distribution on sintering. Theoretical sintering models that take into account both the effect of particle size distribution and grain growth have been developed by, [Ting & Lin, 1994a]. In this model, the shrinkage of a powder compact in both the initial and intermediate stages of sintering prior to the occurrence of grain growth is given by Equation 2.9 below.

$$R = \int 1 \, K_3(t^q/D_{size}^{d0}) \, f(D_{size})dD_{size} / \int f(D_{size})dD_{size} = K_3 t^q F_0 (D_{size}) \qquad 2.9$$

In the above equation, $F_0 (D_{size})$ denotes the shrinkage rate factor before the occurrence of grain growth and depends on the characteristics of the starting particle size distribution while K_3, d_0 and q are constants. When grain growth occurs, the rate of densification may be obtained by taking the time derivative of Equation 2.9 [Ting & Lin, 1994a]. The densification equations in the final stages of sintering [Shi, 1999] are similar to those in the intermediate stages.

2.3.4. Liquid-Phase Sintering

Liquid phase sintering involves the presence of a viscous liquid at the sintering temperature and is the primary densification mechanism for most alumina-silica systems. Liquid-phase sintering occurs most readily when the liquid thoroughly wets the sold particles at the sintering temperature [Kingery, 1967]. The liquid in the narrow channels between the particles results in substantial capillary pressure, which aids densification by rearranging the particles to achieve better packing and increasing the contact pressure between them. This increases the rate of material transfer by solution/precipitation, creep and plastic deformation, vapor transport, and grain growth. The rate of liquid-phase sintering is also strongly affected by temperature. For most compositions, a small increase in temperature results in substantial increase in the amount of liquid present. In some cases, this can be beneficial by increasing the rate of densification while in other cases; it can be detrimental by causing excessive grain growth, which reduces strength, or by allowing the part to slump and deform. The amount of liquid present at a selected temperature can be predicted with the use of phase diagrams. For a ceramic composed of, or fabricated from three major chemical components, information regarding melting temperatures, composition, percentage liquid or solid, solid solution and polymorphism present at a given temperature and composition can be predicted [Bergron & Risbud, 1984] from phase diagrams of ternary systems.

2.3.5. Modified Densification Processes

There are two modified densification processes i.e. hot pressing and reaction sintering. In hot pressing i.e. pressure sintering, pressure and temperature are applied to the ceramic compact at the same time. The application of pressure at the sintering temperature accelerates the kinetics of densification by increasing the contact stress between particles and by rearranging particle

positions to improve packing. Advantages of hot pressing include reduced densification time, residual porosity and densification temperature often resulting in less grain growth than would occur with pressure-less sintering [Richerson, 1982]. In reaction sintering, strong bonding of a ceramic is achieved without undergoing the large shrinkage of conventional sintering. For example, reaction-bonded Si_3N_4 is fabricated by processing silicon powder into the required shape and placing it in a furnace under nitrogen or mixed nitrogen/hydrogen or nitrogen/helium atmosphere and then heated. The nitrogen permeates the porous silicon compact and reacts with the silicon to form Si_3N_4. It is important to point out that a variety of conditions can result in improper sintering and hence a deleterious effect on the material properties. Common problems that occur during sintering include warpage, overfiring, decomposition reactions and polymorphic transformations. Warpage usually results from inadequate support during sintering or from density variations and it increases the rejection rate and thus cost per unit. Overfiring can cause warpage, bloating and excessive grain growth. Excessive grain growth may result in decreased strength. Polymorphic transformations do not usually cause problems during sintering, but can cause problems during cool-down if a sudden volume change is involved. These transformations are particularly important in alumina-silica systems.

2.4. Mechanical and Physical Analysis

2.4.1. Material Properties of Firebricks

The physical properties such as shrinkage, apparent porosity, bulk density etc. and mechanical properties such as impact strength, flexural strength, elastic modulus etc. of firebricks are dependent on their microstructure [Wagh et al, 1993]. Micro-structural features, especially pore phases, size of pores, pore shape, orientation and distribution, glassy phase, grain size and grain size distribution, determine the behavior of ceramic materials [Pickup, 1997, Ohya & Tokahashi, 1999; Zuokai, 1990, Boccaccini & Boccaccini, 1997; Phani, 1996].

The micro-structure of clay-based ceramics such as firebricks is determined by the chemical and mineralogical composition of the raw materials [Papargyris & Cooke 1996]. In addition, the body formulation, type of admixture, particle size and particle size distribution and processing conditions such as the firing schedule also influence the microstructure immensely [Kobayashi et al, 1994; Naga et al, 1993; Gaillard et al; 1993; Saggio Woyansky & Curtis, 1992; Zeng & Reed, 1992; Kshama et al; 1992; Kingery, 1967; Ibisi, 1991].

The particle size and particle size distribution of raw materials have a significant impact on the packing density, size and shape of pore interstices as well as the deformation and the drying behavior of ceramic bodies [Ai-Bing et al, 1993; Kshama et al, 1992; Abdel-Aziz & Kabesh, 1991]. A high concentration of irregular particles can result in bridging during forming producing large or irregular shaped pores which are difficult to eliminate during drying and sintering [Zheng & Reed, 1992; Kingery et al, 1991]. Kshama and coworkers in 1992 observed from sintering studies of plastic clays in which they noted that a material with a wider particle size distribution was compacted better compared to one of very fine or coarse particles.

The ceramic materials are dried below temperatures not exceeding 150 °C using sun and ovens. The shrinkage, which is removal of water films between particles that occurs during the drying process, is dependent on particle sizes of the raw materials. Since the number of water films increase as the particle size increases, materials prepared with a liquid binder and all-fine particle materials have a high shrinkage during drying and the problems of the stresses, warping, distortion and possibly cracking occur [Blanchart & Gaillard, 1995]. Warpage may also develop during drying as a result of uneven shrinkage caused by local variations in the liquid content that may be due to non-uniformity in particle size distribution. Moreover, if shrinkage proceeds at uneven rate, both during drying or firing at higher temperatures normally 1000 °C and above, or if part of the ware is restrained from shrinkage by friction within the material on which it is set, stresses, warpage, and cracking can also develop. A ceramic material may also be warped by flow under forces of gravity. This is especially true for large heavy pieces in which substantial stresses are developed.

Further, for clay ceramics that are formed by the slip casting technique, the settling tendency of the clay particles is directly proportional to the density and the size of the particles [Kingery et al, 1991]. During the settling process, particles may gather together into aggregates, causing sedimentation and a flocculated system that may cause non-uniformity in the physical properties of the green body. Formation of particles depends on the electrical forces between particles. While short-range forces of attraction causes aggregation if two particles approach closely enough, electrostatic forces associated with charges on the solid surface causes repulsion. Addition of alkali cations such as K^+ and Na^+ favors deflocculation of fine clay particles. This is because; alkali cations have a high affinity for water molecules and thus produce a high repulsion potential between adjacent particles [Worrall, 1986].

Controlled sintering is important if material properties of clay-based ceramics are to be optimized. The optimum firing conditions refers to extent to which a clay body must be fired in order to have an acceptable range of properties. In firebricks, properties such as bulk density and strength improve with degree of heat treatment up to a point beyond which, further treatment impairs the properties due to increase in closed porosity [Kobayashi et al, 1992]. Thus among the important parameters that must be controlled during sintering include the firing schedule and the isothermal holding or soaking time [Nyongesa, 1994; Naga et al, 1993; Ibisi, 1991] and the atmosphere within the oven [Gaillard et al, 1993; Bogahawatta & Poole, 1991a].

The above parameters govern the final quality of the fired product by their influence on porosity, thermal expansion coefficient, thermal conductivity, strength and hardness via the relative abundance and texture of the various phases such as the needle shaped secondary $3Al_2O_3.2SiO_2$ and/or the glassy phase. Mullite exists in two varieties. One variety, the primary scaly mullite is produced from decomposition of clays mainly by the reaction of kaolinite and illite, KAl_2 (Si_3Al_{10}) $(OH)_2$, while the other variety, the secondary acicular mullite crystallizes from the glassy liquid phase during cooling [Chandrasekhar & Sampathkumar, 1996]. The mechanical strength of firebrick has sometimes been attributed to the presence of mullite, mullite hypothesis, and or the glassy phase, pre-stress hypothesis. While primary mullite which is situated in the loose clay-mullite aggregates without an intrusion of enough glassy melt considerably lowers the fireclay strength, secondary mullite needles contributes to the strength increase due to networks interlocking in the weak glassy phase [Mattyasovszky-Zsolnay, 1997].

Sane and Ralph in 1995 noted that when the fired strength of ceramic materials were correlated with the X-ray data, the strength was dependent on the total mullite and glass phases present. Papargyris and Cooke in 1996 shared the same concept that the mullite formation may be

beneficial for improving the fracture strength of the clay ceramics by altering the fracture path i.e. since mullite is stronger than glass, fracture will prefer the easiest path by avoiding the mullite needles instead of crossing them. Thus, mullite needles act as reinforcing agents in the same way as ceramic fibers reinforce ceramic composites. However, both the mullite and pre-stress hypothesis in the strengthening of the clay ceramics is still a subject of controversy. For example, Papargyris and Cooke in 1996, on contrary expressed views that mullite does not play a major reinforcing role in kaolinite based ceramics as evidenced by their micrographs from which they did not observe evidence of reinforcing mechanism such as mullite needles standing out of the structure surfaces. The pre-stress hypothesis attributes strength of clay-based ceramics to the compressive pre-stresses imposed in glassy phase during cooling due to the higher degree of contraction of quartz compared to the glass phase as well as due to the abrupt expansion changes accompanying phase transitions [Zuokai, 1990]. These stresses may cause extensive cracking that in turn lowers the strength of the body [Ohya & Takahashi, 1999].

During the firing process of clay ceramic materials, sufficient atomic mobility in the solid is also developed to permit chemical reactions, and sintering. Theoretical models relating to the rate of sintering shows that the sintering rate is roughly inversely proportional to the particle size but proportional to the sintering time [Kingery et al, 1991; Singh, 1996]. Excessive firing for example, may cause excessive grain growth that may result in decreased strength and increased porosity since the distribution of pore sizes shifts to larger sizes with smaller pores disappearing and larger ones growing at high temperatures [Zheng & Reed, 1992]. In general, the strength of the ceramic increases with a decrease in either porosity or grain size and for non-porous brittle polycrystalline specimens, the dependence of strength, σ, on the average grain size, D_{size}, could be represented satisfactorily by the expression of the form [Knudsen, 1959].

$$\sigma = kD_{size}^{-\alpha} \qquad\qquad\qquad\qquad 2.10$$

Where k and α are empirical constants.

Since low porosity is obtained usually only at the expense of considerable grain growth, [Knudsen, 1959], suggested that the fabrication of high-strength specimens depends, in part, on achieving the optimum balance between decreasing porosity and increasing grain size. To achieve such an optimal balance, it is important to monitor the rate of firing, cooling and peak temperatures.

2.4.2. Effects of Pore Phase on Elastic Properties of Firebricks

Porosity has a variable and often significant effect on the material's behavior and in recent years, the subject of porosity has received renewed attention especially for ceramics, metals and composites. Materials may be porous because the fabrication process results in pores between particles that were not fully consolidated or they may be porous by design, cellular solids, in order to affect a specific property. The major causes of porosity in ceramics are incomplete powder compaction and local concentrations of organic matter introduced in the original processing, and subsequently lost during firing, leaving behind pores.

Possible advantageous engineering properties that may be realized by taking advantage of increased porosity include improved thermal resistance and resistance to crack growth [Herakovich & Baxter, 1999]. Besides, applications of porous devices such as particulate filters, gas sensors, heat exchangers, building materials, refractories, and catalyst supports etc. require both high porosity and good strength. The ion exchange capacity of ceramic used for the containment of radioactive waste also depends directly on the surface area of open pore channels.

There are some properties that have little, or no, dependence on porosity and these are properties that are mainly determined primarily, or only, by the atoms present, their local bonding, or both. Such properties include molecular weight and lattice parameters. Primary properties such as heat capacity depend mainly, or only, on the amount of the mass present and thus in a way they depend on the amount of porosity. These properties satisfy a rule of mixtures of the pore and solid phases [Rice, 1996a].

On the contrary, physical and mechanical properties, electrical and thermal conductivity as shown by Rice in 1996, have a more complex dependence on porosity since they depend on both the amount of porosity and one or more aspects of the pore character such as pore distribution and pore morphology. For example, whereas single pores whose dimensions are several too many times the grain size can be sources of failure, irregular shaped pores can also be sources of failure leading to low material strength. Thus, apart from the volume fraction porosity, defining and adequately measuring which other pore aspects are pertinent to various properties has been a major challenge in adequately defining, and hence predicting, the porosity dependence of many important physical properties.

The effect of porosity as well as the pore geometry on material properties, especially the elastic modulus, of brittle solids has been the subject of considerable theoretical as well as experimental investigations. The measurement of the elastic moduli is fundamental to understanding and predicting the material's behavior. Since they are related to inter-atomic forces, the elastic moduli govern attainable strengths and stress energy release rate associated with shock, impact, fracture, etc. [Vary, 1988].

2.4.3. Pore Volume Fraction on Elastic Properties

Ceramic materials have been investigated to establish the correlation between the elastic constants usually Young's, bulk and shear modulus or Poison's ratio and pore volume fraction P. The widely used Young's modulus-porosity relationship is the exponential relation 2.11, which was obtained by fitting data for aluminum oxide to a single exponential equation [Spriggs, 1961].

$$E = E_0 \exp(-bp) \hspace{4cm} 2.11$$

In equation 2.11 above, E is Young's modulus of a porous specimen, E_0 that of a fully dense specimen and b is an empirical constant. Equation 2.11 above was derived on a purely empirical basis until recently when Anderson in 1996 analytically derived it. Spriggs equation is applicable when the packing geometry and the shape of the pores remain unchanged as the volume fraction porosity changes. Spriggs did not give the exact significance of, b, but he suggested that it may be associated with the fabrication technique and it is related to the proportions of closed and open pores, or to the proportions of continuous solid-phase structure and continuous pore-phase structure. Equation 2.11 has been shown to represent the relation between porosity and modulus of elasticity in various brittle solids fairly well [Coquard et al, 1994; Soroka & Sereda, 1967; Knudsen, 1962]. For example, Soroka and Sereda in 1967 investigated the interrelation of hardness and modulus of elasticity with porosity in gypsum systems and found that both the hardness-porosity and the elastic modulus-porosity relationships are best described by Equation 2.11.

Hasselman in 1962 criticized equation 2.11 since it does not satisfy the boundary conditions E=0 at P=1 and instead proposed a general equation based on solutions of the elastic moduli of heterogeneous systems and which satisfies the boundary conditions E=0 at P=1. In his model, he

considered a porous material as a two-phase composite with the second phase comprising of spherical pores. By setting the modulus of voids to zero, the theoretically-based relation proposed by Hasselman in 1962 has the form,

$$E = E_0[1 - \frac{AP}{1+(A-1)P}]$$

2.12

Where A is a constant. This equation was found to describe the data in some rare earth-oxides such as dysprosium oxide, Dy_2O_3, quite well [Manning et al, 1968]. Wong and coworkers in 1984 showed that equation 2.11 holds good only up to a fractional porosity range of $p \leq 0.2$. He further suggested that for correlating data over a wider range of porosity, the value of b in equation 2.11 cannot be treated as a constant nor be considered as a linear function of porosity. By using a phenomenological model, Wong and coworkers in 1984 proposed an expression with a quadratic exponent. In the phenomenological model, the starting powders are assumed to be monosized within a given specimen and are stacked in an identical array. During densification, the area of contact of the neighboring spheres surrounding each powder particle increases until the residual spherical surfaces shrink into points with the transition of the pore structure from interconnected to isolated. Applying Hooke's law to the unit cell cubic array subjected to stress, the semi-empirical expressions for the elastic moduli were approximated by Wong and coworkers in 1984 as:

$$E = E_0\exp[-(BP + CP^2)]$$

2.13

$$G = G_0\exp[-(BP + CP^2)]$$

2.14

Where G is the shear modulus of a porous specimen while G_0 that of a fully dense specimen. The value of the constants, B=3.35 and C=5.48, are approximate equations to the exact solution for both Young's and shear modulus. According to Wong and coworkers in 1984 equation 2.13

41

extends the validity of equation 2.11 up to a fractional porosity range of P≤0.38. For still higher

porosity, Wong and coworkers in 1984 suggested a relation with a polynomial exponent given by

$$E = E_0\exp[-(BP + CP^2 + DP^3 + \cdots)]$$ 2.15

Where B, C, D,...are material constants.

It has been observed that at low volume fraction porosity, Sprigg's equation 2.11, Hasselman's

equation 2.12 and Wang's equation 2.13-2.14 all reduce to an empirical linear relationship of the

form [Pickup, 1997].

$$E = E_0(1 - a p)$$ 2.16

Where a is a constant. Although equation 2.12 above has no theoretical basis, it has sometimes

been used to describe the elastic modulus-porosity relationship in some rare earth oxides

ceramics such as polycrystalline yttrium oxide Y_2O_2, dysprosium oxide Dy_2O_3, holmium oxide

HO_2O_3 and erbium oxide Er_2O_3 [Manning et al, 1968].

Phani and Niyogi in 1987 observed that most of the above equations proposed to describe the

elastic-modulus porosity relationship of brittle solids are not applicable to all ceramic materials

over a wide range of porosity. For example, they noted that the exponential relation 2.11 and

Wong's equations 2.13-2.15 do not obey the boundary conditions E=0 at P=1 and are not valid

over a wide range of porosity. In addition, due to the infinite number of terms, the material

constants B, C, D, etc., in equations 2.13-2.15 lose their physical significance. Hasselman's

equation 2.12, though it satisfies the boundary conditions E=0 at P=1, yields unrealistic values of

E_0 when fitted over a wide range of porosity. This behavior was attributed to the transition of the

pore structure from interconnected to closed pores which are not accounted for in the derivation

equation 2.12 [Wong et al, 1984]. According to Phani and Niyogi in 1987 the evaluation of the elastic modulus by extrapolation following the empirical and semi-empirical equations 2.11-2.16 may yield inaccurate or unrealistic values of the same. With a view to resolving the shortcomings of equations 2.11-2.16, Phani and Niyogi in 1987a, proposed a semi-empirical relation of the form

$$E = E_0(1 - \beta P)^M \qquad\qquad 2.17$$

Where M is a constant dependent on material's grain morphology and pore structure, defined as packing geometry factor. M lies between 2 and 3 for relatively ordered and less open pore structure and is higher than these values for a disordered and interconnected pore structure [Phani & Niyogi, 1987a]. β is a constant related to the packing density ($1 \leq \beta \leq 3.85$). Equation 2.17, shows that $E = 0$ at $\beta = 1/P_{crit}$ where P_{crit} is the critical porosity at which elastic modulus goes to zero. For values of $\beta \leq 1$, P_{crit} becomes ≥ 1, i.e. the material attains a zero modulus at a critical volume porosity ≥ 1. Since this is in contradiction with the physical reality, for values of $\beta \leq 1$, the parameter of the equation 2.17 are evaluated by taking $\beta = 1$ [Phani, 1996].

Phani and Niyogi in 1987, have shown that equation 2.17 provide the best fit to the experimental data of α- and β-alumina over the entire range of porosity compared to equations 2.11, 2.12 or equation 2.13. Equation 2.17 was also to agree well with the data on rare earth oxides such as samarium oxide Sm_2O_3, lutetium oxide Lu_2O_3, ytterbium oxide Yb_2O_3, dysprosium oxide Dy_2O_3, erbium oxide Er_2O_3, scandium oxide Sc_2O_3 over a wide range of porosity, $0 < P < 0.4$ [Phani & Niyogi, 1987b]. In recent years, Wagh and coworkers in 1991, adopted a model which is a modification of one originally proposed by Wong and coworkers in 1984 to explain the

electrolyte conductivity and fluid permeability through pore channels in rocks, and derived the Young's moduli-porosity relation of the form,

$$E = E_0(1 - P)^\eta \qquad\qquad 2.18$$

Where η is a constant and is a measure of the randomness or skewness of the pore structure in the material. In their model, Wagh and coworkers in 1991, assumed that open pores exist at low volume porosity while closed pores, if present, are few in proportion to the total porosity and hence, their effects are negligible. Further, unlike in equation 2.17, the model proposed by Wagh and coworkers in 1991, takes into account the microstructure through the assumption of random size and shape of pores and random pore size distribution. Through fitting of equation 2.18 to various experimental data, Wagh and coworkers in 1991 noted that for ceramics fabricated without sintering aids or by hot pressing, η was approximately 2 as shown in Table 5. Higher values of η were obtained in cases where sintering aids were used and this was attributed to accelerated densification, more randomness, due to applied external pressure [Wagh et al 1991]. Equation 2.18 was also found to describe better the Young's modulus-porosity relationship of siliceous electrical porcelain into which spherical pores of different size ranges were introduced [Pick-up, 1997]. In this case, the E_0 values obtained using this equation was more consistent with Pickup's experiment data compared to E_0 values obtained by fitting either equation 2.11 or 2.12. Based on the theory of composites i.e. by considering a ceramic material as made up of the matrix and pores, Augusto and Coworkers in 1992 proposed equation 2.19 to describe the porosity dependence of elastic moduli in porous materials such as concrete. In this case, the pores in the material were considered as randomly distributed, fluid-filled voids of irregular shapes and various sizes.

Table 5: Exponent Values η Obtained by Fitting Wagh's Equation 2.16 with Various Experimental Data by Linear Regression Analysis

Material	Porosity range	η	Comments
α-alumina	0.22-0.43	2.14	Consistent with conductivity data
β-alumina	0.02-0.41	4.12	Sodium aluminate as glassy phase
Y_2O_3	0.03-0.19	2.02	Pure oxide
Er_2O_3	0.11-0.30	2.14	Pure oxide
Dy_2O_3	0.07-0.38	2.47	Pure oxide
Ho_2O_3	0.01-0.18	2.40	Pure oxide
SiC	0.02-0.16	3.80	Hot pressed
Si_3N_4	0.20-0.20	2.58	Reaction bonded
Si_3N_4+MgO	0.08-0.45	5.48	Hot pressed, sintering aid used
$Si_3N_4+CeO_2$	0.02-0.38	4.20	Sintering aid used
$Si_3N_4+Y_2O_3+SiO_2$	0.00-0.12	3.81	Sintering aid used
UO_2	0.02-0.06	2.27	Pure oxide
$YBa2Cu3O_{7-\delta}$	0.07-0.301	2.05	Oxide mixture

[Source: Wagh et al, 1991]

$$E = E_0(1 - kP^{2/3}) \qquad\qquad 2.19$$

In the above expression, k is a constant dependent on the average void properties of the material [Augusto et al, 1992]. Still on the theory of composites, Sudduth in 1995 proposed a Young's modulus-porosity relationship for ceramic materials that has the form:

$$\ln(E/E_0) = \left(\frac{[E]P_i}{\xi-1}\right)\left\{\left([P_i - P]/P_i\right)^{1-\xi} - 1\right\} \qquad\qquad 2.20$$

For $\xi \neq 1$

And

$$\ln\left(\frac{E}{E_0}\right) = -[E]P_i \ln(\frac{P_i - P}{P_i}) \text{ For } \xi = 1 \qquad 2.21$$

Where

$$[E] = -\frac{15(1 - \upsilon_0)}{7 - 5\upsilon_0} \qquad 2.22$$

And is defined as the intrinsic modulus i.e. the initial slope of the equations 2.20 and 2.21 at particle concentrations near zero. υ_0 is the Poisson's ratio of the matrix, ξ is the porosity interaction coefficient, P_i is the void content of the starting powder and is the maximum porosity expected during ceramic processing. In general, P_i is the critical porosity, P_{crit}, at which the modulus of a porous solid approaches zero.

Sudduth in 1995 found that by varying the porosity interaction coefficient ξ appearing in equation 2.20 and 2.21, he could recover equations previously used to predict modulus-porosity dependence for ceramics. For example, if $\xi = -1$, equation 2.13 was recovered; if $\xi = 0$, equation 2.11 results; and if $\xi = 1$, equation 2.17 is recovered. An inconsistent already noted by Sudduth himself, is that though he obtained an excellent fit of Wang's data to his equation, the resultant parameters yielded unrealistic values of Poisson's ratio $\upsilon = 0.72$ and 2.55 which were out of the accepted range of $-1 < \upsilon < 0.5$ [Arnold et al, 1996]. In practical ceramic bodies, however all the required conditions such as isolated and closed spherical pores are not fully realized. For example, the shape and size of particles and the densification mechanism produce changes in the pore morphology during the sintering process resulting in random microstructures with random

pore shapes, sizes and pore distributions. In the next section, the proposed forms of equations attempt to incorporate parameters such as the pore structure and geometry in the Young's modulus-porosity relationships are presented.

2.4.4. Effect of pore Geometry on Elastic Properties

From the existing literature data on porous materials, studies have shown that the relationship between the elastic moduli and porosity for what is believed to be the same material varied for different investigators, suggesting that other microstructural characteristics may be important in such a relationship. Not much work, however, has been done to correlate microstructural and morphological features with elastic property variations in ceramic materials and only recently has the effect of pore geometry on material properties of porous brittle materials received some attention. Thus, for accurate prediction of the effect of porosity on the elastic moduli, the role of pore geometry upon the modulus-porosity relation ought to be taken into account [Boccaccini, 1999; Boccaccini & Boccaccini, 1997; Maitra & Phani, 1994; Dean, 1983].

To allow for the effect of pore morphology on the elastic moduli, Wu in 1966, for example, extended the Self-Consistent Scheme, SCS, theory to treat spheroidal inclusions using the 'effective' aspect ratio, α, of the porosity as the adjustable parameter. The self-consistent theory assumes that two types of spherical scatterers i.e. pore and the solid phases are present in a porous material and both of these scatterers are deviations from the effective properties of the medium. Whereas the scatterers, spheroids, may have different aspect varying over a wide range, their effect on elastic properties is approximated by an effective' aspect ratio, α, which replaces the spectrum of aspect ratios. Spheroids, defined as objects with regular mathematically definable geometry that have the same surface-to-volume ratio as the real grains/pores, are characterized by the ratio of the minor axes to the major axes, the aspect ratio, α. For $\alpha=1$, the

spheroids become spheres and as α approaches zero, oblate spheroids become disc-shaped and prolate spheroids become needle-shaped shown in Figures 4 and 5 below.
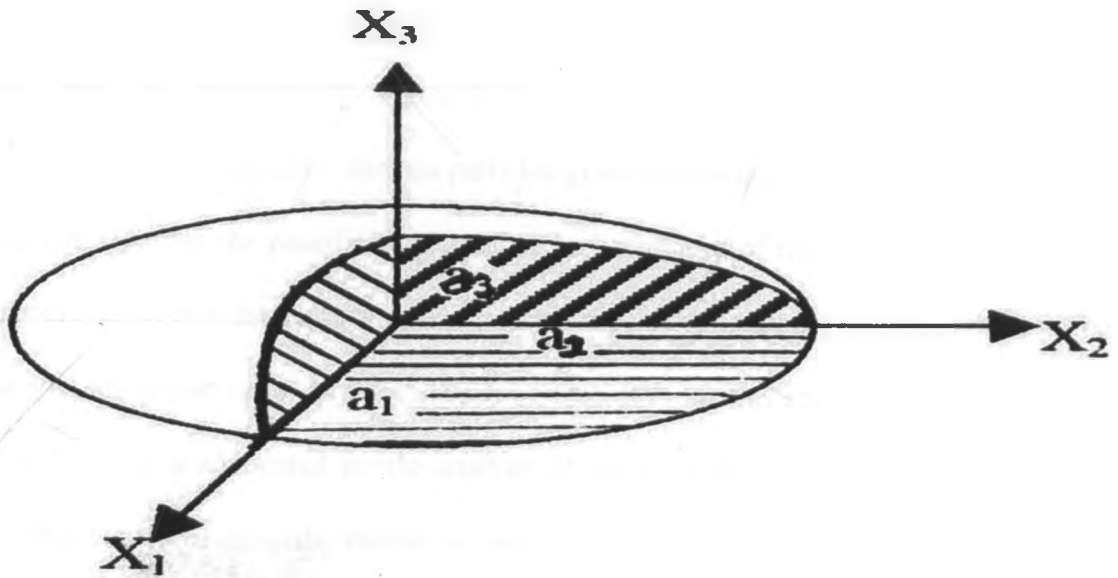
Figure 4: Oblate Spheroid
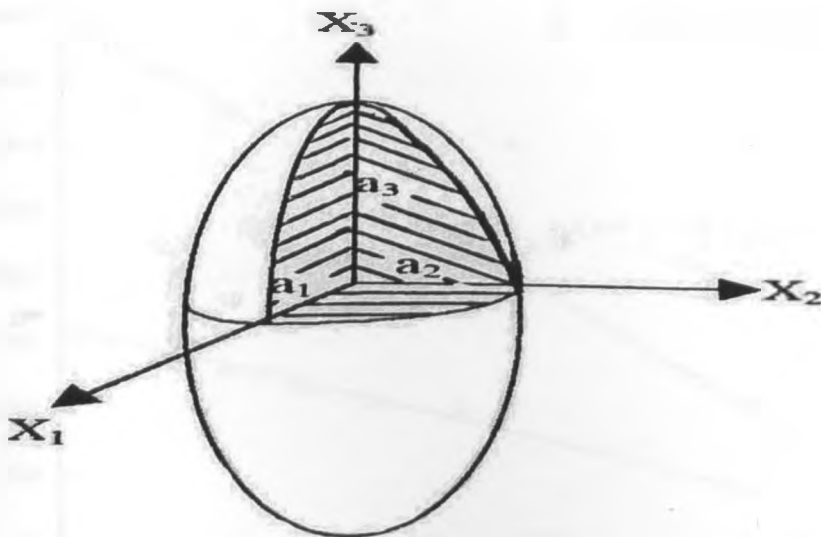
Figure 5: Prolate Spheroid

The SCS has with varying degree of success, been applied by a number of authors in an attempt to analyze the experimental data of sintered ceramics [Phani, 1996; Maitra & Phani, 1994; Pannakkal, 1991; Dean, 1983]. By using an 'effective' aspect ratio, α, as the only variable parameter, Dean in 1983, obtained excellent agreement between theoretical and the experimental elastic modulus data for six types of data sets, one data set each for Al_2O_3 and MgO, and two sets for $MgAl_2O_4$ and ThO_2 respectively. Figure 6 shows some of the results obtained by Dean in 1983. In practice, the complexities, such as particles/grains rearrangement during sintering occur which consequently alter the coordination number and structure of the compact resulting in a variable aspect ratio within the samples. Therefore the assumption that all pores can be described by a single porosity aspect ratio may not always be true. It is for this reason that Martin and his coworkers in 1996 have advocated for the analysis of the modulus-porosity data on a point-by-point basis, that is, determining the moduli at each porosity value using the value of the aspect ratio that provide the best fit with the theoretical prediction.
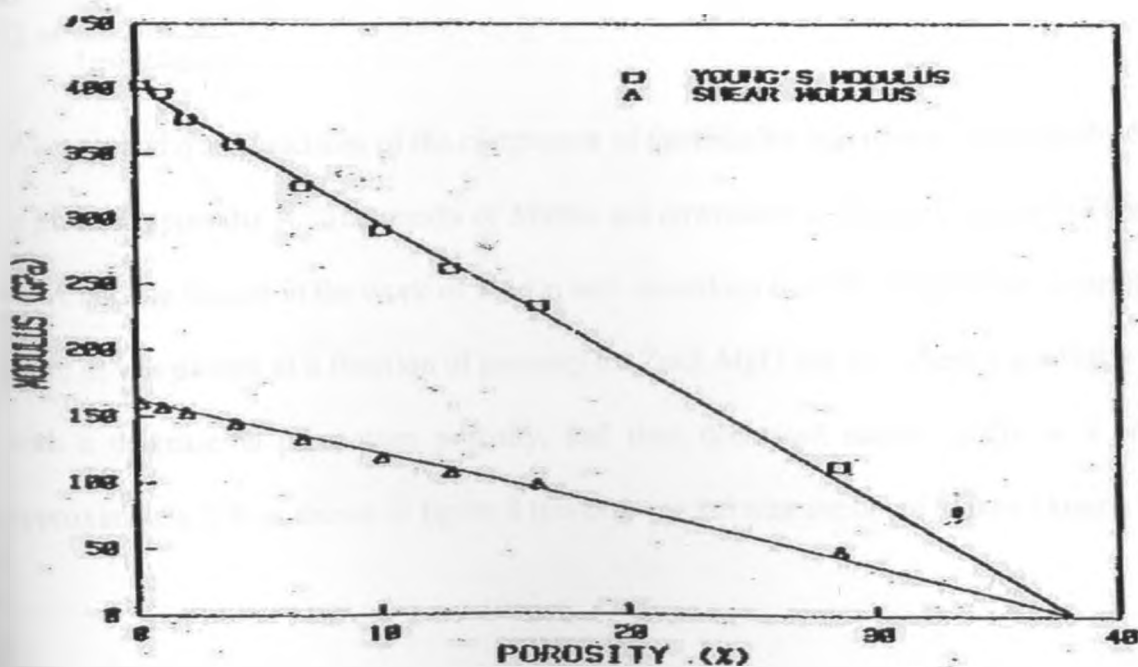
Figure 6: Al_2O_3 Data

N/B: Constants used for theoretical curves are; bulk modulus at zero volume porosity, $K_0 =$ 251.0 GPa, shear modulus at zero volume porosity, G0=162.9 GPa and aspect ratio used is 0.291 [Dean, 1983].

Martin and other coworkers in 1996 have shown that by assigning each datum point a specific aspect ratio, and applying the Mori-Tanaka Scheme, MTS, based-equation, a better fit to the ZnO elastic modulus data is obtained. The MTS approximate the effective elastic properties of a two-phase composite by assuming that both the inclusion and the matrix are subjected to an effective stress field, unlike the self-consistent schemes which focuses on the idea that the effective matrix is the one subjected to the stress field. The Mori-Tanaka Scheme theory can be focused to account for pore-pore interactions at finite concentrations by treating the porosity as ellipsoidal inclusions. The formulations of the MTS theory for isotropic effective moduli of a solid with randomly oriented spheroidal voids are given by [Mori & Tanaka, 1973].

$$K = \frac{K_0}{1 - P(g, S_{ijkl})p} \qquad\qquad 2.23$$

$$G = \frac{G_0}{1 - q(g, S_{ijkl})p} \qquad\qquad 2.24$$

Where p and q are functions of the component of the Eshelby S_{ijkl} tensor. The Eshelby S_{ijkl} tensor is given in appendix A. The results of Martin and coworkers in 1996 are shown in Figures 7 and 8. A notable feature in the work of Martin and coworkers in 1996 is that when a variable aspect ratio, α, was plotted as a function of porosity for ZnO, MgO and Fe, where α gradually increased with a decrease in percentage porosity, and then decreased rather rapidly at a porosity of approximately 5 % as shown in figure 8 this observation was attributed to pore closure.
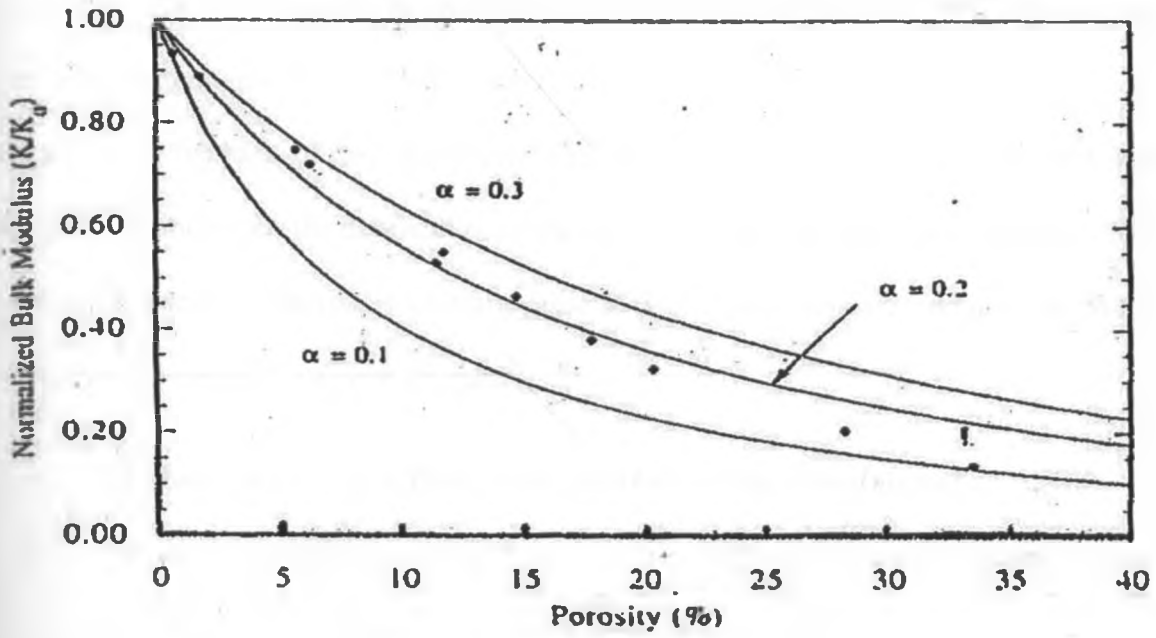
Figure 7: Normalized Bulk Modulus against Porosity of ZnO.

N/B: Curves indicate MTS prediction for α=0.1, 0.2 and 0.3 [Martin et al, 1996]
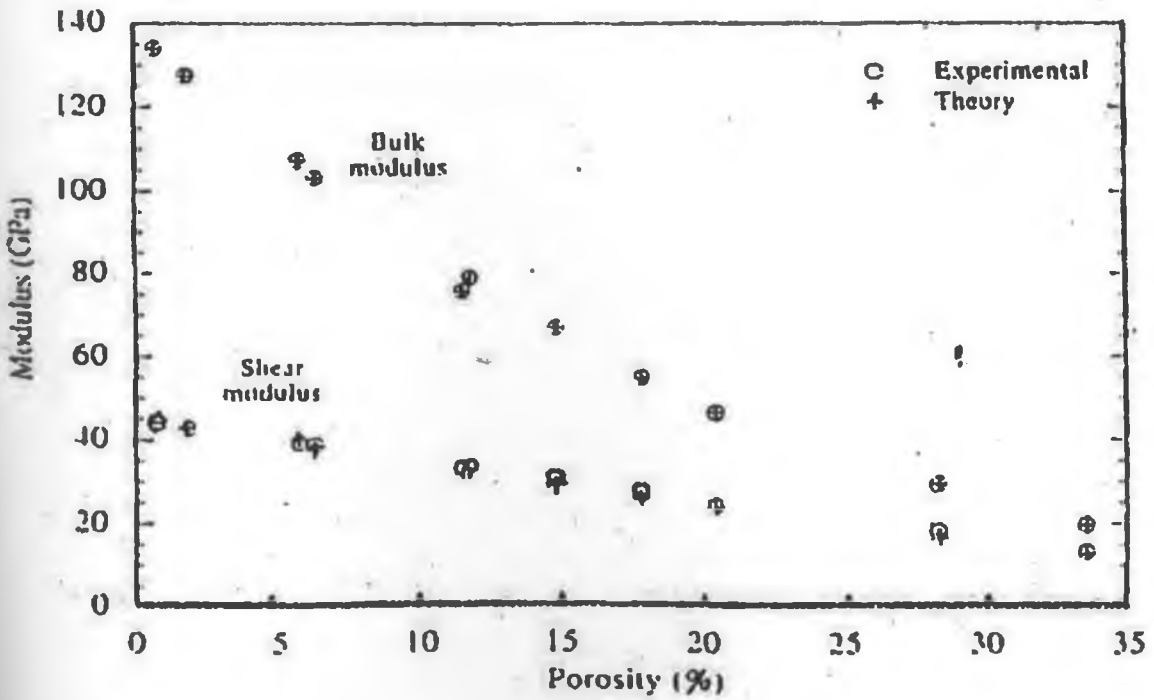
Figure 8: Bulk and Shear Moduli against Porosity of ZnO and MTS Prediction using Point

by Point Calculation Aspect Ratio

According to Boccaccini in 1999, the parameters that characterize the porosity structure for materials containing closed isolated porosity are the distribution, size and orientation of the pores. It is on the basis of these parameters that Boccaccini and his coworkers in 1993 derived analytical formulae for the dependence of the effective Young's modulus on porosity. They considered a porous material as a limiting case of two-phase composite and used the following two factors to describe the pore structure:

I.   The shape factor, z/x, defined as the axial ratio of the spheroids and,

II. The orientation factor defined as $Cos^2 \varphi$, where φ is the angle between the stress direction and the rotational axis of the spheroids.

Figure 9 shows point by point fitting results in a better fit to the experimental data compared to the predictions based on using the 'effective' aspect ratio, α.
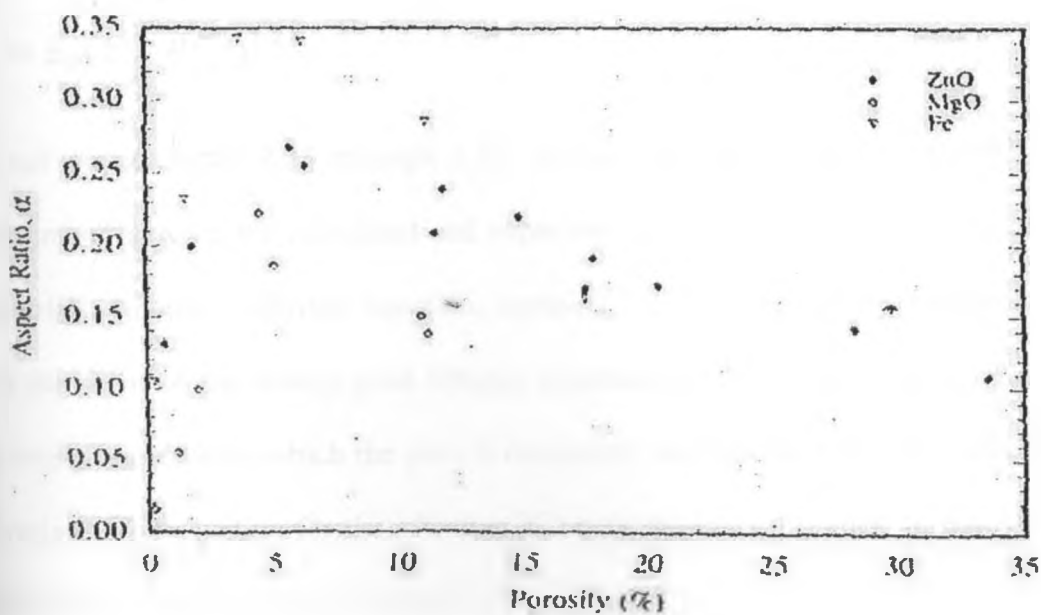
Figure 9: Point by Point Calculation of Optimum Aspect Ratio Fitting MTS Theory to Experimental Modulus Data of ZnO, MgO and Fe.

The general analytical formulae derived by Boccaccini and coworkers in 1993 for materials with closed porosity have the form.

$$E = E_0(1 - P^{2/3})^S$$

2.25

Where

$$S = 1.21[\tfrac{Z}{X}]^{1/3}\sqrt{1 + ([\tfrac{Z}{X}]^{-2} - 1)cos^2\Phi}$$

2.26

Equation 2.25 satisfies the boundary conditions E=0 at a volume fraction porosity p=1 but does not consider pore interactions and intersections that occur at high porosity and is therefore limited to a volume fraction porosity range of approximately $0 \leq P \leq 0.4$. Details of its derivation are found in the work of Mazilu and Ondracek in 1989. The case of random statistical orientation i.e. isotropic materials is obtained by setting $cos^2\varphi = 0.33$. For the special case of spheroidal porosity, z/x=1 and $cos^2\varphi=0.33$ and in this case, Equation 2.25 takes the form

$$E = E_0(1 - P^{2/3})^{1.21}$$

2.27

Based on equations 2.25 through 2.27, Boccaccini and coworkers in 1993 obtained good agreement between the calculated and experimental Young's modulus values of some ceramic materials. Another analytical equation, equation 2.28 was derived by Anderson in 1996 and it has the form of the widely used Spriggs exponential relationship. Anderson assumes a large isotropic body within which the pore is contained, and that the remotely applied stress remains invariant. The equation for the effective Young's modulus, En after, n, pores is incrementally introduced takes the form, for large n:

$$E = E_0 \exp\{-bp\}$$

2.28

53

Where

$$b = 1 + \frac{4(1-\upsilon^2)}{3\pi}\left(\frac{E(\alpha)+\pi(\alpha)}{\alpha E(\alpha)}\right) \quad \text{For randomly oriented pores} \qquad 2.29$$

And

$$b = 1 + \frac{2(1-\upsilon^2)}{\alpha}\left(\frac{2}{\pi}\cos^2\Phi + \frac{\alpha}{E(\alpha)}\sin^2\Phi\right) \quad \text{For aligned pores} \qquad 2.30$$

In the above equations, E (α) is the complete elliptical integral given by Abramowitz and Stegun in 1972.

$$\int E(\alpha)d\alpha = \pi\alpha/2\left[1 - \sum_{j=1}^{\infty}\left[\frac{2j]^2\alpha^{2j}}{(4j^2-1)2^{4j}(j!)^4}\right]\right] \qquad 2.31$$

While α is the aspect ratio. Anderson has shown that in this case, the exponential constant b is a function of the pore shape and the orientation of the pores with respect to the stress axes and is independent of pore size.

2.4.5. Effects of Pore Phase on the Mechanical Strength of Ceramics

Most ceramic materials are composed of two or more phases that differ in physical and chemical properties. Under mechanical loading, differences in elastic properties of individual components of a ceramic body lead to stress in-homogeneities generally referred to as 'stress concentrations'. For example, if there is any geometric discontinuity such as a pore or void, there is a stress concentration near the defect that is void and the true stress in the material is higher near the defect. At a far distance from the defect, the stress is uniform as if there were no defects in the material. A part from increasing the mean value of the stress transferred across material bridges between pores, porosity reduces the effective cross—sectional, load-bearing, areas. The minimum solid load bearing area is the actual sintered or the bond area between particles in the case of stacked particles and the minimum web cross-sectional area between pores in the case of

stacked bubbles. Several studies have suggested the dependence of mechanical strength of ceramics on the minimum solid load bearing area [Rice, 1997; Rice, 1996a; Rice, 1996b; Rice, 1993a; Rice, 1993b; Knudsen, 1959]. Rice in 1996 further suggested that the minimum solid contact area, MCA, models are applicable not only to stress determined that is mechanical properties such as elastic moduli e.g. Young's, shear or bulk modulus; tensile/ flexural and compressive strength; but also to flux determined properties such as electrical and thermal conductivity. The minimum solid area model that is based on various pore models that are generally most pertinent are shown in Figure 10 on a plot of the log of the property versus volume fraction porosity P. A basic characteristic of all these models is that the minimum solid area and hence the pertinent property value of interest decreases first, approximately, though not exactly, along straight lines on the semi-log plot. Beyond this approximately linear region the property of interest decreases more rapidly, and then more precipitously, going to zero at a critical porosity P_{crit}. For stacked particles, P_{crit} is where the bond area between particles goes to zero. For pores e.g. bubbles in a matrix, it is the point at which the minimum web area between particles goes to zero.

On the contrary, other studies have suggested that the behavior in mechanical strength of ceramic materials with porosity is the result of stress concentrations mainly from the pores [Boccaccini, 1998; Maitra & Phani, 1994; Boccaccini, 1994; Ramakrishnan & Arunachalam, 1993; Nielson, 1984; Hasselman & Fulrath, 1967]. For example, Kubicki in 1995 observed that the elastic modulus and tensile strength of a porous material decreases at a rate more than twice the effective cross-sectional area as porosity increases and attributed this to the effect of stress concentration from pores as portrayed in Figure 11.
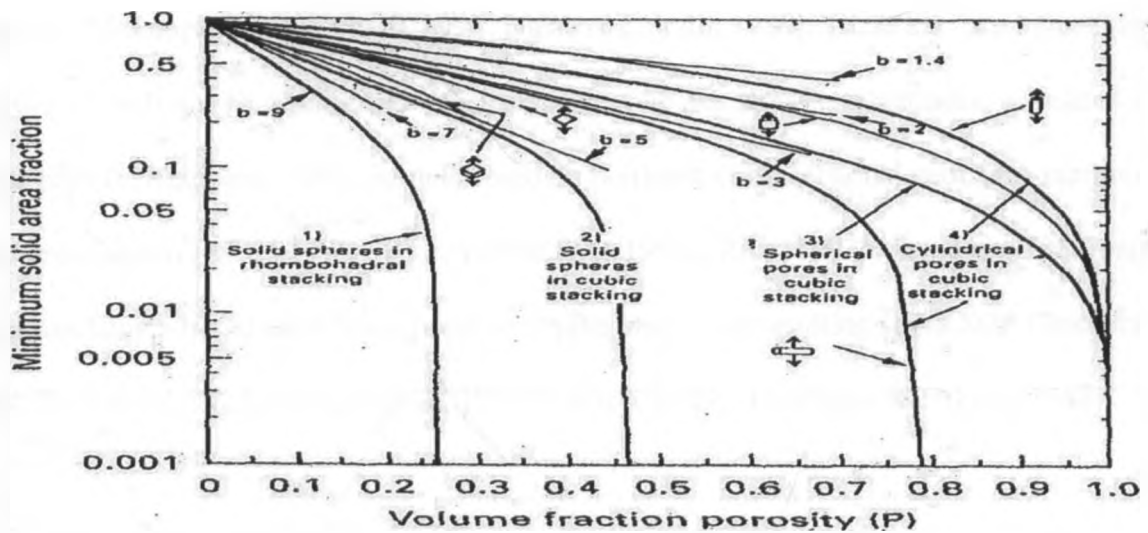
Figure 10: Minimum Solid Areas against Volume Fraction Porosity Calculated for various uniform Stackings of Perfectly Uniform Spherical Particles or Cylindrical or Cubic Pores

N/B: Most relative physically properties i.e. the value at the same P divided by the value at P=0 dependent on the local stress or flux should be directly related to the relative minimum area, i.e. the ratio of the minimum solid area at a given p value to that at p=0 [Rice, 1996b].
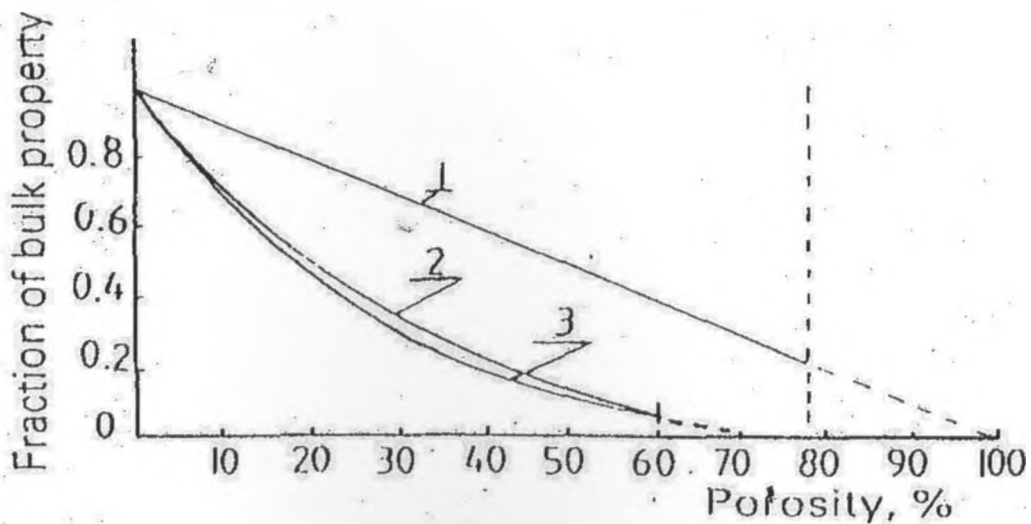
Figure 11: Variations of Effective Cross-sectional Area (1), Elastic Modulus (2), and Tensile Strength (3) against Porosity

Generally, three approaches have been adopted to deal with mechanical property-porosity relations [Mukhopadhyay & Phani, 1998; Dipac & Fulrath, 1980]. These are: mechanical strain analysis of bodies with generalized structure neglecting any stress concentration or related pore shape effects [Knudsen, 1959]; models based on pertinent cross sectional geometry minimum solid area models [Rice,, 1996a; Rice, 1996b; Rice 1993a; Rice, 1993b; Knudsen, 1959]; and micromechanics-based models i.e. premise of pore shape and resulting stress SCE [Boccaccini, 1994; Ramakrishnan & Arunachalam, 1993; Nielsen, 1984; Hasselman & Fulrath, 1967].

2.5. Instrumentation

2.5.1. Atomic Absorption Spectrophotometer

Atomic absorption spectroscopy is a spectroanalytical procedure for the quantitative determination of chemical elements employing the absorption of optical radiation by free atoms in the gaseous state. This method was first used as an analytical technique, and the underlying principles were established in the second half of the 19th century by Robert Wilhelm Bunsen and Gustav Robert Kirchhoff [Varian, 1979].

This technique is based on the principle that the electrons of the atoms in the atomizer can be excited to higher orbitals for a short period of time normally nanoseconds by absorbing a radiation of a specific wavelength. Spectral lines (wavelengths) do overlap but it is possible to select a characteristic wavelength for each element which gives the technique its elemental selectivity.

The radiation flux without a sample and with a sample in the atomizer is measured using a detector, and the ratio between the two values of absorbance is converted to analyte concentration or mass using the Beer-Lamberts Law. In optics, the Beer Lambert law, also known as Beer's law or the Lambert-Beer law or the Beer-Lambert-Bouguer's law, named after August Beer, Johann Heinrich Lambert, and Pierre Bouguer, relates the absorption of light to the properties of material through which the light is travelling. The law states that there is a logarithmic dependence between the transmission or transmissivity, T, of light through a substance and the product of the absorption coefficient of the substance, α, and the distance the light travels through the material i.e. the path length, ℓ. The absorption coefficient can, in turn be written as a product of either a molar absorptivity/ extinction coefficient of the absorber, ε, and

the molar concentration, c, of absorbing species in the material, or an absorption cross section, σ, and the number density N' of absorbers[Ullmann's 1994].

The Beer-Lambert law equation for the liquid solution is expressed as,

$$A = -log_{10}\left(\frac{I}{Io}\right)$$ 2.32

Where A is absorbance, Io and I, is the intensity of the incident and transmitted light respectively. Figure 12 below is a schematic diagram of Atomic Absorption Spectrophotometer Cross Section.
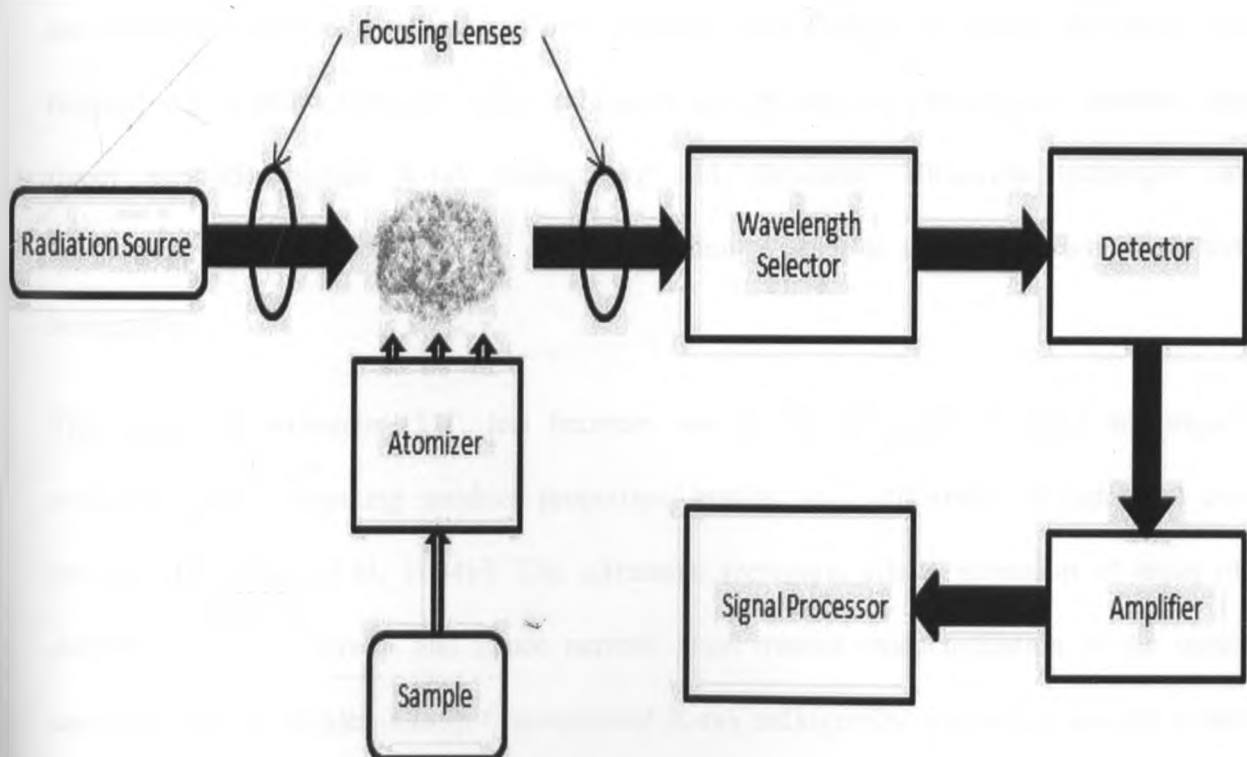
Figure 12: Atomic Absorption Spectrophotometer Cross-Section

2.5.2. Non-Destructive Evaluation of Materials

Despite the fact that most ceramics are hard, wear and corrosion resistant and can withstand high stresses at elevated temperatures, these materials are brittle and consequently, very small defects, which may have been introduced during manufacture or service, can lead to catastrophic failure. Ceramic materials therefore require non-destructive evaluation, NDE, techniques to evaluate their material property. For example, tensile strength tests produce poor results as a result of flaws that might be introduced during shaping of the samples for tensile test. NDE, by definition does not damage the component under inspection.

The objective of most NDE for ceramic materials is the detection of cracks, porosity inclusions and characterization of physical and mechanical properties such as density and elastic moduli respectively. Various types of NDE techniques can be used to characterize ceramics and the major methods include X-ray radiography and ultrasonic. Ultrasonic technique can be subdivided, and to it added a new range of technique such as acoustic emission method and holography.

The ultrasonic technique, UT, has become one of the generally accepted techniques for evaluating and comparing product properties, quality and uniformity of industrial ceramic products [Kulkarin et al, 1994b]. The ultrasonic technique allows detection of areas of low density, and other defects and hence permits good overall characterization of the quality of ceramics [Aly & Semler, 1985]. Conventional X-ray radiography consists of passing a beam of X-rays through the part to be examined to expose a sheet or film. Density variations in the material for example, can be detected by the difference in the light intensities of the film with denser regions showing up lighter than the less dense regions. This technique has been considered for the characterization of firebricks.

2.5.3. X-Ray Diffraction Spectrophotometry

XRD is a versatile analytical method used in analysis of phases, elemental oxides and interatomic distances. The atomic planes of a crystal cause an incident beam of x-rays to interfere with one another as they leave the crystal. This phenomenon is known as X-Ray diffraction. Figure 13 is a schematic diagram of X-Ray Diffraction Spectrophotometer.
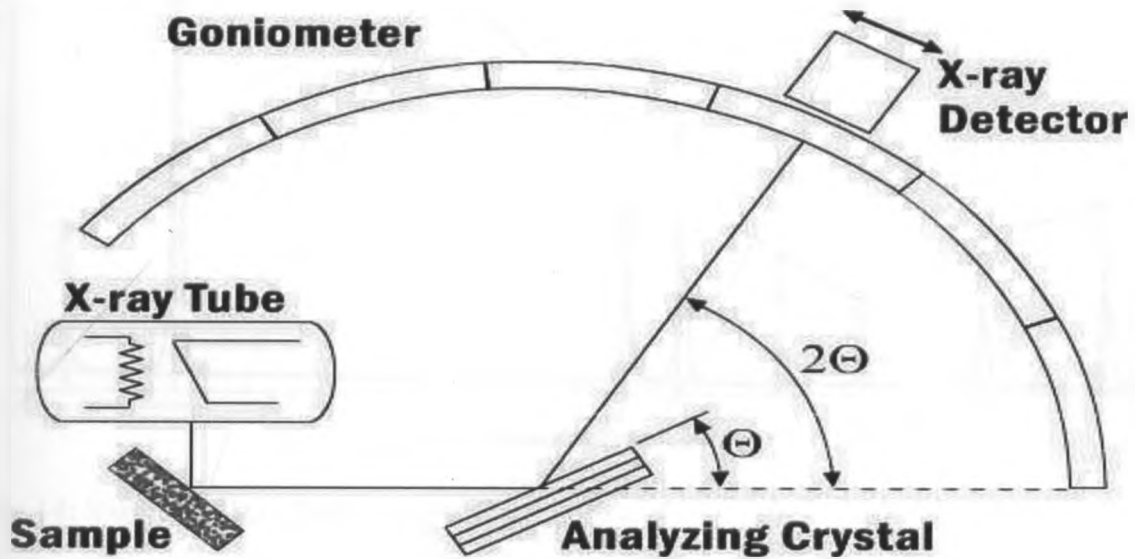
Figure 13: X-Ray Diffraction

X-ray diffraction is a powerful technique for the analysis not only of the structural parameters but also, indirectly, of the actual composition, through comparison of spectra [Suryanarayana & Norton, 1998]. The relation between the reflected X-ray angle, θ, the inter-planar distance, d, and the wavelength, λ, was formulated by Bragg as

$$2d \sin \theta = n\lambda, \; n = 1, 2, 3, \ldots \qquad 2.33$$

From the X-ray spectra it is also possible to extract information about the mean grain size D_{size} through the Scherer's equation, i.e.

$$D_{size} = \frac{K_{scherrer}\lambda}{\Gamma \cos\theta} \qquad 2.34$$

Where $s_{scherer}$ is a dimensionless constant and Γ is the line width [Cullity, 1959].

Figure 14 below shows sample diffractogram, a plot of intensity against 2θ. The diffraction pattern of a mixture is a simple sum of the diffraction patterns of each individual phase. Experimental data are compared to reference patterns to determine what phases are present.
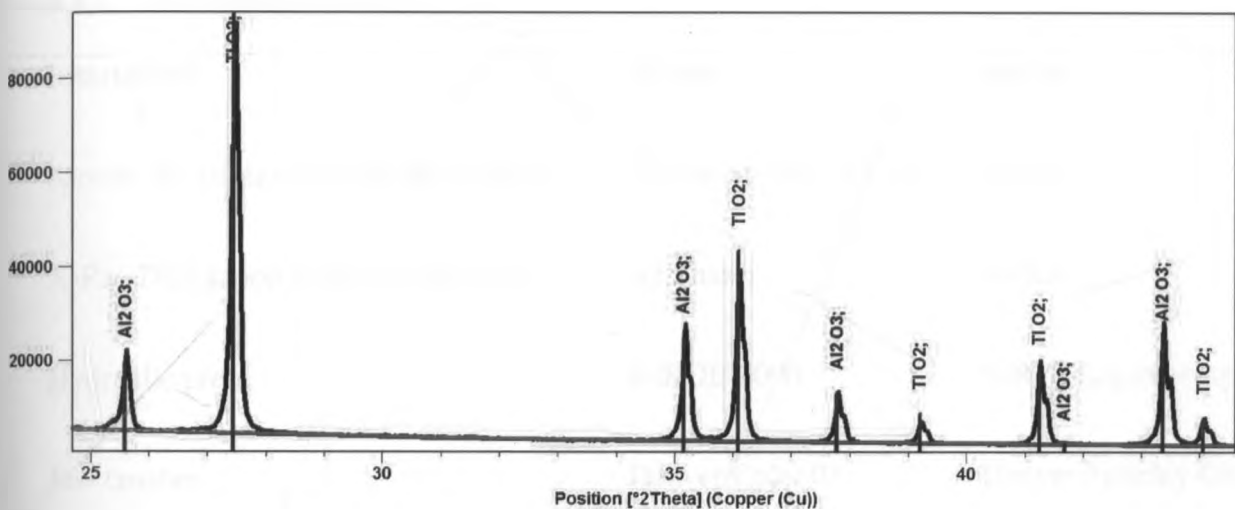
Figure 14: Sample X-Ray Diffractogram

The reference patterns are represented by sticks. The position and intensity of the reference sticks should match the data. A small amount of mismatch in peak position and intensity is acceptable experimental error. Specimen displacement is a systematic peak position error due to misalignment of the sample. Most diffraction data contain K-Alpha 1 and K-Alpha 2 peak doublets rather than just single peaks. The k-alpha1 are peaks always as twice the intensity of the k-alpha2 peaks [Suryanarayana & Norton, 1998]. At low angles 2θ, you might not observe a distinct second peak. You cannot decipher the relative amounts of phases based upon the relative intensities of the diffraction peaks. This is because intenisty of the peak is a function of phase diffraction effivciency, for example, practically TiO_2 pattern compared to Al_2O_3 is more intense because TiO2 diffracts X-rays more efficiently [Cullity, 1959].

Chapter 3

METHODOLOGY

3.1. List of Instruments, Apparatus and Reagents

3.1.1. List of Instruments

Instrument	Model	Source
Atomic Absorption Spectrophotometer	Varian Spectra AA-10	Varian
X-Ray Diffraction Spectrophotometer	D2 Phaser	Bruker
Hydraulic press	KIRDI/ 2000	KIRDI Engineering
Jaw crusher	Denver Colo/ 01	Denver Fireclay Co. Ltd
Steel ball mill	Denver Colo/ 01	Denver Fireclay Co. Ltd
Pan mixer	E-150	Wesman Eng.Ltd
Oven	OV 200 CFD	Gallenkamp Ltd
Furnace	ELF 11/ 6B	Gallenkamp Ltd
Compressive Strength Machine	50-C4600/UP1A	Automax Ltd
Magnetic gyratory separator	9-2-SS	William Boulton Ltd
Attrition Mill	Denver Colo/ 03	Denver Fireclay Co. Ltd

3.1.2. List of Apparatus

Apparatus	Model	Source
Rotary mixer	E6890086	George Forwell Engineering Ltd
Electronic weighing Scale	EKW	Fischer Scientific Ltd
Spring balance	E204567	Fischer Sceintific Ltd
Erlenmeyer flask	Pyrex	Simax Ltd
Micro pipette	E652591	Gilson Ltd
Mild steel mold	KIRDI/2010	KIRDI Engineering
Tailor sieves	BS 410	Tailor Series
Conical flasks	Pyrex	Simax Ltd
pH meter	510	Metler Toledo

3.1.3. List of Reagents

Reagent	Concentration	Source
Hydrochloric Acid	18M	Fischer Scientific
Nitric Acid	23M	Fischer Scientific
Boric acid	99 %	Fischer Scientific
Caesium Chloride	90 %	Fischer Scientific
Hydrofluoric acid	12M	Fischer Scientific

3.2.Sampling

20kgs of Kwale Ilmenite Ore was sourced from Titanium Base Resource Company, 300kgs of Eburru Kaolin and 200kgs of Eburru Fireclay were sampled from Nakuru County and 100kgs of Mukurweini Ball Clay was sampled from Mukurweini, Nyeri County as shown on Figure 15 of the Map of Kenya below.
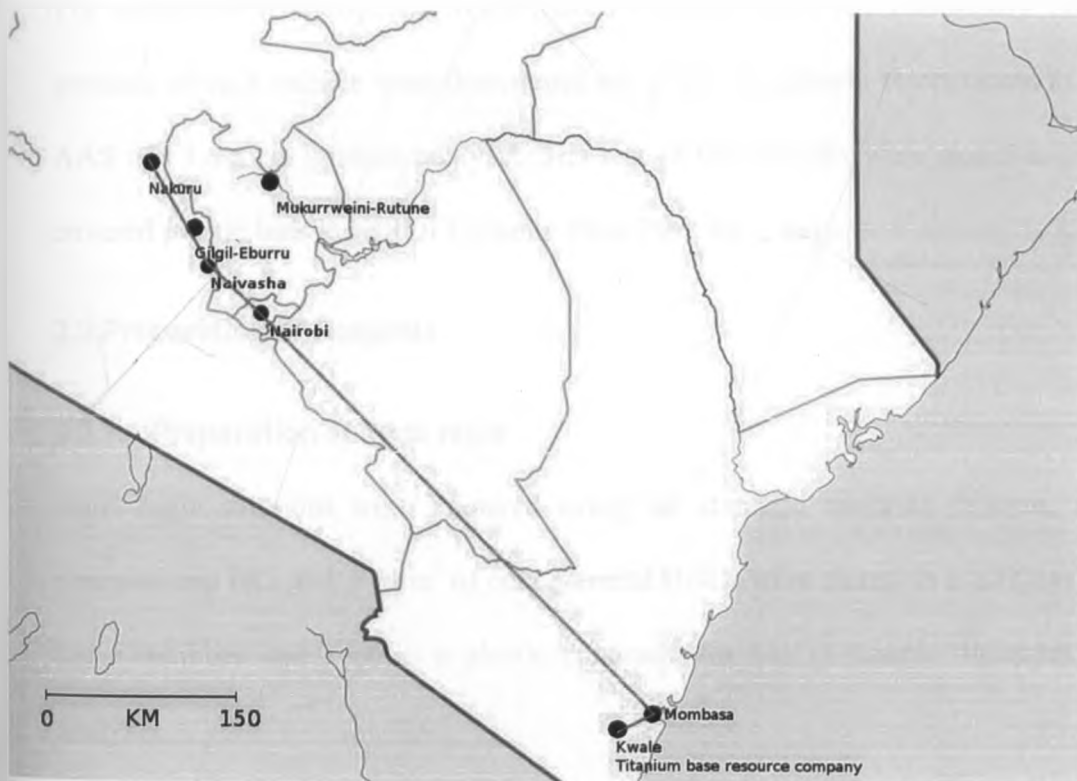
Figure 15: Part of Map of Kenya Showing Raw Material Sampling Sites

Eburru Fireclay was collected approximately 3 to 50cm beneath the surface while Eburru Kaolin was dug 50 to 100cm beneath the surface in the quarry. Mukurweini Ball Clay was collected from Rutune quarry between 15 to 100cm beneath the surface. Open cast method of quarrying was employed to mine the firebrick raw materials from the respective quarries. Before collection the place was cleared to minimize contamination. The samples were dug out using a hard plastic spade and packed in clean sisal sacks and labeled as shown in Table 6 below.

Table 6: Sample Field Coding

Sample	Code
Kwale Ilmenite Titanium Ore	KITO
Eburru Kaolin	EK
Eburru Fireclay	EF
Mukurweini Ball Clay	MBC

The samples were transported to the KIRDI Ceramic Pilot Plant Laboratory. Approximately 1 kg portions of each sample were drawn and left to dry at ambient temperature in the laboratory for AAS and Loss on Ignition analysis. The rest of the samples were stored in clean, labelled and covered plastic bins in KIRDI Ceramic Pilot Plant for 2 days.

3.3. Preparation of Reagents

3.3.1. Preparation of aqua regia

Aqua regia solutions were prepared using the standard methods [Varian, 1979]. $900cm^3$ of concentrated HCl and $300cm^3$ of concentrated HNO_3 were mixed in a $2000cm^3$ conical flask in a fume chamber and kept in a plastic container for use in sample digestion for AAS sample analysis.

3.3.2. Preparation of working standards

The working standards were prepared using standard analytical methods [Varian, 1979]. $250cm^3$ stock solutions of 1000ppm were prepared by weighing a specified amount of analar grade Al_2O_3, SiO_2, Fe_2O_3, NaOH, KOH, CaO, MnO and MgO. They were dissolved in aqua regia and diluted to a $250 cm^3$ in a volumetric flask using de-ionized water. $100cm^3$ secondary stocks of 10 ppm were prepared from 1000 ppm primary stocks by taking $1cm^3$ of each of the stock solution

and diluting it to the mark in 100cm^3 volumetric flask. Working standards of 1ppm, 2ppm, 3ppm, 4ppm and 5ppm were prepared from 10ppm secondary stock solution by taking 1cm^3, 2cm^3, 3cm^3, 4cm^3 and 5cm^3 respectively and diluted to 100cm^3 in the volumetric flask. These standards together with the stock solution were transferred into plastic bottles and used for calibration of AAS.

3.3.3. Preparation of Boric Acid Solution.

320g H$_3$BO$_3$ and 12.65g CsCl were transferred into a 5litre Erlenmeyer flask. 5 litres of distilled water were added and heated to near boiling and then allowed to cool. During this experiment, it was ensured that the undissolved boric acid crystals remained at the bottom of the flask, to retain saturated solution.

3.4. Raw Materials Analysis

3.4.1. Atomic Absorption Spectrophotometer

Samples were analyzed using Varian Flame Spectroscopy Analytical Methods [Varian, 1979]. 30g each of EK, EF, KITO and MBC were weighed and transferred into porcelains labelled EK, EF, KITO and MBC respectively and dried in the oven at 100 ^{O}C for 2½ hours to a constant weight. Each sample was pulverized using an attrition mill into fine powder and sieved using 200μm sieve. 0.1g of the pulverized sample of EK, EF, KITO and MBC were weighed separately into 100cm^3 plastic bottles labelled EK, EF, KITO and MBC, taking care that the samples were dropped into the bottom of the bottles without spreading along the walls. 1 cm^3 of aqua regia solution was added using a plastic tipped pippete into each of the plastic bottles to digest the samples. The bottles were stoppered loosely. The mixtures were allowed to stand overnight and 3cm^3 of HF acid was added into each mixture and the bottles stoppered

immediately to avoid loss of silicon. The mixtures were stirred homogenously using an orbital shaker, while ensuring that there was no spillage. The mixtures were allowed to stand for 12 hours and then heated in the water bath for 2 hours to completely dissolve the sample while keeping the stoppers tightly closed. The solutions were cooled and using an automatic dispenser, 50cm^3 of the boric acid solution was added into each of the mixtures then left to stand for at least one hour. 46cm^3 of water was added using an automatic dispenser into each solution and mixed well. The solution was left to stand for at least 3 hours before AAS analysis was carried out. The blanks were first aspirated and then the instrument adjusted to zero. Each of the prepared standards was then analyzed and a calibration curve drawn. The nebulizer was aspirated with de-ionized water. The blanks for the samples were then ran and the instrument adjusted to zero. Each sample was then analyzed and its absorbance and concentration determined. The total elemental concentrations in ppm were obtained after subtraction of the blank. Since the initial concentration in each sample was different resulting to various dilution factors; the quantities of metals in each sample was expressed as mg/g by taking:

$$\frac{\text{initial volume of the digested sample x exact concentration in ppm x dilution factor x } 10^6}{\text{weight of the sample}} \qquad 2.35$$

3.4.2. Loss on Ignition

The losses on ignition analysis were done as described by Henry A. Leper, (2008) standard analysis method. 5g each of EK, EF, MBC and KITO samples were weighed and transferred separately into the crucibles labeled EK, EF, MBC and KITO respectively. The initial weight of the crucibles and samples were taken. They were transferred into a muffle furnace and heated at 1000 $^\text{O}$C for 1⅔ hours. The samples were left for 12 hours in the muffle furnace to cool to room

temperature. They were then removed and final weight recorded. The percentage Loss on Ignition of samples was calculated as follows.

$$\frac{\text{initial weight of sample} - \text{final weight of sample}}{\text{initial weight}} 100 \qquad 2.36$$

The % composition on dry basis was the composition that did not change with temperature and was calculated as:

$$\text{Composition on Dry Basis} = \left\{\frac{\%\ \text{Elemental Oxide}}{(\%\ \text{Total composition of Raw Samples} - \%\text{Loss On Ignition})}\right\} 100\ \% \qquad 2.37$$

3.5. Formulation

3.5.1. Grog and Binder Formulation

The sample raw materials were separately dried on clean polythene paper sheets for 3 days in the Ceramic Pilot Plant Laboratory away from direct sunshine as shown in figure 16 below.
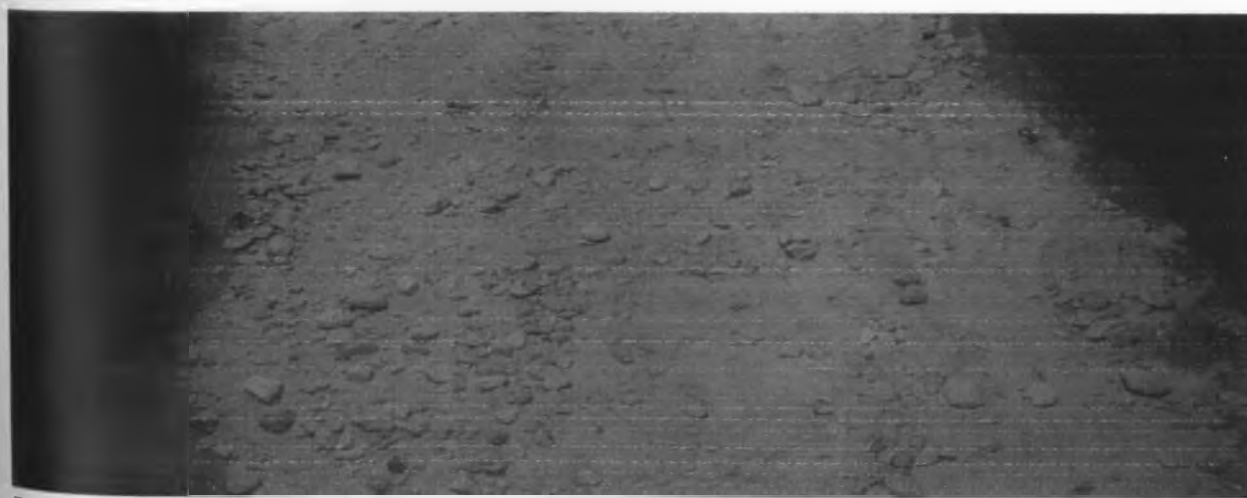
Figure 16: EK Drying in KIRDI Ceramic Pilot Plant

The visible contaminants were removed. The steel ball mill and milling media were thoroughly cleaned using compressed air. 15kgs of EK and 30 liters of water were weighed into the ball mill. The mild steel balls were added and the ball mill tightly closed and milled for 1½ hours.

The ball mill was switched off, contents offloaded and milling media sieved using 3mm sieve. The sample was passed 4 times through a 100μm sieve fitted with a magnetic separator to remove iron fillings. The sample was left to stand for 12 hours undisturbed; water was decanted and sun dried for 7 days at ambient temperature. The procedure was repeated for KITO, EF and MBC. Each dried sample was transferred in plastic containers labeled EK, EF, MBC and KITO respectively for grog and binder formulation.

Material balance using percentage elemental oxide analysis obtained from AAS analysis was used to determine the mixing ratio of EK, EF, MBC and KITO [Harbison, 2005]. Grog was formulated from the EK, EF and MBC, while the binder was made from EK and MBC. Low Fe_2O_3 content in EK and higher Al_2O_3 in MBC and EF made them suitable for grog and binder formulation as shown in Table 10. MBC had higher plasticity index suitable in binding.

To ascertain the mixing ratio of the EK, EF and MBC for formulation of grog, % Fe_2O_3 was used as a basis. Fe_2O_3 content was set at 2.00 % and used as a basis for calculating mixing ratio of EK, EF and MBC to formulate grog [Rahman, 2012]. Percentage Fe_2O_3 content in EK and EF were 0.70 and 2.74 respectively. Setting the % Fe_2O_3 at 1.72 for EF-EK batch mix, the mixing ratios for EK and EF were calculated as:

EK + EF =1

0.7(1-EF) + 2.74EF = 1.72

EF=0.5, and EK=0.5

The EF and EK were mixed in the ratio of 1:1 by weight.

To determine the amount of MBC to be added to EF-EK mixture, Fe_2O_3 content in the EK-EF-MBC mix was set at 2.00% and mixing ratios calculated as:

$3.79MBC + 1.72Fk = 2$

$1.72MBC + 1.72Fk = 1.72$

$2.07MBC = 0.28$, $MBC = 0.14$, $Fk = 0.86$

Hence the mixing ratio by weight of EF, EK and MBC for production of grog was 100:100:33.

To ascertain the mixing ratio of EK and MBC for binder formulation, % Fe_2O_3 in the EK and MBC final batch mix was set at 2.00% and used as a basis to calculate EK and MBC mixing ratio. The Fe_2O_3 content in MBC and EK were 3.79 and 0.70 respectively.

$MBC + EK = 1$, Thus $EK = (1-MBC)$

$3.79MBC + 0.70EK = 2.00$

Hence, $3.79MBC + 0.70(1-MBC) = 2.00$

$MBC = 0.421$, $EK = 0.579$

Hence the mixing ratio of MBC to EK was 6: 4 by weight for binder formulation.

Dry and finely ground 25kgs EF, 25kgs EK and 8.25kgs MBC were weighed and homogenously mixed for about 15 minutes in the pan mixer. The mixture was transferred into a rotary mixer, 15 liters of water was added and mixed thoroughly for 15 minutes. 0.5 kg of the EK-EF-MBC formulation mixture was weighed into the mild steel mold, measuring 10cm by 7.5cm, and pressed into a brick at 50 tons with a hold time of 1 minute using hydraulic press. The hydraulic

press was fitted with a pressure gauge with a range of 0-50 tons as shown in Figure 17 below. The firebricks were then dried in the laboratory away from the sun for 24 hours in the laboratory and then in an oven at 110 ^{O}C for 12 hours. The dried firebricks were then fired at 1200 ^{O}C for 24 hours and allowed to cool to room temperature while in the furnace for 3 days.
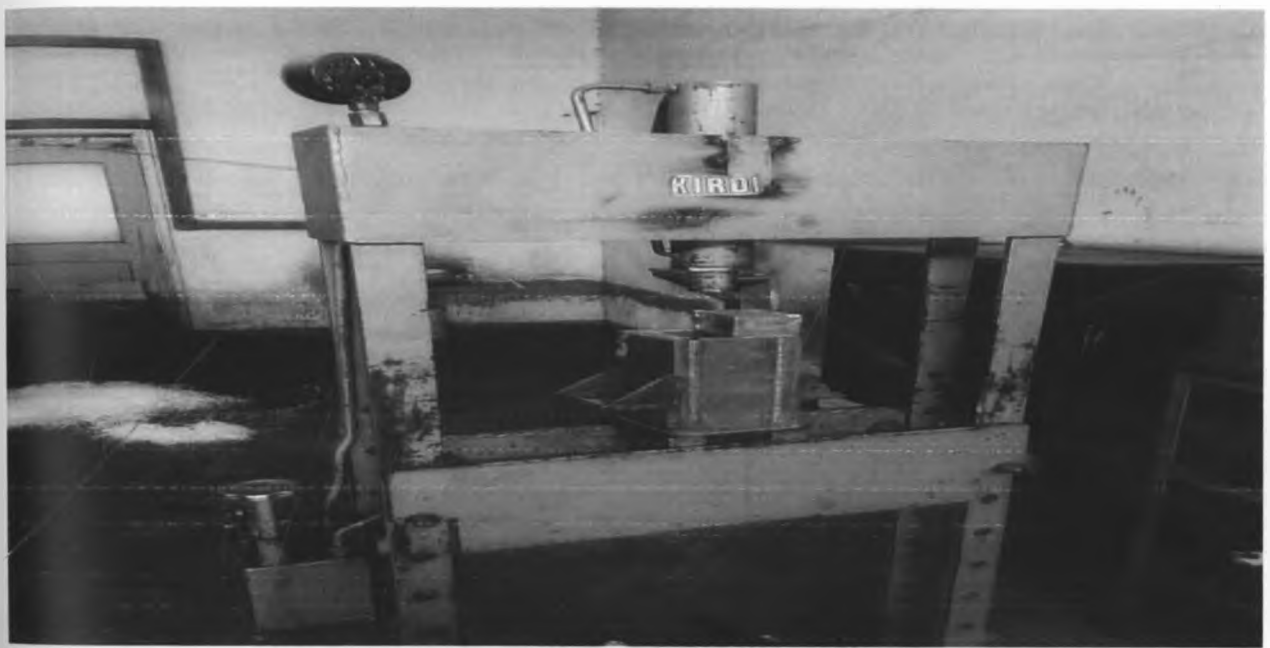
Figure 17: Hydraulic Press in KIRDI Engineering Workshop
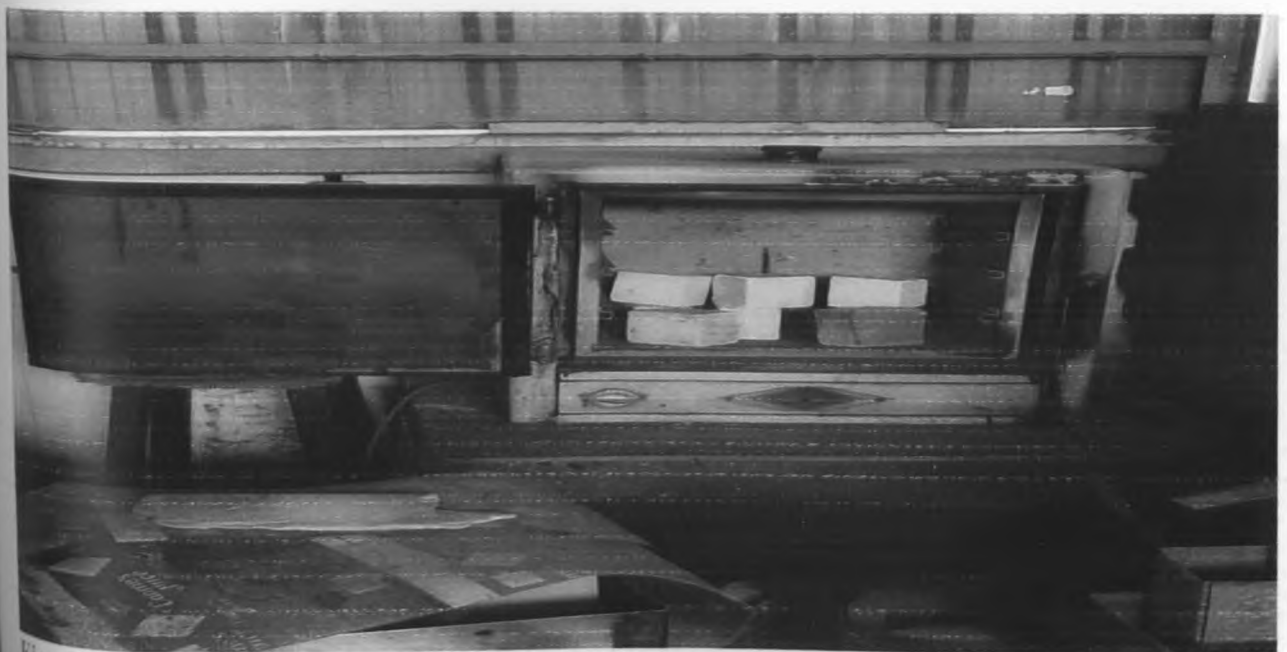
Figure 18: Sample Firebricks in the Firing Furnace

Figure 18 above shows the firing furnace in KIRDI Ceramic Pilot Plant. The firing furnace was fitted with temperature control units and thermocouples.

The bricks were crushed using a jaw crusher to produce grog. The standard sieves 3mm, 1mm and 200 μm were used to classify grog in three different particle sizes i.e. coarse, medium and fines as recorded in Table 7 below. The tailings were recycled for production of fine, coarse or medium particle sizes. The classified grog was transferred into clean containers labelled KFB_C, KFB_M and KFB_F for coarse, medium and fine particle sizes respectively. The procedure was repeated 2 times.

Table 6: Grog Classification

Grade	Screen Sizes
Coarse	<1mm-3mm>
Medium	<1mm-200μm>
Fine	≤200μm
Tailings	≥ 3mm

Figure 19: Classified Grog and Sieves

Figure 19 above shows the sample classified grog and the Tailor series sieves used for grog sieving. The grog was classified into different particle sizes to study the impact of particle size distribution on mechanical properties of sample firebricks.

12.63kg of MBC and 17.37kg of EK were weighed and mixed in the pan mixer for 10 minutes. The mixture was transferred into a bucket and labeled binder. The bucket was tightly closed and kept in a cool and dry place for sample firebrick production. Approximately 100kg of grog and 30kgs of the binder were produced for sample firebrick formulation.

3.5.2. Particle Size and Distribution

Samples A, B, C, D, E, F and G were prepared with different particle size aggregates by weight as indicated in Table 8 below. 25 % of the binder was added into each and mixed for 15 minutes in separate containers. The mixtures were transferred to containers labeled A, B, C, D, E, F and G, and thoroughly mixed with 20 % water. Samples were produced in triplicates. 21 samples, weighing approximately 1kg each were pressed at 50 tons pressure.

Table 7: Particle Sizes and Distribution

Sample No	Samples	Fine: Medium: Coarse
1	A	1: 1: 1
2	B	3: 3: 4
3	C	1: 1: 2
4	D	1: 1: 4
5	E	1: 0: 0
6	F	1: 0: 0
7	G	1: 0: 0

The lengths, L_1, of the unfired firebricks were measured and the firebrick samples were air dried for 24 hours, then at 110 ^{O}C for 12 hours in the oven and cooled for 12 hours to room temperature in the furnace. The lengths of dried samples, L_2, were then measured and % Linear Drying Shrinkage, LDS, determined. The samples were fired at 1200 ^{O}C for 24hrs and cooled to room temperature for 3 days. The compressive strength, bulk density and apparent porosity were determined at room temperature.

3.5.3. Grog to Binder Ratio

The mixing ratio that had minimum apparent porosity obtained in Section 3.5.2 was used to investigate the effect of grog to binder ratio on apparent porosity, bulk density and compressive strength of the sample firebricks. 7.5kg of coarse, 3.75kg of medium and 3.75kg of fine screen sizes were weighed and mixed in the pan mixer for 15 minutes. They were divided into 5 parts weighing 3.00kgs each and transferred to containers labeled S_{AA}, S_{BB}, S_{CC}, S_{DD} and S_{EE}. 0.33kg, 0.75kg, 1.29kg, 2kg and 3kg of the binder was added respectively and thoroughly mixed. 25 % of water by weight was added to each and mixed to homogeneity. The samples were pressed at 50 tons and air-dried for 24 hours. They were then dried at 110 ^{O}C in an oven overnight and fired at 1200 ^{O}C for 24 hours. A total of 15 sample firebricks, each weighing 1kg, were made. The samples were analyzed for compressive strength, bulk density and apparent porosity.

3.5.4. Amount of Water

The percentage binder and particle size distribution with the lowest apparent porosity obtained in Section 3.5.3 and 3.5.2 respectively were used to investigate the effect of water. 7.5kg of coarse, 3.75kg of medium, 3.75kg of fine and 6.43kg of the binder were weighed and thoroughly mixed in the pan mixer. They were divided into 5 parts of 4.29kg each and placed into containers labeled SW_1, SW_2, SW_3, SW_4 and SW_5. 215cm^3, 430cm^3, 645cm^3, 860cm^3 and 1075cm^3 of

water were added respectively and mixed to homogeneity. The samples weighing approximately 1 kg and in triplicates were pressed at 50 tons and air dried for 24 hours. They were then dried at 110 ^{O}C in the oven for 12 hours and fired at 1200 ^{O}C for 24 hours in a furnace. The samples were analyzed for drying shrinkage, compressive strength, bulk density and apparent porosity.

3.5.5. Sample Curing Schedule

7.5kg of coarse, 3.75kg of medium, 3.75kg of fine, 6.43kg of the binder, and 6.4 liters of water were measured and mixed thoroughly in the pan mixer. They were divided into 7 parts of 4 kg each and placed into containers labeled SRT_0, SRT_1, SRT_2, SRT_3, SRT_4, SRT_5 and SRT_6. The firebricks were pressed at 50 tons, dried away from direct sunshine for 24 hours and in the oven at 110 ^{O}C for 12 hours. The bricks were made in triplicate and fired at 1200 ^{O}C. The soaking time of firing was varied as 0, 3, 6, 9, 12, 15 and 18 hours respectively. They were cooled to room temperature and compressive strength, apparent porosity and bulk density determined.

3.5.6. Kwale Ilmenite Oxide Formulation

7.5kg of coarse, 3.75kg of medium, 3.75kg of fine and 6.43kg of the binder were weighed and thoroughly mixed in the pan mixer. They were divided into 5 parts of approximately 5.57kg each and transferred into containers labeled STO_0, STO_1, STO_2, STO_3, and STO_4 and 0.00 kg, 0.06kg, 0.11kg, 0.17kg and 0.22kg, of KITO added respectively. Approximately 1.6liters of water was added into each mix respectively and mixed thoroughly. Approximately 1kg of the mix was weighed, transferred into the mold and pressed at 50 tons with a hold time of 1 minute. They were air dried away from direct sunlight for 24 hours and in the oven at 110 ^{O}C for 12 hours. The length of the firebrick samples was measured and then fired at 1200 ^{O}C for 24 hours after which cooled to room temperature for 3days.The length of the samples was again measured and

recorded. The firebricks were kept in a cool and dry place. The compressive strength, bulk density, apparent porosity and permanent linear shrinkage of the samples were determined.

3.6.Chemical, Mechanical and Physical Characterization of Firebricks

3.6.1. X-Ray Diffraction Spectrophotometric Analysis

XRD analysis using ASTM C 618 Standard Method for Analysis [Ramachandran & Beaudron, 2001]. Sample firebricks were separately crushed and sieved using 2mm and sub-sampled to 10g by conning and quartering for 5 minutes. The 10g crushed firebrick sample was oven dried at 40 ^{O}C and put in a labeled zip-lock polythene bag and transferred to the XRD laboratory. Using a loading device for McCone Mill, forty eight cylindrical agate grinding elements were loaded into the sample cup. The weight of the sample cup with agate elements were tared and 3 g of sample weighed into sample cup. The mass was made up to 12g using ethanol as a grinding fluid, capped and milled with a McCone Mill for 12 minutes. The unique grinding action of the mill rapidly reduced particles size to sub-micrometer level and mixed to homogeneity, approximately10μm, for quantitative and qualitative analytical methods.

The milled sample was washed into a 50cm^3 centrifuge tube with ethanol making sure to collect as much of it as possible. The power switch of the centrifuge was turned on and stop/open button pressed to release the safety latch and allow the cover of the centrifuge to be opened. The tubes were placed in the centrifuge the cover closed and samples centrifuged for 10 minutes at 4000 revolution per minute. The tubes were removed from the centrifuge, caps pried off and the supernatant liquid evaporated in an oven at 100°C to dryness. Hexane was added to the sample in the ratio of 0.5cm^3 hexane to 1g of crushed firebrick sample. Using a vortex mixture, the mixture was mixed to re-suspend the sample in hexane and then dried at between 80 ^{O}C to 105

^{O}C in an oven for 1 hour. Using a spatula, the sample which was stuck to the centrifuge bottle was scrapped and the dried material was brushed from the tube through a 250 μm sieve onto a weighing paper. The purpose of the brushing was to obtain a homogenous powder with many crystallites in random orientations. The sieved powder sample was poured into a glass vial and capped. The sample was loaded into the XRD sample chamber and analyzed. The analyses were done in triplicates.

3.6.2. PH of Sample Firebricks

The pH of the firebricks was determined using pH meter [Arnold et al, 1992]. The firebrick was crushed into fine powder and 2 g measured. It was then leached with 100 cm^3 of de-ionized water for 12 hours. The supernatant was filtered and the pH determined at ambient temperature. The procedure was repeated three times for each sample firebrick.

3.6.3. Apparent Porosity, Bulk Density and Water Absorption

The Boiling Water Method [Ramachandran & Beaudron, 2001] was used to determine bulk density, apparent porosity and water absorption of the sample firebricks. The sample firebricks were dried at 110 ^{O}C for 12 hours in the furnace, and then left to cool to room temperature for 12 hours. They were then weighed and fully immersed in water, boiled for 2 hours and left to cool for 3 hours. They were removed, dripped for 2minutes, carefully wiped with cotton and the soaked weight taken. The water can was filled with water. The brick was suspended in water using a spring balance and the suspended weight measured. The procedure was repeated 3 times. The results were recorded and the bulk density and apparent porosity calculated as follows,

$$\text{Bulk density} = \frac{\text{Dry weight}}{\text{(Soaked Weight−Suspended Weight)}} \qquad 2.38$$

$$\% \text{ Apparent Porosity} = \left\{\frac{\text{soaked weight} - \text{dry weight}}{\text{Soaked Weight} - \text{Suspended Weight}}\right\} 100 \qquad 2.39$$

The results obtained were as shown in Tables 20, 21, 22, 23 and 24 of Appendix 2.

3.6.4. Compressive Strength at Ambient Temperatures

The dimensions of the sample firebrick i.e. length, width and height, were taken using the Vernier calipers. The surface area of the brick was calculated and recorded. The weight of the firebrick sample was measured. The sample firebrick was placed in the compression chamber and compressive strength machine switched. The maximum load of sample firebrick failure was recorded and compressive strength calculated as follows [Ramachandran & Beaudon, 2001],

$$\text{compressive strenght} = \frac{\text{Maximum Load (N)}}{\text{Surface Area (mm}^2)} \qquad 2.37$$

Figure 20: Compressive Strength Testing at Ambient Temperature

Figure 20 above shows the compressive strength testing of the sample firebricks in progress at the Ministry of Works at the Materials Testing Department.

Chapter 4

RESULTS AND DISCUSSION

4.1.1. Atomic Absorption Spectrophotometric Analysis

The AAS analysis results of EK, EF, MBC and KITO were as shown in Table 9 below. EK, EF and MBC were Al_2O_3-SiO_2 raw materials while KITO was a TiO_2 ore [Kshama et al, 1992].

Table 8: Raw Materials Inorganic Oxides

	EK	EF	MBC	KITO
% SiO_2	72.64	66.64	55.38	0.79
% Al_2O_3	24.74	26.63	36.85	0.38
% Fe_2O_3	0.71	2.78	3.86	53.20
% K_2O	0.05	0.19	1.14	0.004
% Na_2O	0.13	0.17	0.43	0.11
% TiO_2	0.73	2.25	2.96	44.60
Al_2O_3/SiO_2 ratio	0.3406	0.3996	0.6654	0.4810

Using the Rational Analysis Method, see the workings in tables 25-36 in appendix 2, the mineralogical composition of EK, EF, MBC and KITO as ascertained from the AAS analysis were as shown in table 10 below. The mineral composition of the raw materials affects the mechanical, physical and chemical properties of firebricks. The Al_2O_3 content of EK, MBC and EF were above a minimum standard of 23% [Harbison, 2005], therefore favorable for formulating the refractory firebricks. Controlling the % Fe_2O_3 is key in production quality control of the final sample firebricks. The Fe_2O_3 content of MBC, EF and KITO exceeded the

standard maximum limit of 2.5 % [Chukwudu, 2008] while that of EK was optimal for firebrick formulation. Al_2O_3-SiO_2 firebricks are sensitive to corrosion by iron oxides because of formation of low melting compounds; Iron oxide is more corrosive as the content of alumina in the firebrick is lower, and Al_2O_3 firebricks have different degrees of resistance to corrosion by iron oxides depending on the oxygen potential [Karl & Mark, 2002].

Table 9: Mineral Composition in the Raw Materials by Rationale Analysis Method

Mineral	EK	EF	MBC	KITO
Orthoclase %	0.28	1.00	5.74	0.22
Albite %	1.00	1.26	3.14	0.94
Anorthite %	0.50	1.28	0.11	-
Kaolinite %	56.58	58.47	72.52	-
Quartz %	39.51	30.78	7.48	-
Ilmenite %	-	-	4.89	79.77
Rutile %	-	-	0.89	18.03
Limonite %	-	2.72	-	-
Hematite %	0.41	-	-	-
Limestone %	-	-	-	0.14
Corundum %	-	-	-	0.15

The Rational Analysis Method revealed that the % kaolinite, $Al_2O_3.2SiO_2.2H_2O$, content of EK, EF and MBC samples was 56.58, 58.47 and 72.52 while the % quartz, SiO_2 was 39.51, 30.74 and 7.44 respectively as shown in table 10 above. The fluxing minerals which were established in trace amounts were albite, anorthite and orthoclase.

81

4.1.2. Particle Size and Distribution

The particle size and distribution results obtained were as shown in Table 11 below. See the workings in Table 20 in Appendix 2. Graphs of apparent porosity, compressive strength and bulk density against particle size and distribution are as shown in Figure 21, 22 and 23 below. The X-axis numbers 1 to 7 represent samples S_1 to S_7 with different particle size distribution as indicated in Table 11. In Figure 21 the apparent porosity reduced from 44.71 % in S_1 to a minimum of 36.23 % in S_3.

Table 10: Effects of Particle Size and Distribution

	Units	S_1	S_2	S_3	S_4	S_5	S_6	S_7
Coarse	%	26.67	32	40	53.33	100	0	0
Medium	%	26.67	24	20	13.33	0	100	0
Fine	%	46.66	44	40	33.33	0	0	100
Apparent Porosity	%	44.71	39.02	36.23	37.71	43.22	42.24	47.01
Compressive Strength	kN/ cm^2	1.47	1.71	2.07	1.79	1.41	1.52	1.14
Bulk Density	g/cm^3	1.51	1.56	1.62	1.58	1.53	1.53	1.50
Linear Drying Shrinkage	%	4.99	3.76	2.91	3.61	2.81	3.27	5.63

The apparent porosity then increased with increasing coarse aggregate from 36.23% to a maximum of 47.01 % in S_7. The optimal apparent porosity i.e. 36.23 % was obtained in Sample S_3, with ratio of 2:1:2. At this particle size and distribution the ratio of coarse, fines and mediums was optimum to minimize porosity during compaction. The apparent porosity varied with

characteristic particle size distribution of samples. The apparent porosity variation with particle size distribution was in agreement with the findings of Rice, [1996] who established that the particle size distribution affects the mechanical and physical properties of the firebricks.

In Figures 22 and 23 below, the maximum compressive strength, $2.07kN/cm^2$, and bulk density, $1.62g/cm^3$, were obtained with S_3, while the minimum compressive strength, $1.14kN/cm^2$, and bulk density, $1.50g/cm^3$, were obtained with S_7 that gave maximum apparent porosity, 47.01 %.
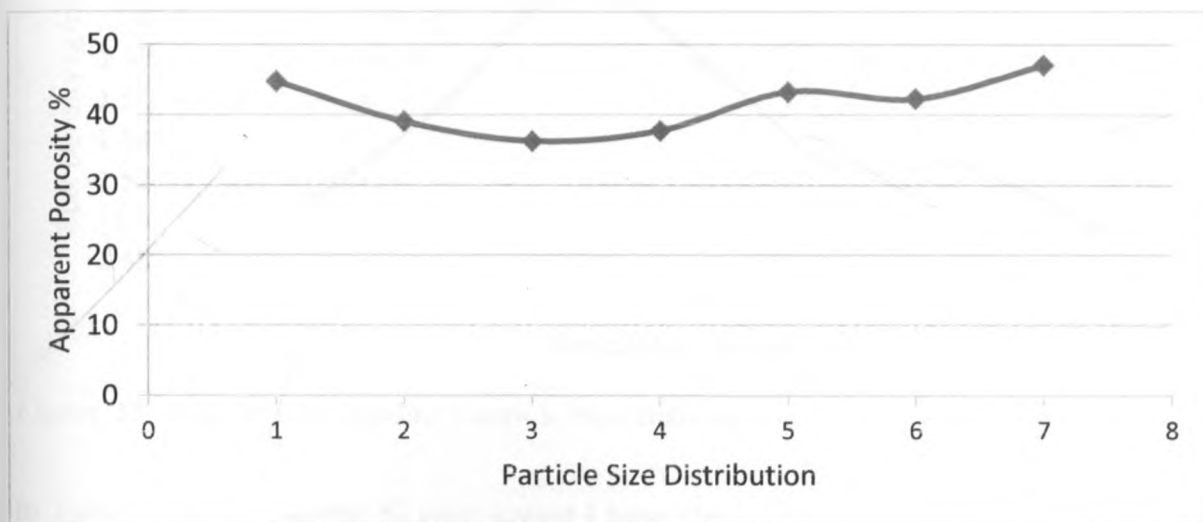
Figure 21: Apparent Porosity against Particle Size Distribution
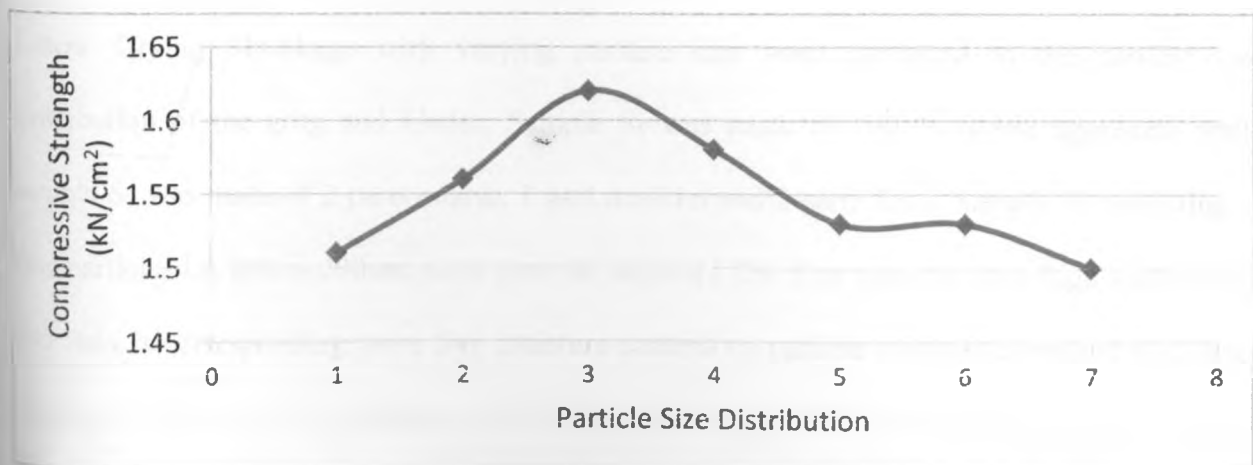
Figure 22: Compressive Strength against Particle Size Distribution

The particle size and distribution of raw materials have a significant impact on the packing density, size and shape of pore interstices as well as the deformation and the firing behavior of ceramic bodies. From the experiments, three particle systems, S_2, S_3 and S_4 gave optimal compaction, which yielded optimal apparent porosity, bulk densities and compressive strength than mono-sized particle systems, i.e. S_7 and S_5.
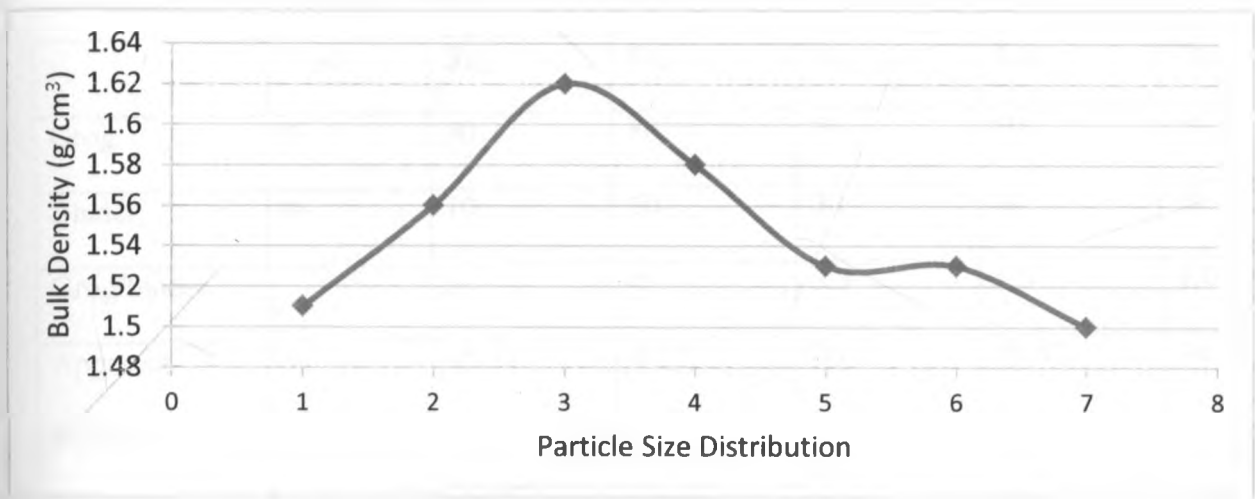
Figure 23: Bulk Density against Particle Size Distribution

In Table 11 above, Sample S_5 gave lowest Linear Drying Shrinkage, LDS, of 2.81 % while S_7 yielded the highest LDS of 5.63 %. Sample S_3 had the second lowest LDS. The variations in Linear Drying Shrinkage with varying particle size were attributed to the particle size distribution of the grog and binder. Sample S_5 was made of 100 % coarse aggregate while sample S_3 was made of 2 parts coarse, 1 part medium and 2 parts fines. Sample S_7 consisting of fine particles i.e. below 200µm sieve gave the highest LDS. Fine particles have high surface area and thus, a corresponding more free moisture content on particle surfaces compared to coarser particles. Since drying shrinkage results from the removal of water films from the particle surfaces and not from the voids between particles, bodies with higher percentage of fine particles i.e. Sample S_7, content had consequently higher drying shrinkages compared to bodies with less

percentage of fine particles i.e. Samples S_3 and S_5. Linear drying shrinkage should be as minimal as possible to minimize firebrick warping and spalling especially during firing as a result high LDS is undesirable [Kamran & Allaire, 2000].

4.1.3. Grog to Binder Ratio

The results of the grog to binder ratio are as shown in Table 12 below.

Table 11: Grog to Binder Ratio

	Units	S_{AA}	S_{BB}	S_{CC}	S_{DD}	S_{EE}
Grog	%	90	80	70	60	50
Binder	%	10	20	30	40	50
Grog/binder		9	4	2.3	1.5	1.0
Apparent porosity	%	45.11	40.77	36.82	39.97	44.01
Compressive strength	kN/cm^3	1.06	1.78	1.99	1.96	1.90
Bulk density	g/cm^3	1.45	1.50	1.59	1.57	1.55

The variations of apparent porosity, bulk density and compressive strength with grog to binder ratio are as shown in Figures 24, 25 and 26 respectively. The maximum compressive strength, 1.99kN/cm^2, bulk density, 1.59g/cm^3, and lowest apparent porosity, 36.82 % were obtained with sample S_{CC}, consisting of 70 wt % grog and 30 wt % binder respectively. The lowest compressive strength, 1.06kN/cm^2, bulk density 1.45 g/cm^3 and the highest apparent porosity, 45.11 %, were obtained with sample S_{AA} consisting 90 wt % grog and 10 wt % binder. S_{AA} and S_{BB} exhibited poor green strength, high water absorption and drying rate. This was attributed to

higher grog percentage. S_{DD} and S_{EE} took longer time to dry and exhibited pronounced drying and firing shrinkages than other samples due to higher amount of the binder.
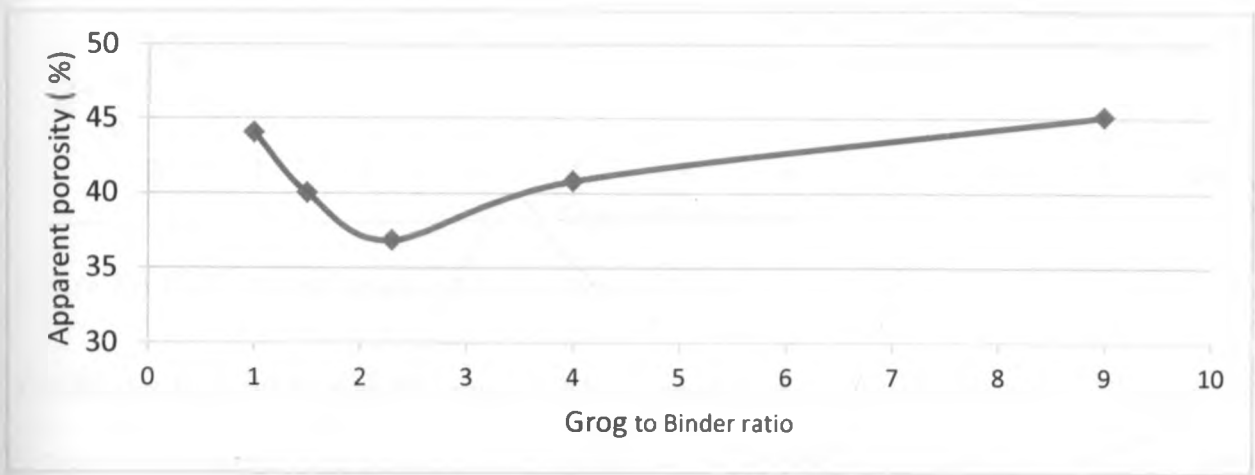
Figure 24: Porosity versus Grog to Binder Ratio

The binder phase composed of EK and MBC which were made of fine particles, below sieve 200µm. The drying shrinkage was attributed to increased water absorption caused by increased surface area of binder clay fine particles. The use of grog drastically reduced water absorption and phase transformation which are the main causes of drying and firing shrinkage. In Figure 24, when the percentage binder dropped or exceeded 30 % the apparent porosity increased resulting in lower compressive strength and bulk density. These findings were in agreement with the findings of Rahman, 2012 who found out that grog to binder ratio influenced the final mechanical and physical properties.
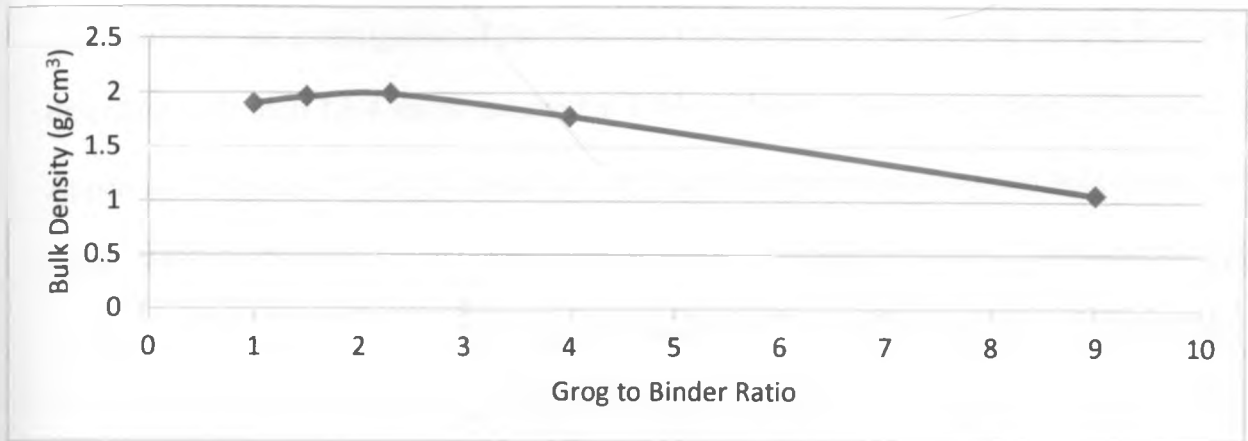
Figure 25: Bulk Density against Grog to Binder Ratio

The Binder level 30 % was the point at which apparent porosity was lowest on Figure 24 or compressive strength and bulk densities highest see Table 12, Sample Scc. At Binder levels below 30 % the clay phase was no longer able to fill the voids between the Grog particles causing a drop in bulk density and compressive strength. At higher binder levels beyond 30 %, water absorption increased and the phase transformation reactions in the binder phase were more pronounced adversely affecting the compressive strength and bulk density [Matsui *et al*, 1991]
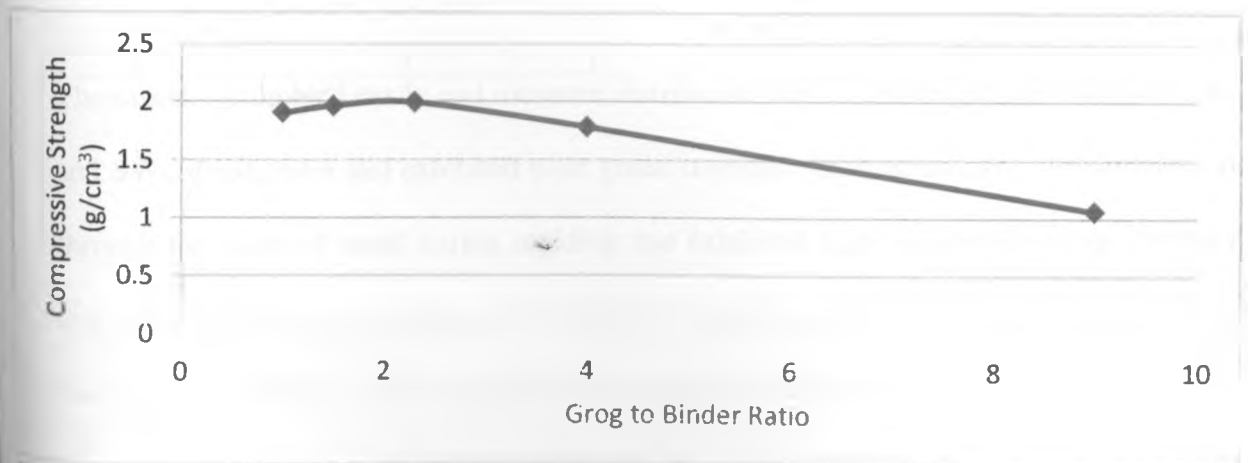
Figure 26: Compressive Strength against Grog to Binder Ratio

4.1.4. Amount of Water

The results for the investigation of the effects of the amount of water on the sample firebricks as described in Section 3.5.4 are as recorded in Table 13 below. See the workings in Table 22 in Appendix 2. Figures 27 and 28 shows the variations of apparent porosity and bulk density with water content at constant firing temperature of 1200 ^{O}C. In Figure 27, 16.71 % water, the optimal amount of water, gave the minimum apparent porosity, 36.97 %, and maximum bulk density, 1.58 g /cm^3 as shown by the minima point on Figure 28. In Figures 27 and 28, the points indicate the apparent porosities and bulk densities of samples SW_1, SW_2, SW_3, SW_4 and SW_5 from left to right.

Table 12: Amount of Water in Sample Firebricks

	Units	SW_1	SW_2	SW_3	SW_4	SW_5
Water	%	4.78	9.12	13.08	16.71	20.05
Apparent porosity	%	49.23	40.53	38.91	36.97	41.12
Bulk density	g/cm^3	1.27	1.49	1.53	1.58	1.50

The samples crumbled easily and moisture distribution was not homogenous. Samples SW_1, SW_2 and SW_3, dried faster and exhibited poor green strength. In samples SW_5, the samples extruded through the joints of mold during molding and exhibited high volume shrinkage during drying and firing. The finer the particles, the stronger the inter-particle attraction/adhesive forces due to the high ion-exchange capacity between the particle-water-particle contacts. Samples SW_1, SW_2 and SW_3, had a poor inter-particle attraction due to low amount of water. The high amount of water in sample SW_5 increased drying and firing shrinkage. These results were in agreement

with the findings of Rahman 2012, who found out that the amount of water influences drying and firing shrinkages.
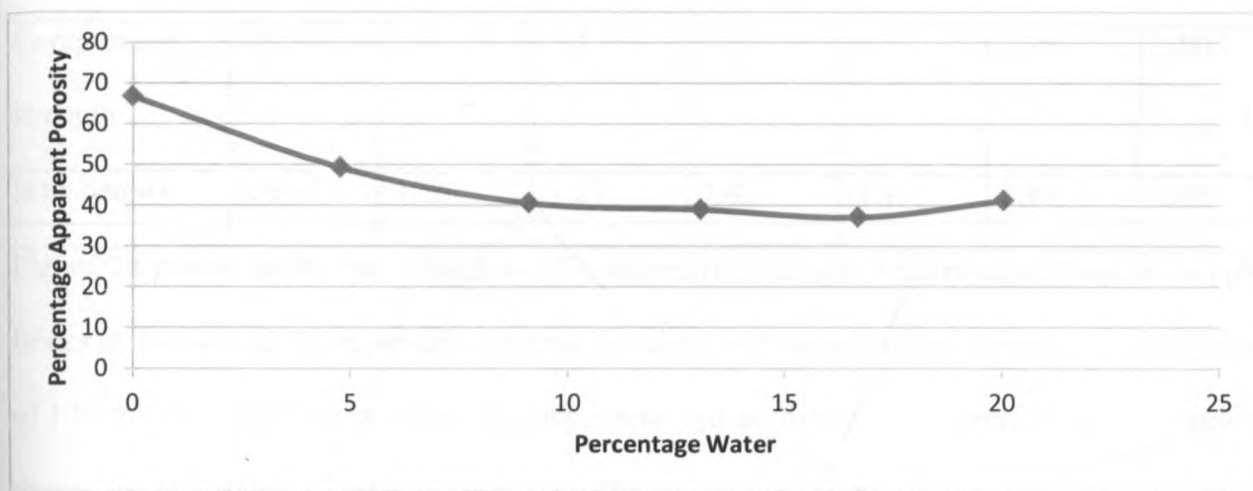
Figure 27: Apparent Porosity against Water
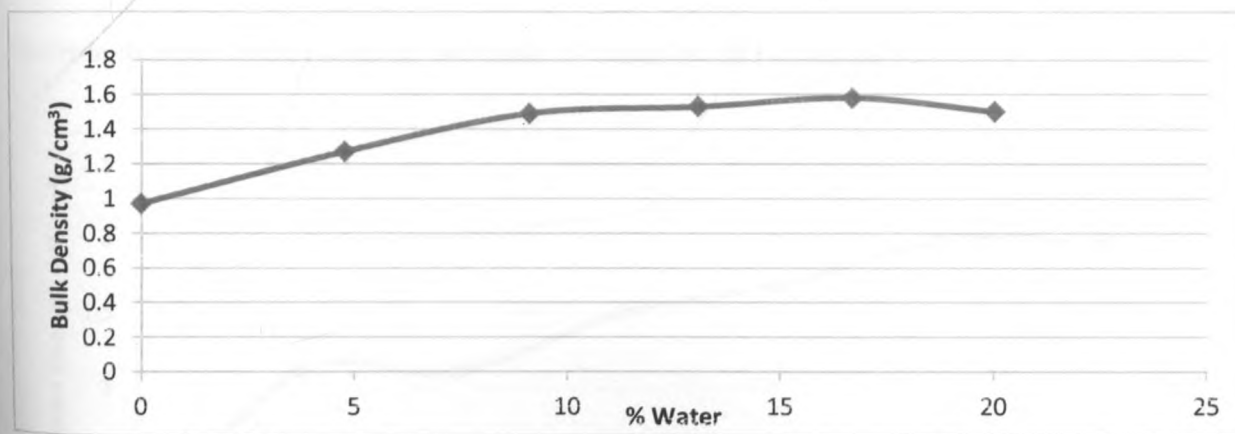
Figure 28: Bulk Density versus Amount of Water

4.1.5. Curing Schedule

The results obtained from the experiments in Section 3.5.5 are as presented in Table 14 below. See the workings in Table 23 of Appendix 2. In this experiment, a constant firing temperature of 1200 ^{O}C, heating rate of 50 ^{O}C/hour and approximate cooling rate of -16 ^{O}C/ hour were applied

Table 13: Curing Schedule on Firebricks

	Units	SRT_0	SRT_1	SRT_2	SRT_3	SRT_4	SRT_5
Firing time	Hours	3	6	9	12	15	18
Compressive strength	kN/cm^2	1.1	1.1	1.5	1.7	1.99	2.00
Bulk density	g/cm^3	1.26	1.27	1.42	1.47	1.49	1.49

Figure 29 below shows the variations of compressive strength with resident time of sample bricks in the furnace. Compressive strength increased with sample curing time up to a maximum of 1.99 kN/cm^2 which upon further heating, there was no further increments. Figure 30 below shows the variations of bulk density with the firing time in the furnace. The bulk density increased with the firing time to a saturation point, 1.49g/cm^3 where there were no further increments upon further heating, see table 14 Samples SRT4 and SRT5.
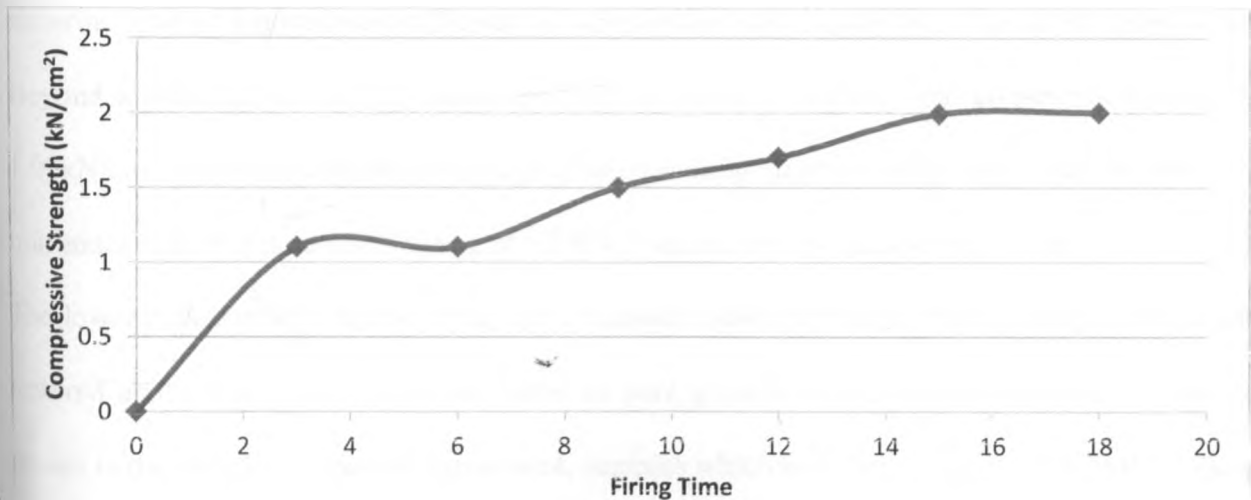
Figure 29: Compressive Strength against Resident Time
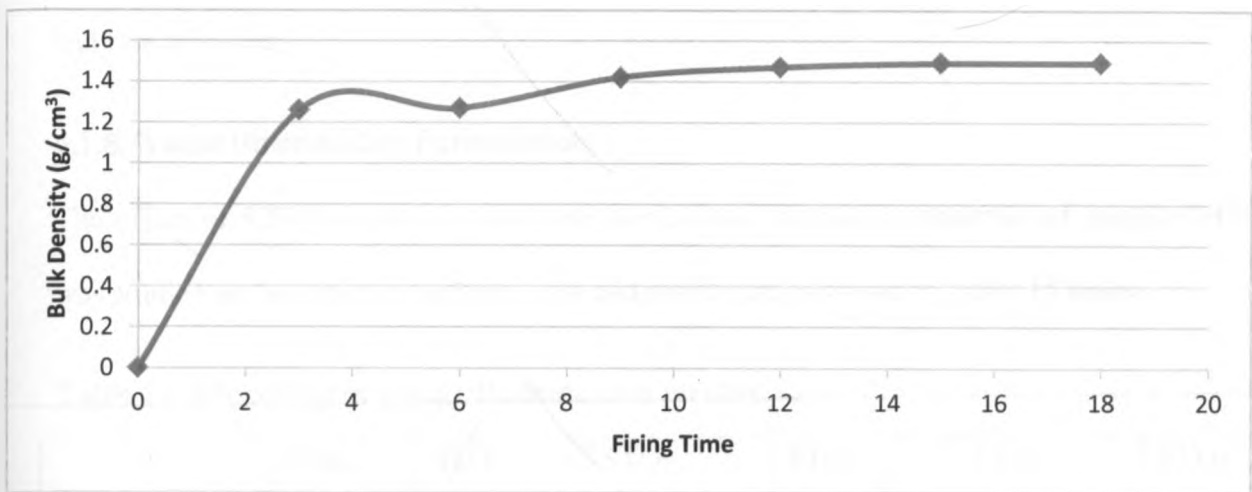
Figure 30: Bulk Density against Resident Time

The samples sintered below 6 hours at 1200 ^{O}C had a lower average bulk densities compared to the green state bulk densities. The decrease in bulk densities was attributed to pore growth in the early stages of sintering whereby gases in the inter-granular spaces and from decomposing organic matter first expand prior to their escape from the matrix. Samples sintered at 1200 ^{O}C, a sintering time of 9 hours was sufficient to increase the bulk density over that of the green state. Beyond a sintering time of 12 hours, the bulk densities, 1.49g/cm^3, and compressive strength, 1.99kN/cm^2 remained constant with increasing sintering time showing that in this firebrick, a minimum sintering time of 12 hours, at 1200°C, was enough to achieve maximum densification. The lower bulk densities below 1.42g/cm^3 of samples sintered below 9 hours compared to those sintered above 9 hours could be attributed to pore growth resulting from trapping of evolved gasses in the sample. In another experiment, samples which were heated at a rate of 200 ^{O}C /hour and cooled at -61 ^{O}C/ hour developed macro-cracks and exhibited higher spalling rate. The samples that were cooled in the air with approximate cooling rate of -117 ^{O}C /hour exhibited low compressive strength, 0.7kN/cm^2, and bulk density, 0.97g/cm^3. Thus the firing and cooling rate influence the mechanical properties of the firebricks. These findings were in comparison with the

findings of Ibisi in 1991 who established that degree of sintering is influenced by soaking time and rate of curing.

4.1.6. Kwale Ilmenite Ore Formulation

The effect of KITO on the physical, mechanical and chemical properties of sample firebricks was studied as described in Section 3.5.6 and results are as shown in Table 15 below.

Table 14: Properties of Kwale Ilmenite Ore Firebricks

	Units	STO_0	STO_1	STO_2	STO_3	STO_4
KITO	%	0	1	2	3	3.43
Apparent Porosity	%	36.78	37.01	36.58	36.87	36.45
Bulk density	g/cm^3	1.60	1.59	1.60	1.57	1.59
Compressive strength	kN/cm^2	2.03	2.01	1.98	2.00	2.06
Color		Brown	Yellow	Yellow	Yellow	Yellow

Figure 31, 32 and 33 below shows the variation of apparent porosity, compressive strength and bulk density at different percentage of KITO in the Sample firebricks. In figure 31, apparent porosity did not vary significantly with the varying amounts of KITO in the sample firebrick. The compressive strength and bulk densities increased significantly to $2.06kN/cm^2$ and $1.61g/cm^3$ in sample STO_4 containing 4% KITO as shown in figures 32 and 33 respectively. This was attributed to the presence of KITO and these results were found in agreement with Arato et al, [1995] found out that the low melting phases enhance initial stage of sintering consequently improving bulk densities and compressive strength.
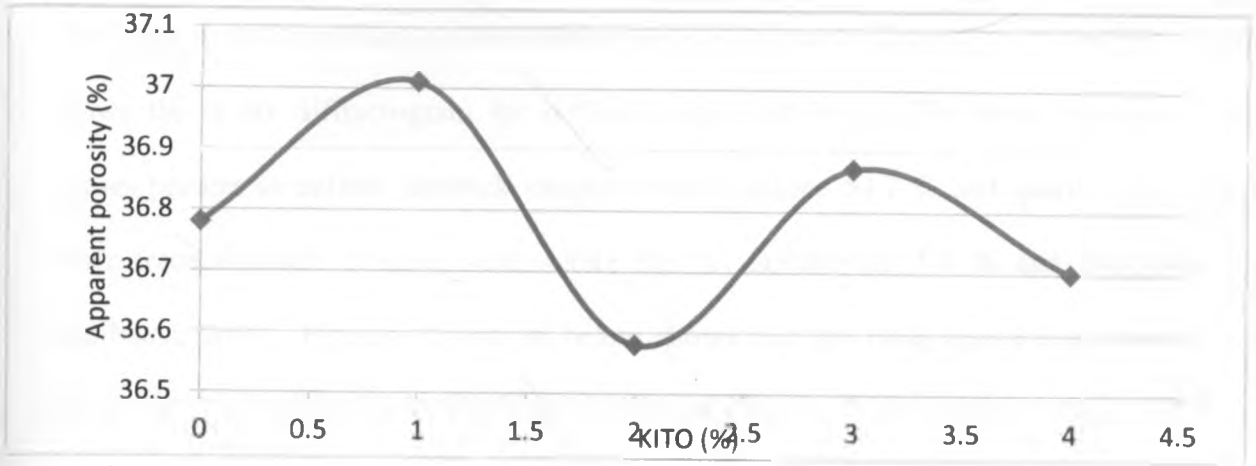
Figure 31: Apparent Porosity versus % KITO
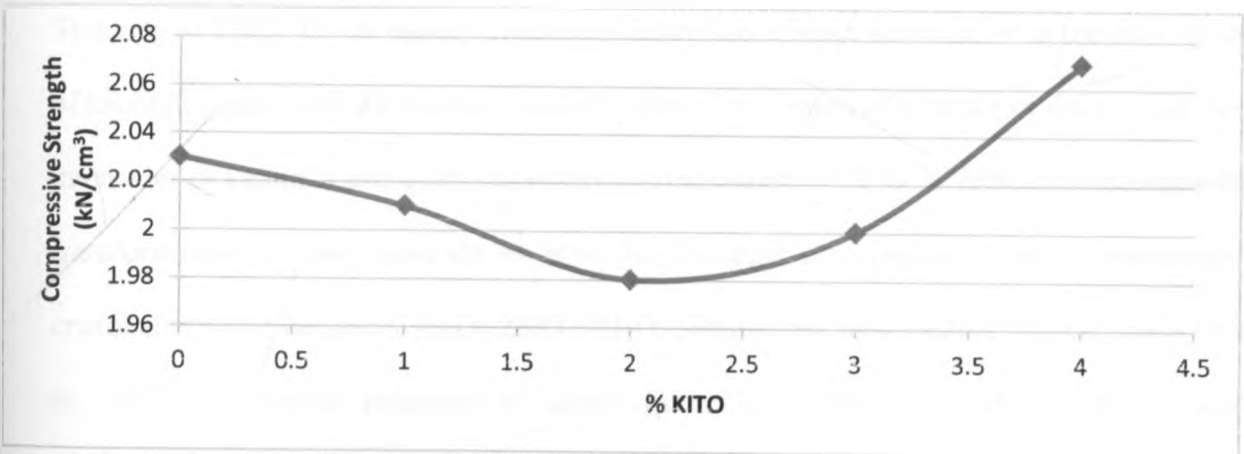
Figure 32: Compressive Strength versus % KITO
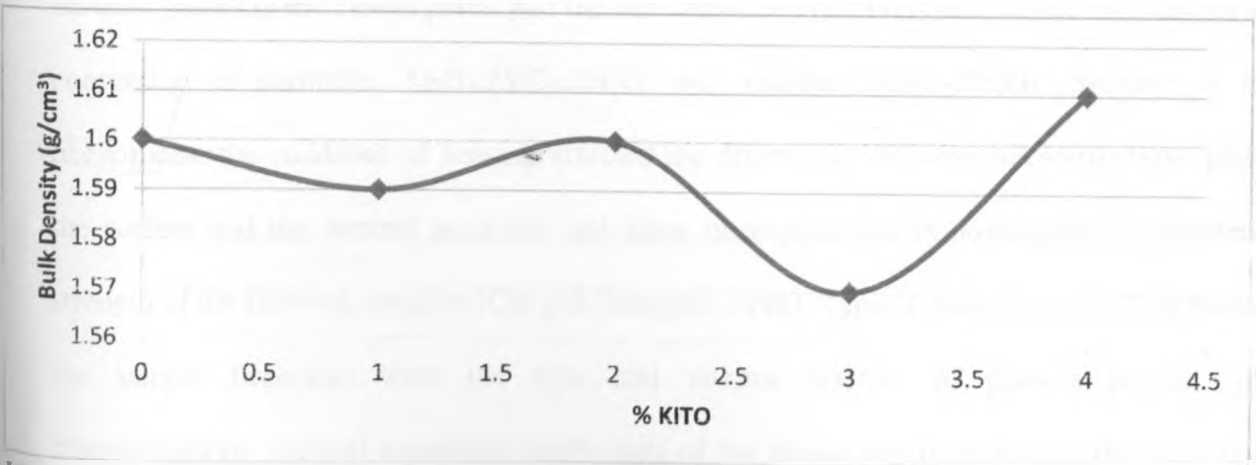
Figure 33: Bulk Density versus % KITO

4.1.7. X-Ray Diffraction Analysis of Sample Firebricks

The XRD analysis diffractograms obtained were as shown in figures 34, 35 and 36. Figure 34 shows the X-ray diffractogram for unfired sample firebricks. The main constituent mineral phases present in unfired firebrick samples were kaolinite 54.7 % and quartz 29.4 % and the other trace minerals present were Albite 9.6 %, hornblende 4.0 % and magnetite 2.2 % [Harbison, 2002]. Figures 35 and 36 below shows that the main constituent minerals phases present in fired sample firebricks were mullite 44.0 %, cristobalite 18.5 %, quartz 25.9 % and corundum 11.6 % [Chakraborty & Ghosh, 1977].

Sintering at 1200 ^{O}C was mainly characterized by the absence or decrease in the peak intensities of kaolinite, quartz, albite and presence of mullite. The observed absence or decrease in the peak intensities of kaolinite and quartz at sintering temperature of 1200 ^{O}C indicated decomposition or transformation of clay minerals to other high temperature phases. Quartz transformed into cristobalite while kaolinite, $Al_2O_3.2SiO_2.2H_2O$, transformed into mullite, $3Al_2O_3.2SiO_2$ [Arato et al, 1995]. The thermal processes of sample firebrick at temperatures above 1000 ^{O}C were the result of a combination of sintering, shrinkage and expansion by the effect of temperature on the residual gasses in the closed pores, and the decomposition reactions such as the high temperature conversion of kaolinite, $Al_2O_3.2SiO_2.2H_2O$, into mullite, $3Al_2O_3.2SiO_2$. Because of these phenomena, the condition of heating affected the differences between microstructures close to the surface and the internal positions and these microstructural in-homogeneities affected the strength of the firebrick samples [Carty & Senapati, 1998]. Typical strength controlling factors in the sample firebricks were the type and volume fraction of phase's present, phase transformations, thermal expansion coefficients of the phases and to an extent, the grain size of

the crystalline phases [Bogahawatta & Poole, 1991]. All of these factors were present in firebrick samples and were dependent on the extent of firing process.

Both compressive strength and bulk densities increases with mullite content and is attributed to the interlocking effect of secondary mullite. The interlocking of secondary mullite crystals inhibits the propagation of cracks and thereby improving the strength of firebricks. Notably, secondary mullite due to its acicular morphology and smaller needle diameter has more interlocking effect compared to primary mullite. The quartz polymorphism serves as a source of flaws in the firebricks [Bergeron & Risbud, 1984].

Figure 34: Unfired Firebrick Diffractogram

The following details appear within the diffractogram figure:

Y-axis: Lin (Counts), scale from 0 to 3900
X-axis: 2-Theta - Scale, range from 4 to 70

Commander Sample ID - File: icr078910.raw - Type: Locked Coupled - Start: 3.060 ° - End: 75.055 ° - Step: 0.020 ° - Step time: 96 s - 2-Theta: 3.060 ° - Generator kV: 30 kV - Generator mA: 10 mA - Divergence slit:

Operations: Displacement -0.073 | Background 0.000,1.000 | Import

00-046-1045 (*) - Quartz, syn - SiO2 - I/Ic PDF 3.4 - S-Q 29.4 % - F30=558(0.0011,31)

01-080-1094 (A) - Albite, low - Na(AlSi3O8) - I/Ic PDF 0.6 - S-Q 9.6 % - F30=169(0.0040,37)

01-075-1593 (D) - Kaolinite 1A - Al2Si2O5(OH)4 - I/Ic PDF 1.2 - S-Q 54.7 % - F30=1000(0.0007,33)

01-071-1060 (N) - Hornblende - Na.9K.4Ca1.6Mg2.8Fe1.4Ti.5Al2.4Si6O23(OH) - I/Ic PDF 0.6 - S-Q 4.0 % - F30=322(0.0029,42)

00-019-0629 (*) - Magnetite, syn - Fe+2Fe2+3O4 - I/Ic PDF 4.9 - S-Q 2.2 % - F26= 59(0.0126,34)

Figure 35: Sample A Fired Firebrick Diffractogram

The figure contains the following axis labels and annotations:

- Y-axis: Lin (Counts), with gridlines at 0, 100, 200, 300, 400, 500, 600, 700, 800, 900, 1000, 1100, 1200, 1300, 1400, 1500, 1600, 1700, 1800, 1900, 2000, 2100, 2200, 2300, 2400, 2500, 2600, 2700, 2800, 2900, 3000, 3100, 3200, 3300, 3400, 3500, 3600, 3700, 3800, 3900
- X-axis: 2-Theta - Scale, with gridlines at 4, 10, 20, 30, 40, 50, 60, 70

Commander Sample ID - File: icr078911.raw - Type: Locked Coupled - Start: 3.060 ° - End: 75.055 ° - Step: 0.020 ° - Step time: 96. s - 2-Theta: 3.060 ° - Generator kV: 30 kV - Generator mA: 10 mA - Divergence slit:

Operations: Displacement -0.073 | Background 0.000,1.000 | Import

00-046-1045 (*) - Quartz, syn - SiO2 - I/Ic PDF 3.4 - S-Q 25.9 % - F30=558(0.0011,31)

01-074-9378 (*) - Cristobalite - SiO2 - I/Ic PDF 5.9 - S-Q 18.5 % - F30=1000(0.0003,30)

01-089-2814 (D) - Mullite, syn - Al(Al.83Si1.08O4.85) - I/Ic PDF 0.8 - S-Q 44.0 % - F30=1000(0.0001,32)

00-046-1212 (*) - Corundum, syn - Al2O3 - I/Ic PDF 1. - S-Q 11.6 % - F25=379(0.0021,25)

Commander Sample ID - File: icr078911.raw - Type: Locked Coupled - Start: 3.060 ° - End: 75.055 ° - Step: 0.020 ° - Step time: 96. s - 2-Theta: 3.060 ° - Generator kV: 30 kV - Generator mA: 10 mA - Divergence slit:
Operations: Displacement -0.073 | Background 0.000,1.000 | Import

00-046-1045 (*) - Quartz, syn - SiO2 - I/Ic PDF 3.4 - S-Q 25.9 % - F30=558(0.0011,31)
01-074-9378 (*) - Cristobalite - SiO2 - I/Ic PDF 5.9 - S-Q 18.5 % - F30=1000(0.0003,30)
01-089-2814 (D) - Mullite, syn - Al(Al.83Si1.08O4.85) - I/Ic PDF 0.8 - S-Q 44.0 % - F30=1000(0.0001,32)
00-046-1212 (*) - Corundum, syn - Al2O3 - I/Ic PDF 1. - S-Q 11.6 % - F25=379(0.0021,25)

Figure 36: Sample B Fired Refractory Firebrick

4.1.8. Elemental Analysis of Sample Firebricks

Figure 37 below shows the fired sample refractory firebricks in the Ceramic Pilot Plant Laboratory in KIRDI ready for chemical, mechanical and physical characterization. The firebricks were kept in a cool and dry place.
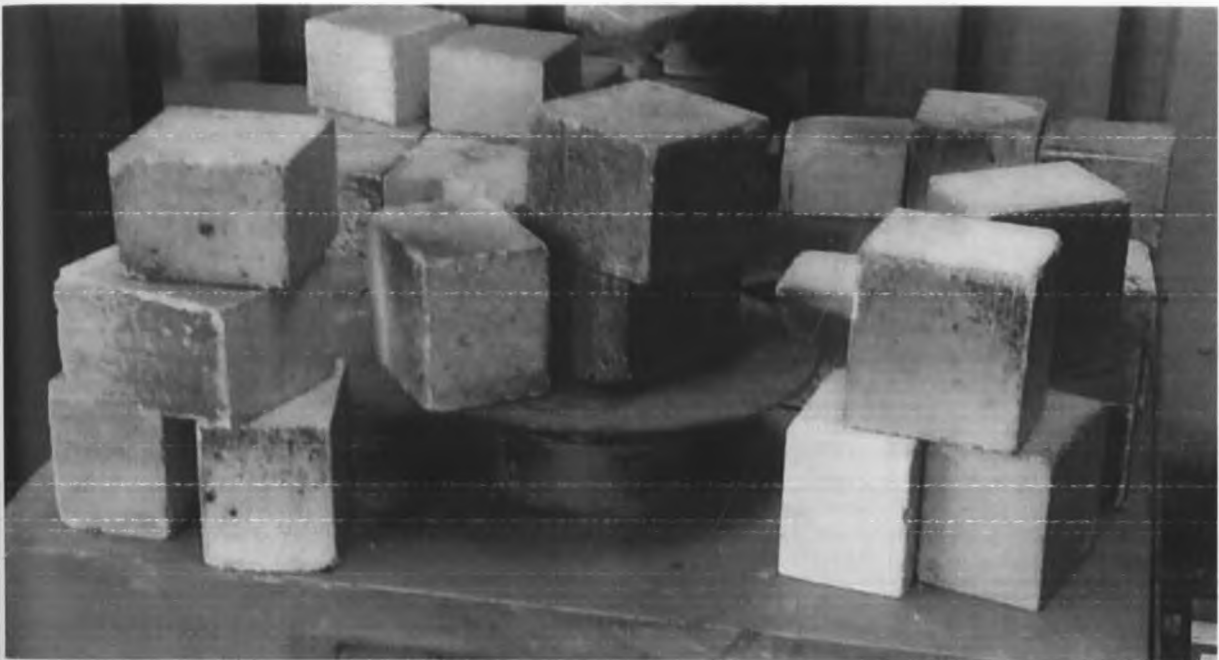
Figure 37: Sample KITO formulated Firebricks

The elemental analysis of KITO formulated sample firebricks was determined using Atomic Absorption Spectrophotometer and results are as shown in the Table 16 below. The average elemental oxide composition of the KITO formulated firebricks indicated that the firebricks were medium duty range i.e. 26-33 % Al_2O_3. The Fe_2O_3, TiO_2 and other trace elements content were within the standard limits of the refractory firebrick. This was in agreement with [Harbison, 2005]

Table 15: Elemental Composition of Firebricks

Elemental Oxide	Standard	Imported	KITO Formulated Sample Firebricks STO$_3$
%SiO$_2$	60-70	57.69	65.87
%Al$_2$O$_3$	26-36	33.80	27.53
%Fe$_2$O$_3$	$\leq$2.5	1.94	2.08
%K$_2$O	$\leq$3	1.20	0.12
%Na$_2$O	$\leq$3	0.23	0.07
%TiO$_2$	$\leq$4	2.26	3.43
%CaO	$\leq$1.0	0.55	0.11
%MgO		0.31	0.18
%MnO		0.02	0.12
Al$_2$O$_3$/SiO$_2$ ratio	$\leq$0.60-0.37$\geq$	0.59	0.42

4.1.9. pH Analysis of the Sample Firebricks

The pH analysis of the sample firebricks result are as shown in Table 17 below.

Table 16: pH of Firebricks

	Standard	Imported	Sample
pH	7	6.65±0.35	6.78±0.22

The pH of the sample KITO formulated firebricks was optimum [ASTM]. The sample firebricks can be utilized in acidic and basic environments without substantial chemical degradation. Most industrial processes are acidic or basic in nature. To overcome the reactor lining corrosion,

neutral firebricks i.e. neither reacts with base nor acid are vital. The higher the pH of the firebricks, the higher the corrosion of the firebricks.

4.2.0. Physical and Mechanical Properties

Table 18 below shows the mechanical properties of sample firebricks as analyzed in Section 3.6.1 and 3.6.2. The average apparent porosity, 36.45 %, and bulk densities, $1.64g/cm^3$, of the sample firebricks as shown in Table 18 below were below the standard of 25% and $1.71g/cm^3$ respectively, while the compressive strength at room temperature, $20.6N/mm^2$ and Linear Firing Shrinkage, 8.74%, were within the minimum standard limits.

Table 17: Mechanical Properties of Sample Firebricks

	Units	Firebricks		
		Standard Firebrick	Imported Firebrick	Sample Firebrick
Apparent porosity	%	15-25	17.23	36.45
Bulk density	g/cm^3	1.71-2.2	2.00	1.64
Compressive strength	N/mm^2	20	42. 7	20.6
Linear Firing Shrinkage	%	0-10	0.00	8.7375
Dimensions			25cm by 15cm by 12.5cm	9cm by 10cm by 8.75cm
Weight	kgs	4.0-5.0	4.11	0.91
Cost per unit (locally)	Kshs		450	120

The high apparent porosity and low bulk densities were attributed to the firing temperature of up to a maximum of 1200 ^{O}C. Liquid phase sintering was the primary densification mechanism for sample firebricks and at 1200 ^{O}C. At 1200 ^{O}C, the liquid in the narrow channels between the particles which results in capillary pressure that aids densification by several mechanisms, rearranging the particles to achieve better packing and increasing the contact pressure between particles was not optimal to build substantial capillary pressure. This reduced the rate of material transfer by solution/ precipitation, creep and plastic deformation, vapor transport, and grain growth, thus reducing apparent porosity and bulk densities. The shrinkage of firebricks was as a result of dehydroxylation of the lattice water in the kaolinite mineral structure and the oxidation of organic matter present in the binder phase. The crystal structure of kaolinite contains water of crystallization whose dehydration to form metakaolin, $Al_2O_3.2SiO_2$, occurs via the reaction,

$$Al_2O_3.2SiO_2.2H_2O \xrightarrow{\hspace{0.5cm} 400\text{-}550\ ^{O}C \hspace{0.5cm}} Al_2O_3.2SiO_2 + 2H_2Og \qquad 2.38$$

This process was accompanied by a reorganization of octahedrally coordinated aluminum in kaolinite to a more tetrahedrally coordinated aluminum in metakaolin resulting in sample shrinkage [Arato et al, 1995].

Chapter 5

CONCLUSION AND RECOMMENDATION

5.1. Conclusion

The Chemical composition of Eburru Kaolin, Eburru Fireclay, Mukurweini Ball Clay and Kwale Ilmenite Ore were found to be suitable to produce firebricks for utilization in waste incineration facilities locally. The AAS analysis indicated that Eburru Kaolin contained 24.74 % Al_2O_3, 72.64% SiO_2, and 0.71% Fe_2O_3; Eburru Fireclay contained 26.63% Al_2O_3, 66.40% SiO_2, and 2.78% Fe_2O_3; Mukurweini Ball Clay contained 36.85% Al_2O_3, 55.38% SiO_2, and 3.86% Fe_2O_3; and Kwale Ilmenite Ore was found to contain 44.60 % TiO_2 and 53.20 % Fe_2O_3.

The optimal formulation was 2 parts Kwale Ilmenite Ore, 43 parts Mukurweini Ball Clay, 100 parts Eburru Kaolin and 100 parts Eburru Fireclay. This formulation yielded sample firebricks with chemical composition 27.53 % Al_2O_3, 65.87 % SiO_2, 3.43 % TiO_2, 2.08 % Fe_2O_3 and 1.09 % others. The XRD analysis of the fired sample firebricks indicated the presence of 44.0 % mullite, $3Al_2O_3.2SiO_2$ and 18.5 % cristobalite, SiO_2. The optimal apparent porosity 36.45 %, bulk density 1.64g/cm^3 and compressive strength at room temperature of 20.6 N/mm^2 were obtained with fine to coarse to medium ratio of 2:1:2; water to binder to grog ratio of 7: 13: 30, firing rate of 50 ^{O}C/ hour at 1200 ^{O}C and a cooling rate of -16 ^{O}C/hour.

There was a correlation between processing conditions, mechanical and physical characteristics of the sample firebricks. The compressive strength at room temperature and bulk densities of Kwale Ilmenite Ore formulated firebricks increased significantly from 20.6 N/mm^2 and 1.61g/cm^3 from 20 N/mm^2 and 1.57g/cm^3 respectively. The particle size distribution, water to

binder to grog ratio and curing schedule significantly affected the mechanical and physical properties of the firebricks. The grog ratio reduced thermal stresses during firing as a result of mineral phase evolutions. The curing schedule rate of firing and cooling was critical for optimizing the mechanical parameters of the sample firebricks.

The pH of the sample firebrick 6.78 compared well with the standard of 6.00 to 8.00 and the firebricks can be utilized as incinerator lining with minimal corrosion from acidic or basic environment.

5.2. Recommendations.

The findings in this study were in agreement with the ones reported in literature [Rahman, 2012, Chukwudu, 2008; Arato et al, 1995; Harbison, 2005]. For pilot production of firebricks using Kwale Ilmenite Ore to be used as incinerator lining, this study recommends,

- Further Investigation of the effects of high temperatures curing, 1000 ^{O}C-1500 ^{O}C, on firebricks on strength, porosity, creep and bulk density. The mechanical and physical properties of firebricks improve with increasing firing temperature up to a maximum temperature approximately 1500 ^{O}C [Arato et al, 1995].

- Further study to enrich the formulation, standardization and use of local material for formulation of firebricks.

- A feasibility study on possibility of recycling and pilot production of refractory firebricks in Kenya. Grog i.e. recycled firebricks, consists of approximately 70% of material input in production of firebricks [Rahman, 2012]. Utilization of used bricks as a source of grog will drastically cut down the cost of production and mitigate environmental impact as a result of quarrying [Chukwudu, 2008].

- Pilot production and performance testing of the sample firebricks as a lining in the local incinerators. The cost per unit of the standard size firebrick was estimated at approximately Ksh 120 per piece.

REFERENCES

Abdel-Aziz, A.K., & Kabesh, A.M. (1991).

    Effect of sand particle size distribution of the ceramic properties of the fired clay bodies. Industrial ceramics 11[4], pp 188-192, Kuala Lumpur, Malaysia.

Abramowitz, M., & Stegun, I.A. (1972).

    Handbook of Mathematical Functions. Dove publications 3, pp 591. New York, USA.

African Economic Outlook, (2014).

    Kenya Economic Report. Government of Kenya. Nairobi, Kenya.

Ai-Bing, Y., Nicholas, S., & Arnold, M. (1993).

    Porosity calculation of Binary Mixtures of Non Spherical Particles. Journal of American Ceramic Society 6[11], pp 2813-2816. Wollongong, Australia.

Aly, F., & Semler, C. (1985).

    Prediction of Refractory Strength using Nondestructive Sonic Measurements. American Ceramic Society Bulletin 6[2], pp 1555-1558. Westerville, USA.

Anderson, C.A. (1996).

    Derivation of the Exponential Relation for the Effect of Ellipsoidal Porosity on Elastic Modulus. Journal of American Ceramic Society 9[2], pp 2181-2184. Wallingford, Pennsylvania.

Arato, P., Besenyei E., Kele, A., & Weber, F. (1995).

    Mechanical Properties in the Initial Stage of Sintering. Journal of Materials Science 30, pp 1863-1871. New York, USA.

Arato, P., Besenyei, E., Kele, A., & Weber, F. (1995).

Mechanical Properties in the Initial Stage of Sintering. Journal of Materials Science 30, pp 1863-1871. New York, US.

Arnold, M., Boccaccini, A.R., & Ondracek, G. (1996).

Prediction of the Poisson's Ratio of Porous Materials; Kluwer Academic Publishers 45, pp 1643-1646. Norwell, USA.

Arnold, E., Greenberg Lenore, S., Clescerl, & Andrew, D. E. (1992).

Standard Methods for the Examination of Water and Waste Water. American Public Health Association 18, pp 465-469. New York, USA.

Augusto, I., Pena, P., Sandoval, F., & Gonzalez, J. M. (1992).

Modification of the inert component in wall tile bodies. American Ceramic Society Bulletin 7[1], pp 1661-1668. New York, USA.

Bergeron & Risbud, (1984).

Introduction to Phase Equilibria in Ceramics. American Ceramic Society 2, pp 10-76. New York, USA.

Blanchart, P., & Gaillard, J.M. (1995).

The Drying of Clay Minerals and Mixed Clay Minerals. Journal of Material Science 30, pp 231-234. Paris, France.

Boccaccini, A.R. (1998).

Influence of Stress Concentrations on Mechanical Property-Porosity Correlation in Porous Materials. Journal of Material Science Letters 17, pp 1273-1275. Budapest, Hungary

Boccaccini, A.R. (1999).

Fabrication, Microstructural Characterization and Mechanical Properties of Glass compacts containing controlled porosity of spheroidal shape. Journal of Porous Materials 6, pp 369-379. Budapest, Hungary.

Boccaccini, A.R. (1994).

Comment on Dependence of Ceramic Fracture Properties on Porosity. Journal of Material Science Letters 30, pp 1035-1037. Birmingham, UK.

Boccaccini, A.R., Ondracek, G., Mazilu, P., & Windelberg, D. (1993).

On the effective Young's Modulus of Elasticity for Porous Materials: Microstructure modeling and Comparison between calculated and experimental values. Journal of Mechanical Behavior of Materials 4[2], pp 119-128. Birmingham, UK.

Boccaccini, N., & Boccaccini, A.R. (1997).

Dependence of Ultrasonic Velocity on Porosity and Pore shape in sintered materials. Journal of Nondestructive Evaluation 16[4], pp 187-192. Birmingham, UK.

Bogahawatta, V.T.L., & Poole, A.B. (1991).

Estimation of Optimal Firing Conditions for Kaolinite Clay Bodies. Journal of British Ceramic Transactions 90, pp 52-86. New York, USA.

Bogahawatta, V. T. L., & Poole, A.B. (1991).

Strength-Porosity-Mullite content Relationship for Kaolin Clay Bodies containing Lime additive. Journal of British Ceramic Transactions 61, pp 184-189. New York, USA.

Carniglia & Barna, (1992).

Handbook of Industrial Refractories Technology, Noyes Publication 11, pp 17-34. New Jersey, USA.

Carty, W.M., & Senapati, U. (1998).

Porcelain-Raw materials, Processing, Phase Evolution, and Mechanical Behavior. Journal of American Ceramic Society 81[1], pp 13-51. Birmingham, UK.

Chakraborty, A.K., & Ghosh, D.H. (1977).

Re-examination of the kaolinite-to-Mullite Reaction Series. Journal of the American Ceramic Society 61 [3], pp 170-173. Birmingham, UK.

Chan & Page, (1993).

Creep Damage Development in Structural Ceramics. Journal of American Ceramic Society 76, pp 803. New Jersey, USA.

Chandrasekhar, B.K., & Sampathkumar, N.N. (1996).

Refining of Cristobalite Porcelain. British Ceramic Transactions 95[2], pp 67-70. Birmingham, UK.

Chukwudu, B.C. (2008).

Characterization and Evaluation of the Refractory Properties of the Nsu Clay Deposit in Imo State Nigeria. Pacific Journal of Science and Technology 2, 67-121. Abuja, Nigeria.

Coquard, P., Boistelle, R., Amathiel, L., & Barriac, P. (1994).

Hardness, Elasticity Modulus and Flexion Strength of Dry Set Plaster. Journal of Material Science 29, pp 4611-4617. Birmingham, UK.

Cullity, B.D. (1959).

Elements of X-ray Diffraction. Addison-Wesley Publishers 2, pp 54-67. Reading, UK.

Deane, A. (1983).

Elastic Modulus of Porous Sintered Materials as Modeled by a variable-Aspect ratio self-consistent Oblate-spheroidal-inclusion theory. Journal of American Ceramic Society 66 [12], pp 847-857. New York, USA.

Dipak, R.B., & Fulrath, R.M. (1980).

Strength of Porous Polycrystalline Ceramics. British Ceramic Transactions 79 [1], pp 11-23. London, UK.

Environmental Liaison, Education & Action for Development, (2005).

A study on waste incineration activities in Nairobi that release dioxin and furan into the environment. Government of Kenya Press. Nairobi, Kenya.

Gaillard, J.M., Gault, C., Glandus, J.C., & Petrault, P. (1993).

Prediction of Tableware Deformations Using a Finite Element Analysis and the Measurements of Physical Parameters in Process Conditions. Industrial Ceramics 13 [1], pp 55-87. London, UK.

Gandi, C., Ashby, M. F., & Taplin, D. M. R. (1979).

Fracture Mechanism maps and their construction for metals and alloys.

Acta Metallurgia 3. London, UK.

Geith, M., Majcenovic & Wiry, A. (2001).

Processes Know How-Special Impregnation of Alumina Bricks to Increase Alkali Resistance. 54, pp 638-645. London, UK.

Government of Kenya, Central Bureau of Statistics, (2014).

Economic Survey Report 2014. Government of Kenya. Nairobi, Kenya

Government of Kenya, Central Bureau of Statistics, (2012).

Kenya Facts and Figures 2012. Government of Kenya. Nairobi Kenya

Government of Kenya, Kenya Institute of Public Policy and Research Analysis, (2013).

Kenya Economic Report: Creating Enabling Environment for Stimulating Investment for Competitive and Sustainable Counties. Government of Kenya. Nairobi, Kenya.

Government of Kenya, Ministry of Devolution & Planning, (2013).

Second Medium Term Plan 2013-2017: Pathway to Devolution, Socio-Economic, equity and National unity. Government of Kenya. Nairobi, Kenya.

Government of Kenya, Ministry of Environment & Natural Resources, (2006).

Mapping the Resources of Kenya. Government of Kenya. Nairobi, Kenya.

Government of Kenya, Ministry of Industrialization, (2013).

Sustainable Industrialization Report. Government of Kenya. Nairobi, Kenya.

Grimshaw, W. (1991).

The Chemistry and Physics of Clays, Ernest Ben Limited 3[3], pp 30-41. London, UK.

Harbison, (2005).

Handbook of Refractory Practice. Industrial Ceramics 5, pp 1-89. Pennsylvania, USA.

Hasselman, D.P.H. (1962).

On the Porosity Dependence of the elastic Moduli of Polycrystalline Refractory Materials. Journal of American Ceramic Society 45[9], pp 452-453. Pennsylvania, USA.

Hasselman, D.P.H., & Fulrath, R.M. (1967).

Microchemical stress concentrations in two phase Brittle-Matrix Ceramic Composites. Journal of American Ceramic Society 50[8], pp 399-404. Pennsylvania, USA.

Hayashi, T., & Shibuno, M. (1979).

Shingawa Technical Report. Journal of American Ceramic Society 3, pp 1-33. Shingawa, Tokyo, Japan.

Henry, A. L. (2008).

Methods of Analysis of Agricultural Chemist. Association of Official Agricultural Chemists 10, 1-53. Pennsylvania USA

Herakovich, C.T., & Baxter, S.C. (1999)

Influence of Pore Geometry on the Effective Response of Porous Media. Journal of Material Science 34, pp 1505-1609. Palo Alto, USA.

Hertzberg, (1967).

Deformation and Fracture Mechanism of Engineering Materials, John Wiley and Sons Inc., USA.

Hummel, F.A. (1951).

Thermal-Expansion properties of some synthetic Lithia minerals. Journal of American Ceramic Society 4, pp 235-239. John Wiley and Sons Inc., USA.

Ibisi, M.I. (1991).

The Firing Behavior of Some Nigerian Clays. Industrial ceramics 11[4], pp 183-186. Lagos, Nigeria.

Intermediate Technology Consultants, (2004).

Kenya Low Cost Waste Incinerator Country Review: Demand Survey and Country Selection Report. National Environmental Management Authority report. Nairobi, Kenya.

Jacques, P., & Bouchetou, M. L. (2006).

Refractories Applications Transactions. Journal of the American Ceramic Society 6, pp 123-154, Missouri USA.

Jokanovic & Spasic, (1992).

Synthesis of Mullite Nanostructured Spherical Powder by Ultrasonic Spray Pyrolysis. Elsevier Science 10, pp 7-26. New York, USA.

Kamran & Allaire, (2000).

Study the Microstructure changes during the Creep Process of Aluminosilicate Refractories used in Aluminum Industry. Tehrani International Conference Proceedings. Tehrani, Iran.

Karl, E. S., & Mark, D. A. (2002).

Thermodynamic Analysis of Alumina Refractory Corrosion by Sodium or Potassium Hydroxide in Glass Melting Furnaces. Journal of Material Science 31, pp 7-18. London, UK.

Kim, U., & Carty, W.M. (1998).

The effect of Clay Substitutions on the Plasticity of a typical whiteware body; in materials and equipment and whitewares, ceramic engineering and science proceedings. The American Ceramic Society 19 [2], pp 39-46. New York, USA.

Kingery, W. D., Bowen, H.K., & Uhlmman, R.D. (1991).

Introduction to Ceramics. John Wiley and Sons 4, pp 78-80, 355-386, 532-540. New York, London.

Kingery, (1967).

Introduction to Ceramics, John Wiley and Sons 2, pp 355-540. New York, London.

Knudsen, F.P. (1959).

Dependence of Mechanical Strength of Brittle Polycrystalline Specimens on Porosity and Grain Size. Journal American Ceramic Society; 42[8], pp 366-387. Delhi, India.

Knudsen, F.P. (1962).

Effect of Young's modulus of Alumina. Journal of the American Ceramic Society-Discussions and Notes. Delhi, India.

Kobayashi, Y., Osamu, O., Ohashi, Y., & Kato, E. (1992).

Effect of Firing Temperature on the Bending Strength of Ceramic materials for Tableware. Journal of American Ceramic Society 5 [7], pp 1801-1806. Aichi, Japan.

Kobayashi, Y., Osamu, O., Ohashi, Y., & Kato, E. (1994).

Composition for Strengthening Ceramic Bodies in Alumina-Feldspar-Kaolin systems. British Ceramic Transactions Journal 9[2], pp 49-52. Toki, Japan.

Krishna, P.K., Franklin, J. S., & Senith, S. (2013).

A study on the progress of Indian Cement Industry. European Centre for Research, Training and Development 11, pp 72-90. London, UK.

Kshama, V.D., Mohan, B. V., & Lilithambika, M. (1992).

Sintering Studies on Plastic Clays. Ceramics 18, 359-364. Delhi, India.

Kubicki, B. (1995).

Stress Concentration at Pores in Sintered materials. Powder metallurgy 8[4], pp 295-298. Kolkata, India.

Kulkarini, N., Mouudgil, B. & Bhardwaj, M., (1994).

Ultrasonic Characterization of Green and Sintered Ceramics II, Frequency Domain. American Ceramic Society Bulletin 6 [3], pp 83-85, Kolkata, India.

Levin, E.M., Robbins, C.R., & MCMurdie, H.F. (1979).

Phase Diagrams for Ceramists. American Ceramic Society 11, pp 156-158. Michigan, USA.

Maitra & Phani, (1994).

Ultrasonic Evaluation of Elastic Parameters of Sintered Powder Compacts. Journal of Material Science. London, UK.

Manning, W. R., Hunter, O. Jr., & Powell, B. R. Jr. (1968).

Elastic Properties of Polycrystalline Tritium Oxide, Dysprosium Oxide, Holmium Oxide and Erbium Oxide. Journal of American Ceramic Society. Washington D. C., USA.

Martin, L. P., Daddon, D., & Rosen, M. (1996).

Evaluation of Ultrasonically Determined Elastic-Porosity Relation in ZnO. Journal of American Ceramic Society. London, UK.

Matsui, K., Kawano, F. & Naibi, K. (1991).

Refractories. Elsevier Science Ltd 43, pp 442-450. Toki, Japan.

Mattyasovsky-Zsolnay, (1997).

Mechanical Strength of Porcelain. Journal of American Ceramic Society 40 [9]. Berlin, German.

Mazilu & Ondracek, (1989).

Effective Young's Modulus-Porosity of Elasticity for Porous Materials: The General Model Equation, in Thermal Effects in Fracture of Multiphase Materials. Proceedings of Euromechanical Colloquim. Berlin, German.

Mori & Tanaka, (1973).

Average Stress in Matrix and Average Elastic Energy of Materials with Misfitting Inclusions. Acta Metallurgica. London, UK.

Mukhopadhyay & Phani, (1998).

Young's Modulus Porosity Relations: An analysis based on a Minimum Contact Area Model. Journal of Materials Science. London, UK.

Naga, S. M., Sallam, E. M. H., & Elaziz, D. A.A. (1993).

Assessment of Some Egyptian Basalt and Low Grade Clays for Ceramic Tiles Manufacture. Industrial Ceramics. Manchester, UK.

Narita, K., Onoye, T., Satoh, Y., Miyamoto, M., Taniguchi, K., Kamatani, S., Sato, T., & Fukihara, S. (1981).

Effects of Alkalis and Zinc on the Wear of Blast Furnace Refractories and the Tuyere Displacement. Transactions ISIJ 21, pp 839-845. Toki, Japan.

Ngai, K.L. & Yung Wang, C.T. (2002).

Moynihan, the mixed Alkali Effect Revised: The Importance of Ion-Ion Interactions. Journal of Non crystalline solids 5, pp 301-310, 999-1011. Delhi, India.

Nielson, (1984).

Elasticity and Damping of Porous and Impregnated Materials. Journal of American Ceramic Society. Wollongong, Australia.

Nyongesa, F. W. (1994).

Ultrasonic Characterization of Kenyan Clay Refractories. Msc Thesis University of Nairobi. Nairobi, Kenya.

Ohya & Takahashi, (1999).

Acoustic Emission from a Porcelain Body during Cooling. Journal of American Ceramic Society. Tokyo, Japan.

Panakkal, J. P. (1991).

Use of Longitudinal Ultrasonic Velocity as a Predictor of Elastic Moduli and Density of Sintered Uranium Dioxide, IEEE Transactions on Ultrasonics, Ferroelectrics, and Frequency Control. London, UK.

Papargyris, A. D., & Cooke, R. D. (1996).

Structure and Chemical Properties of Kaolin Based Ceramics. British Ceramic Transactions. London, UK.

Peacor, D. R., Roland, C. R., & Edward, S. G. (1999).

Structure of boralsilite and its relation to a family of boroaluminosilicates, silimanite, and andalusite. American Mineralogist. Washington D.C., USA.

Phani, K.K. (1996).

Porosity Dependence of Ultrasonic Velocity in Sintered Materials- A model Based on the Self-Consistent Spheroidal Inclusion Theory. Journal of Material Science 11, PP 167-2001. Kuala Lumper, Malaysia.

Phani & Niyogi, (1987a).

Young's Modulus of Porous Brittle Solids, Journal of Material Science. London, UK.

Phani & Niyogi, (1987b)

Elastic Moduli Porosity Relation in Polycrystalline Rare Earth Oxides. Journal of American Ceramic Society. New York, USA.

Phani & Niyogi, (1987).

Elastic Modulus Porosity Relationship in Brittle Solids in High Tech Ceramics. Elsevier's Science Publisher. Amsterdam, Netherlands. .

Phani, (1996).

Nondestructive Characterization of Zirconia Toughened Alumina Ceramics using Ultrasonic. Central Glass and Ceramic Research Institute 31, pp 1021-1026. Kolkata, India.

Pickup, P. (1997).

Effect of Porosity on Young's Modulus of Porcelain. British Ceramic Transactions 5 [3], pp 111-140. London, UK..

Rahman, (2012).

Properties of Fireclay after Dressing and the Effect of Grog. Bangladesh University of Engineering and Technology. Dhaka, Bangladesh.

Ramachandran, V.S., & Beaudon, J. J. (2001).

Handbook of Analytical Techniques in Concrete Science and Technology. Pergamon press. New York, USA.

Ramakrishnan & Arunachalam, (1993).

Effective Elastic Moduli of Porous Ceramic Materials. Journal of American Ceramic Society. New York, USA.

Reed, S.J. (1987).

Introduction to Principals of Ceramic Processing. John Wiley and Son Ltd. Manchester, UK.

Rice, R.W. (1997).

Limitations of Pore-Stress Concentrations on the Mechanical Properties of Porous Materials. Journals of Material Science. London, UK.

Rice, R. W., (1993a).

Evaluating Porosity Parameters for Porosity Property Relations. Journal of American Ceramic Society. Texas, USA.

Rice, R. W, (1993b).

Comparison of Stress Concentration versus Minimum Solid Area Based Mechanical Property Porosity Relations. Journal of Material Science. Moscow, Russia.

Rice, R. W. (1996a).

Evaluation and Extension of Physical Property-Porosity Models based on Minimum Solid Area. Journal of Material Science. Moscow, Russia.

Rice, R. W. (1996b).

Comparison of Physical Property Porosity Behavior with Minimum Solid Area. Journal of Material Science. Berlin, German.

Richerson, (1982).

Modern Ceramic Engineering Properties, Processing and Use in Design. Journal of Material Science. Texas, USA.

Saggio-Woyansky & Curtis, (1992).

Processing of Porous Ceramics. American Ceramic Society Bulletin. Washington D.C., USA.

Sane & Ralph, (1995).

Effect of Grinding and Firing Treatment on the Crystalline and Glass Content and the Physical Properties of Whiteware Bodies. Journal of American Ceramic Society. Texas, USA.

Schneider, H., Schrener, J., & Hildmann, B. (2008).

Structure and Properties of Mullite-A Review. Journal of the European Ceramics Society 8, PP 329-334. Liverpool, UK.

Schneider, Okada K., & Pask, J. (1994).

Mullite and Mullite Ceramics. John Wiley and Sons. Chichester, UK.

Sherby, O. D., & Burke, P.M. (1968).

Mechanical behavior of crystalline solids at elevated temperature. Elsevier ltd. Manchester, UK.

Sherby, O. D., & Lytton, J. L. (1956).

Effect of the crystal system on high-temperature strength-titanium and thallium; Elsevier ltd. Chichester, UK.

Shi, (1999).

Thermodynamic and Densification Kinetics in Solid State Sintering of Ceramics. Journal of Material Research. Tokyo, Japan.

Singh, (1996).

Sintering Study of Calcium Aluminate. Journal of Material Science. Kuala Lumper, Malaysia.

Soroka & Sereda, (1967).

Interrelation of Hardness, Modulus of Elasticity and Porosity in various Gypsum Systems. Journal of American Ceramic Society. New York, USA.

Spriggs, (1961).

Expression for Effect of Porosity on Elastic Moduli of Polycrystalline Refractory Materials, Particularly Al_2O_3. Journal of American Ceramic Society. Kolkuta, India.

Step-by-Step Group, (2004).

Waste Management Assessment and Recommendations Report. Nairobi, Kenya.

Stjernberg, J., Lindblom, B., Wikstrom, J., Antti, M. L., & Oden, M. (2010).

Microstructural characterization of Alkali Metal Mediated High Temperature Reactions in Mullite based Refractories. Ceramics International 7, pp 733-740. Berlin, German.

Sudduth, (1995).

Generalized Model to Predict the Effect of Voids on Modulus in Ceramics. Journal of Material Science. Birmingham, UK.

Suryanarayana, C., & Norton, M. (1998).

X-ray Diffraction, A practical Approach. Pergamon Press. London, UK.

Ting & Lin, (1994a).

Effect of Particle Size Distribution on Sintering: Part I Modelling. Journal of Material Science. Tokyo, Japan.

Ting and Lin, (1994b).

Effect of Particle Size Distribution on Sintering: Part II Sintering of Al_2O_3 Cambridge, UK.

Ullman, F., Barbara, E., Stephens, H., & William E.R. (1994).

Ullman's Encyclopedia of Industrial Chemistry. Cambridge, UK.

Varian, (1979).

Analytical Methods for Flame Spectroscopy. Varian Techtron Pty Ltd. Springvale, Australia.

Vary, A. (1988).

Ultrasonic Measurements of Mechanical Properties. Elsevier Science Ltd. Clevelend, Ohio, USA.

Viswabaskavan, V., Gnenam, F. D., & Balasubramanian, (2002).

Mullitazation Behavior of South Indian Clays. Ceramic Internationals 8, pp 557-564. Kolkuta, India.

Wagh, A. S., Poeppel, R. B. and Singh, J. P., (1991).

Open Pore Description of Mechanical Properties of Ceramics. Journal of Material

Science. New York, USA.

Wagh A. S, Poeppel, R. B. and Singh, J. P., (1993).

Dependence of Ceramic Fracture Properties on Porosity. Journal of Material

Science. London, UK.

Winker, H.G.F. (1953).

Effects of Lithium Alumina Silicates. Acta Crystal. London, UK.

Wong, p., Koplik, J., & Tomanic, J. P. (1984).

Conductivity and Permeability of Rocks. Physical Review. Tokyo, Japan.

World Bank, (2013).

Kenya Economic Update: accelerating growth and poverty reduction in new

Kenya. Poverty reduction and Economic Management Unit Africa Region.

Nairobi, Kenya.

Worrall, (1986).

Clays and Ceramic Raw Materials. Elsevier Applied Science Publishers. New

York.

Wu, T. T. (1966).

The effect of inclusion shape on the elastic modulus of a two phase material.

International Journal of Solid Structures. London, UK.

Zhang, S. & Lee, W. E., (2000).

Use of phase diagrams in studies of refractories corrosion. International Material

Revision 4 [2], 41-58. Tokyo, Japan.

Zheng & Reed, (1992).

The Different Roles of Firing and Sintering on Densification of Powder Compacts. American Ceramic Society Bulletin. Texas, USA.

Zimmermann & Julien, (2007).

Study of Reactions between iron-ore slag and Refractories. Science Direct. Lulea University of Technology, Sweden.

Zuokai, (1990).

Fracture Initiating Flaws in Aluminous Electrical Porcelain. Ceramic Bulletin 3 [3], pp 71-106. Kolkuta, India.

APPENDICES

Appendix 1: Eshelby's tensor for elasticity

Eshelby's (υ) tensors S_{ijkl} for isotropic matrix are a function of the geometry of ellipsoid with axes a_1, a_2 and a_3 and poisons of the matrix (υ). In the following are the Eshelby's tensors for ellipsoids with simple geometry.

The domain of an ellipsoidal inclusion is bounded by

$$\frac{x_1^2}{a_1^2} + \frac{x_2^2}{a_2^2} + \frac{x_3^3}{a_3^3} = 1 \tag{A-1}$$

Where a_1, a_2, and a_3 are the principal axes of the ellipsoid and coincide with the x_1, x_2, and x_3 axes, respectively. S_{ijkl} satisfies the symmetry; $S_{ijkl}=S_{ijkl}=S_{ijkl}$.

(a) Oblate spheroid: $a_1=a_2>a_3$ (Fig. 5, Chapter 2, sub-section 2.3.4)

$$S_{111} = S_{222} = -\frac{3}{8(1-\upsilon)}\frac{\alpha^2}{(1-\alpha^2)} + \frac{1}{4(1-\upsilon)}\left\{1 - 2\upsilon + \frac{9}{4(1-\alpha^2)}\right\}g \tag{A-2}$$

$$S_{333} = \frac{1}{2(1-\upsilon)}\left\{4 - 2\upsilon - \frac{2}{(1-\alpha^2)}\right\} + \frac{1}{2(1-\upsilon)}\left\{-4 + 2\upsilon + \frac{3}{1-\alpha^2}\right\}g \tag{A-3}$$

$$S_{1122} = S_{2211} = \frac{1}{8(1-\upsilon)}\left\{1 - \frac{2}{1-\alpha^2}\right\} + \frac{1}{16(1-\upsilon)}\left\{-4(1 - 2\upsilon) + \frac{3}{1-\alpha^2}\right\}g \tag{A-4}$$

$$S_{1133} = S_{2233} = \frac{1}{2(1-\upsilon)}\frac{\alpha^2}{(1-\alpha^2)} - \frac{1}{4(1-u)}\left\{1 - 2\upsilon + \frac{3\alpha^2}{(1-\alpha^2)}\right\}g \tag{A-5}$$

$$S_{3311} = S_{3322} = \frac{1}{2(1-\upsilon)}\left\{-(1 - 2\upsilon) + \frac{2}{1-\alpha^2}\right\} + \frac{1}{4(1-\upsilon)}\left\{2(1 - 2\upsilon) - \frac{3}{1-\alpha^2}\right\}g \tag{A-6}$$

$$S_{1212} = -\frac{1}{8(1-\upsilon)}\frac{\alpha^2}{(1-\alpha^2)} + \frac{1}{16(1-\upsilon)}\left\{\frac{3}{1-\alpha^2} + 4(1 - 2\upsilon)\right\}g \tag{A-7}$$

$$S_{1313} = S_{2323} = \frac{1}{4(1-\upsilon)}\left\{1 - 2\upsilon + \frac{(1+\alpha^2)}{(1-\alpha^2)}\right\} - \frac{1}{8(1-\upsilon)}\left\{1 - 2\upsilon + \frac{3(1+\alpha^2)}{(1-\alpha^2)}\right\}g \tag{A-8}$$

Where

125

$$\alpha = \frac{a_3}{a_1} < 1 \tag{A-9}$$

$$g = \alpha/(1-\alpha^2)^{\frac{3}{2}} \left\{ \cos^{-1}\alpha - \alpha(1-\alpha^2)^{1/2} \right. \tag{A-10}$$

(b) Prolate spheroid: $a_1 = a_2 < a_3$ (Fig. 6, Chapter 2, sub-section 2.3.4)

$$S_{1111} = S_{2222} = \frac{3}{8(1-\upsilon)} \frac{\alpha^2}{(\alpha^2-1)} + \frac{1}{4(1-\upsilon)} \left\{ 1 - 2\upsilon - \frac{9}{4(\alpha^2-1)} \right\} g \tag{A-11}$$

$$S_{3333} = \frac{1}{2(1-\upsilon)} \left[1 - 2\upsilon + \frac{(3\alpha^2-1)}{(\alpha^2-1)} - \left\{ 1 - 2\upsilon + \frac{3\alpha^2}{\alpha^2-1} \right\} \right] g \tag{A-12}$$

$$S_{3333} = S_{2211} = \frac{1}{4(1-\upsilon)} \left[\frac{\alpha^2}{2(\alpha^2-1)} - \left\{ 1 - 2\upsilon + \frac{3}{4(\alpha^2-1)} \right\} \right] g \tag{A-13}$$

$$S_{1133} = S_{2233} = -\frac{1}{2(1-\upsilon)} \frac{\alpha^2}{\alpha^2-1} + \frac{1}{4(1-\upsilon)} \left\{ \frac{3\alpha^2}{(\alpha^2-1)} - (1-2\upsilon) \right\} g \tag{A-14}$$

$$S_{3311} = S_{3322} = -\frac{1}{2(1-\upsilon)} \left\{ 1 - 2\upsilon + \frac{2}{(\alpha^2-1)} \right\} + \frac{1}{2(1-\upsilon)} \left\{ 1 - 2\upsilon + \frac{3}{2(\alpha^2-1)} \right\} g \tag{A-15}$$

$$S_{1212} = \frac{1}{8(1-\upsilon)} \frac{\alpha^2}{(\alpha^2-1)} + \frac{1}{4(1-\upsilon)} \left\{ 1 - 2\upsilon - \frac{3}{4(\alpha^2-1)} \right\} g \tag{A-16}$$

$$S_{2323} = S_{1313} = \frac{1}{4(1-\upsilon)} \left\{ 1 - 2\upsilon + \frac{(\alpha^2+1)}{(\alpha^2-1)} \right\} - \frac{1}{8(1-\upsilon)} \left\{ 1 - 2\upsilon + \frac{3(\alpha^2+1)}{(\alpha^2-1)} \right\} g \tag{A-17}$$

Where

$$\alpha = a_3/a_1 > 1 \tag{A-18}$$

$$g = \frac{\alpha}{(\alpha^2-1)^{3/2}} \left\{ \alpha \left(\alpha^2 - 1 \right)^{\frac{1}{2}} - \cosh^{-1}\alpha \right\} \tag{A-19}$$

Appendix 2: Tables of Results

Table 18: % Elemental Composition and Loss on Ignition

	SiO_2	Al_2O_3	CaO	MgO	Na_2O	K_2O	TiO_2	MnO	Fe_2O_3	% LOI	Total	Recovery
KITO	0.79	0.38	0.14	0.62	0.11	0.04	44.6	0.60	53.2	NIL	100.48	0.48
EK	66.95	22.8	0.10	0.16	0.12	0.05	0.67	0.20	0.65	7.83	99.53	0.47
EF	60.07	24.0	0.25	0.19	0.15	0.17	2.03	0.20	2.45	9.86	99.37	0.63
MBC	47.19	31.4	0.02	0.26	0.37	0.97	2.52	0.03	3.26	14.79	100.81	0.81

The Loss on Ignition, LOI, was computed as:

$$\% \text{ LOI} = \left\{ \frac{\text{Initial weight} - \text{Final weight}}{\text{Initial weight}} \right\} 100$$

Table 19: Effects of Particle Size Distribution on Bulk Density. Compressive Strength and Apparent Porosity

	S_A		S_B		S_C		S_D		S_E		S_F		S_G	
	A_1	A_2	B_1	B_2	C_1	C_2	D_1	D_2	E_1	E_2	F_1	F_2	G_1	G
Dry weight, kgs	1.02	1.02	1.00	1.00	0.99	0.99	1.00	1.00	1.00	1.00	1.02	1.02	1.00	1.
Soaked weight, kg	1.3220	1.3220	1.2501	1.2501	1.214	1.2114	1.2387	1.2387	1.2825	1.2825	1.2967	1.2967	1.3134	1.34
Suspended weight, kgs	0.6465	0.6465	0.6091	0.6091	0.6003	0.6003	0.6058	0.6058	0.6289	0.6289	0.63	0.63	0.6467	0.67
Soaked weight-suspended weight	0.6755	0.6755	0.6410	0.6410	0.6111	0.6111	0.6299	0.6299	0.6536	0.6536	0.6667	0.6667	0.6667	0.67

Soaked weight – dry weight	0.302	0.302	0.2501	0.2501	0.2214	0.2214	0.2387	0.2387	0.2825	0.2825	0.2767	0.2767	0.3134	0.34
Bulk density, g/cm^3	1.51	1.51	1.56	1.56	1.62	1.62	1.58	1.58	1.53	1.53	1.53	1.53	1.50	1.
% apparent porosity	44.71	44.71	39.02	39.02	36.23	36.23	37.71	37.71	43.22	43.22	42.24	42.24	47.01	47.1
Maximum load, kN	110.25	110.25	128.25	128.25	155.25	155.25	134.25	134.25	105.75	105.75	114	114	85.5	85
Length by Width, cm	10.X 7..5													
Surface area, cm^2	75													
Compressive strength (kN/cm^2)	1.47	1.47	1.71	1.71	2.07	2.07	1.79	1.79	1.41	1.41	1.52	1.52	1.14	1.

Table 20: Effects of Grog to Binder Ratio on Mechanical and Physical Properties

	S_{AA}		S_{BB}		S_{CC}		S_{DD}		S_{EE}	
	SAA_1	SAA_2	SBB_1	SBB_2	SCC_1	SCC_2	SDD_1	SDD_2	SEE_1	SEE
Dry weight, kgs	1.00	1.00	1.05	1.05	1.00	1.00	0.99	0.99	1.02	1.02
Soaked weight, kg	1.3111	1.3111	1.3219	1.3219	1.2316	1.2316	1.2446	1.2446	1.3097	1.30
Suspended weight, kgs	0.6214	0.6214	0.6552	0.6552	0.6027	0.6027	0.6077	0.6077	0.6516	0.65
Soaked weight-suspended weight	0.6897	0.6897	0.6667	0.6667	0.6289	0.6289	0.6369	0.6369	0.6581	0.65
Soaked weight – dry weight	0.3111	0.3111	0.2719	0.2719	0.2316	0.2316	0.2546	0.2546	0.2897	0.28
Bulk density, g/cm^3	1.45	1.45	1.50	1.50	1.59	1.59	1.57	1.57	1.55	1.55
% apparent porosity	45.11	45.11	40.77	40.77	36.82	36.82	39.97	39.97	44.01	44.0
Maximum load, kN	79.5	79.5	133.5	133.5	149.25	149.5	147	147	142.5	142.
Length by Width, cm	10 x 7.5									
Surface area, cm^2	75									
Compressive strength (kN/cm^2)	1.06	1.06	1.78	1.78	1.99	1.99	1.96	1.96	1.90	1.90

Table 21: Effects of Water on Bulk Density and Apparent Porosity

	SW$_1$		SW$_2$		SW$_3$		SW$_4$		SW$_5$	
	W$_{1A}$	W$_{1B}$	W$_{2A}$	W$_{2B}$	W$_{3A}$	W$_{3B}$	W$_{4A}$	W$_{4B}$	W$_{5A}$	W$_{5B}$
Dry weight, kgs	1.00	1.00	1.00	1.00	1.02	1.02	0.99	0.99	1.01	1.01
Soaked weight, kg	1.3876	1.3876	1.2720	1.2720	1.2794	1.2794	1.2217	1.2217	1.2869	1.286
Suspended weight, kgs	0.60 02	0.6002	0.6009	0.6009	0.6127	0.6127	0.5951	0.5951	0.6136	0.613
Soaked weight- suspended weight	0.7874	0.7874	0.6711	0.6711	0.6667	0.6667	0.6266	0.6266	0.6733	0.673
Soaked weight – dry weight	0.3876	0.3876	0.272	0.272	0.2594	0.2594	0.2317	0.2317	0.2769	0.276
Bulk density, g/cm^3	1.27	1.27	1.49	1.49	1.53	1.53	1.58	1.58	1.50	1.50
% apparent porosity	49.23	49.23	40.53	40.53	38.91	38.91	36.97	36.97	41.12	41.12

Table 22: Effects of Curing Time on Mechanical and Physical Properties

	SRTO$_0$		SRTO$_1$		SRTO$_2$		SRTO$_3$		SRTO$_4$		SRTO$_5$	
	T$_{0A}$	T$_{0B}$	T$_{1A}$	T$_{1B}$	T$_{2A}$	T$_{2B}$	T$_{3A}$	T$_{3B}$	T$_{4A}$	T$_{4B}$	T$_{5A}$	T$_{5B}$
Dry weight, kg	1.00	1.00	0.98	0.98	0.99	0.99	1.00	1.00	1.00	1.00	1.01	1.01
Soaked weight, kg	1.2341	1.2341	1.2299	1.2299	1.2257	1.2257	1.2401	1.2401	1.2383	1.2383	1.2365	1.2365
Suspended weight, kgs	0.5492	0.5492	0.4582	0.4582	0.5285	0.5285	0.5598	0.5598	0.5672	0.5672	0.5632	0.5632
Soaked weight-suspended weight	0.6849	0.6849	0.7717	0.7717	0.6972	0.6972	0.6803	0.6803	0.6711	0.6711	0.6733	0.6733
Bulk density, g/cm^3	1.46	1.46	1.27	1.27	1.42	1.42	1.47	1.47	1.49	1.49	1.50	1.50
Maximum load, kN	80.11	82.89	79.23	85.77	110.5	114.5	122.5	132.5	144.25	154.25	151.4	148.6
Length by Width, cm	10 X 7.5	9.9 X 7.5	10 X 7.5	10 X 7.5	9.9 X 7.5	10 X 7.4	10 X 7.5	10 X 7.5	10 X 7.5	10 X 7.5	9.9 X 7.5	10 X 7.5
Surface area, cm^2	75	74.25	75	75	74.25	74	75	75	75	75	74.25	75
Compressive strength (N/cm^2)	1.07	1.12	1.06	1.14	1.49	1.55	1.63	1.77	1.92	2.06	2.04	1.98

Table 23: Effects of **KITO** on Mechanical and Physical Properties

	STO$_0$		STO$_1$		STO$_2$		STO$_3$		STO$_4$	
	TO0$_A$	TO0$_B$	TO1$_A$	TO1$_B$	TO2$_A$	TO2$_B$	TO3$_A$	TO3$_B$	TO4$_A$	TO4$_B$
Dry weight, kgs	1.00	1.00	1.00	1.00	1.00	1.00	1.02	1.02	0.99	0.99
Soaked weight, kg	1.2283	1.2283	1.2327	1.2327	1.2286	1.2286	1.2595	1.2595	1.2157	1.2157
Suspended weight, kgs	0.6072	0.6072	0.6038	0.6038	0.6036	0.6036	0.6098	0.6098	0.6008	0.6008
Soaked weight-suspended weight	0.621	0.621	0.6289	0.6289	0.6250	0.6250	0.6497	0.6497	0.6149	0.6149
Soaked weight – dry weight	0.2283	0.2283	0.2327	0.2327	0.2286	0.2286	0.2395	0.2395	0.225	0.225
Bulk density, g/cm^3	1.61	1.61	1.59	1.59	1.60	1.60	1.57	1.57	1.61	1.61
% apparent porosity	36.78	36.78	37.01	37.01	36.58	36.58	36.87	36.87	36.70	36.70
Maximum load, kN	149.25	149.25	150.75	150.75	148.50	148.50	150.00	150.00	155.25	155.25
Length by Width, cm	10 x 7.5									
Surface area, cm^2	75									
Compressive strength (kN/cm	1.99	1.99	2.01	2.01	1.98	1.98	2.00	2.00	2.07	2.07

Appendix 3: Rationale Analysis Method

In this method, CaO, Na_2O and K_2O were assumed to exist as; Anorthite, $CaO.Al_2O_3.2SiO_2$; Orthoclase, $K_2O.Al_2O_3.6SiO_2$; and Albite, $Na_2O.Al_2O_3.6SiO_2$. To calculate the mineral compositions in EK, EF, MBC and KITO, mole equivalent of SiO_2 and Al_2O_3 combined in Anorthite, Orthoclase and Albite were subtracted from their original amounts. The remaining Al_2O_3 was assigned to kaolinite, $Al_2O_3.2SiO_2.2H_2O$, together with the required SiO_2 and H_2O. MgO was assigned: magnesite, $MgCO_3$; or dolomite, $MgCO_3.CaCO_3$; or serpentine $3MgO.2SiO_2.2H_2O$; and or talc $3MgO.4SiO_2.H_2O$. Fe_2O_3 was assigned to hematite, Fe_2O_3. Since there was more LOI after subtraction of H_2O from kaolinite and talc, it was assigned to limonite, $Fe_2O_3.H_2O$, though that was not the case upon confirmation of existence of pyrite, FeS, in the samples. In KITO samples CO_2 emission was clear, hence the equivalent CaO was considered as limestone. Since kaolinite and orthoclase, existed in EK, EF and MBC, the existence of muscovite, $K_2O.3Al_2O_3.6SiO_2.2H_2O$, was clear, but it was impossible to ascertain its content. However, even if K_2O originated from feldspar or muscovite, the source of K_2O has less influence on the properties of the firebricks. TiO_2 was allotted to Ilmenite, $Fe_2O_3.TiO_2$. Since Fe_2O_3 in KITO was not enough to allot to Ilmenite, a part of TiO_2 was assigned to rutile, TiO_2. In all cases Loss on Ignition was assumed to be H_2O.

Table 24: Eburru Kaolin Inorganic Oxides Mole Equivalent

Element Oxide	Content (wt %)	Molecular weight	Mole equivalent
SiO_2	66.95	60.1	1.1140
Al_2O_3	22.80	102.0	0.2235
Fe_2O_3	0.65	160.0	0.0041
K_2O	0.05	94.2	0.0005
Na_2O	0.12	62.0	0.0019
TiO_2	0.67	79.9	0.0084
CaO	0.10	56.1	0.0018
MgO	0.16	40.3	0.0040
MnO	0.20	86.9	0.0023
LOI	7.83	18.0	0.4350

Table 25: Eburru Kaolin Mineral Content

	SiO_2	Al_2O_3	Fe_2O_3	CaO	K_2O	Na_2O	H_2O
Mole equivalent	1.1140	0.2235	0.0041	0.0018	0.0005	0.0019	0.4350
0.0005mol orthoclase	0.003	0.0005			0.0005		
Remain	1.1110	0.2230			0.0000		
0.0019 mol Albite	0.0114	0.0019				0.0019	
Remain	1.0996	0.2211				0.0019	
0.0018 mol Anorthite	0.0036	0.0018		0.0018			
Remain	1.0960	0.2193		0.0000			
0.2193 kaolinite	0.4386	0.2193					0.4386
Remain	0.6574						0.0000
0.6574 mol quartz	0.6574						
Remain							
0.0041 mol Hematite			0.0041				
Remain			0.0041				

Table 26: % Mineral Phases in Eburru Kaolin

Mineral	Mol. equivalent	Mol. weight	Weight	Weight %
Orthoclase	0.0005	557	= 00.2785	0.28
Albite	0.0019	524	= 00.9956	1.00
Anorthoclase	0.0018	279	= 00.5022	0.50
Kaolinite	0.2193	258	= 56.5800	56.58
Hematite	0.0041	100	= 00.4100	0.41
Quartz (Free)	0.6574	60.1	= 39.5100	39.51
Total			98.28	

Table 27: KITO Inorganic Oxides Mole Equivalent

Element Oxide	Content (wt %)	Molecular weight	Mole equivalent
SiO_2	0.79	60.1	0.0131
Al_2O_3	0.38	102.0	0.0037
Fe_2O_3	53.2	160.0	0.3325
CaO	0.14	56.1	0.0025
Na_2O	0.11	62.0	0.0018
K_2O	0.04	94.2	0.0004
MgO	0.62	40.3	0.0154
TiO_2	44.60	79.9	0.5582
MnO	0.60	86.9	0.0069
LOI	NIL	18.0	0.0000

Table 28: KITO Mineral Mole Content

	SiO_2	Al_2O_3	Fe_2O_3	CaO	K_2O	Na_2O	TiO_2	H_2O
Mole equivalent	0.0131	0.0037	0.3325	0.0025	0.0004	0.0018	0.5582	0.00
0.0004 mol orthoclase	0.0024	0.0004			0.0004			
Remain	0.0107	0.0033			0.0000			
0.0018 mol Albite	0.0108	0.0018				0.0018		
Remain	0.0000	0.0015				0.0000		
0.0000 mol Anorthite	0.0000	0.0000		0.0000				
Remain	Nil	0.0015		0.0025				
0.0000 mol kaolinite	Nil	0.0000		0.0000				
Remain	Nil	0.0015		0.0025				
0.0000 mol quartz	0.0000	0.0000		0.0000				
Remain	Nil	0.0015		0.0025				
0.0025 mol limestone	-	0.0000		0.0025				
Remain	-	0.0015		0.0000				
0.0015 alumina	-	0.0015		-				
Remain		0.0000						
0.3325 mol Ilmenite	-	-	0.3325	-	-	-	-	0.3325
Remain			0.0000					0.2257
0.2257 mol Rutile								0.2257
Remain								0.0000

Table 29: KITO % Mineral Content

Mineral	Mol. equivalent	Mol. weight	Weight	Weight %
Orthoclase	0.0004	557	=0.22	0.22
Albite	0.0018	524	= 0.94	0.94
Corundum	0.0015	102.0	= 0.15	0.15
limestone	0.0025	56.1	= 0.14	0.14
ilmenite	0.3325	239.9	= 79.77	79.77
Rutile	0.2257	79.9	= 18.03	18.03
Total			99.25	

Table 30: MBC Minerals Mole Equivalent

Element Oxide	Content (wt %)	Molecular weight	Mole equivalent
SiO_2	47.19	60.1	0.7852
Al_2O_3	31.40	102.0	0.3078
Fe_2O_3	3.26	160.0	0.0204
CaO	0.02	56.1	0.0004
Na_2O	0.37	62.0	0.0060
K_2O	0.97	94.2	0.0103
MgO	0.26	40.3	0.0065
TiO_2	2.52	79.9	0.0315
MnO	0.03	86.9	0.0003
LOI	14.79	18.0	0.8217

Table 31: MBC Mineral Mole Content

	SiO$_2$	Al$_2$O$_3$	Fe$_2$O$_3$	CaO	K$_2$O	Na$_2$O	TiO$_2$	H$_2$O
Mole equivalent	0.7852	0.3078	0.0204	0.0004	0.0103	0.0060	0.0315	0.8217
0.0103mol orthoclase	0.0618	0.0103			0.0103			
Remain	0.7234	0.2875			0.0000			
0.0060 mol Albite	0.0360	0.0060				0.0060		
Remain	0.6874	0.2815				0.0000		
0.0004 mol Anorthite	0.0008	0.0004		0.0004				
Remain	0.6866	0.2811		-				
0.2811 mol kaolinite	0.5622	0.2811						0.5622
Remain	0.1244	-						0.2595
0.1244 mol quartz	0.1244	-						
Remain	-							
0.0204 mol ilmenite	-	-	0.0204				0.0204	
Remain	-	-	-				0.0111	
Rutile	-	-	-				0.0111	
Remain							0.0000	
		-						

Table 32: % MBC mineral Content

Mineral	Mol. equivalent	Mol. weight	Weight	Weight %
Orthoclase	0.0103	557	= 5.74	5.74
Albite	0.0060	524	= 3.14	3.14
Anorthoclase	0.0004	279	= 0.11	0.11
Kaolinite	0.2811	258	= 72.52	72.52
Quartz	0.1244	60.1	= 7.48	7.48
Illumenite	0.0204	239.9	= 4.89	4.89
Rutile	0.0111	79.9	= 0.89	0.89
Total			94.77	

Table 33: Eburru Fireclay Mineral Mole Equivalent

Element Oxide	Content (wt %)	Molecular weight	Mole equivalent
SiO_2	60.07	60.1	0.9995
Al_2O_3	24.00	102.0	0.2353
Fe_2O_3	2.45	160.0	0.0153
CaO	0.25	56.1	0.0046
Na_2O	0.15	62.0	0.0024
K_2O	0.17	94.2	0.0018
MgO	0.19	40.3	0.0047
TiO_2	2.03	79.9	0.0254
MnO	0.20	86.9	0.0023
LOI	9.86	18.0	0.5478

Table 34: Eburru Fireclay Mineral Mole Content

	SiO_2	Al_2O_3	Fe_2O_3	CaO	K_2O	Na_2O	TiO_2	H_2O
Mole equivalent	0.9995	0.2353	0.0153	0.0046	0.0018	0.0024	0.0254	0.5478
0.0018 mol orthoclase	0.0108	0.0018			0.0018			
Remain	0.9887	0.2335			-			
0.0024 mol Albite	0.0144	0.0024				0.0024		
Remain	0.9743	0.2311				-		
0.0046 mol Anorthite	0.0092	0.0046		0.0046				
Remain	0.9651	0.2265		--				
0.2265 kaolinite	0.4530	0.2265						0.4530
Remain	0.5121	-						0.0948
0.5121 mol quartz	0.5121							
Remain	-							
0.0153 mol limonite			0.0153					0.0153
Remain			-					0.0795
0.0795 mol water								0.0795
Remain								0.0000

Table 34: Eburru Fireclay Mineral Mole Content

	SiO_2	Al_2O_3	Fe_2O_3	CaO	K_2O	Na_2O	TiO_2	H_2O
Mole equivalent	0.9995	0.2353	0.0153	0.0046	0.0018	0.0024	0.0254	0.5478
0.0018 mol orthoclase	0.0108	0.0018			0.0018			
Remain	0.9887	0.2335			-			
0.0024 mol Albite	0.0144	0.0024				0.0024		
Remain	0.9743	0.2311				-		
0.0046 mol Anorthite	0.0092	0.0046		0.0046				
Remain	0.9651	0.2265		--				
0.2265 kaolinite	0.4530	0.2265						0.4530
Remain	0.5121	-						0.0948
0.5121 mol quartz	0.5121							
Remain	-							
0.0153 mol limonite			0.0153					0.0153
Remain			-					0.0795
0.0795 mol water								0.0795
Remain								0.0000

Table 35: Eburru Fireclay % Mineral Phases

Mineral	Mol. equivalent	Mol. weight	Weight	Weight %
Orthoclase	0.0018	557	= 1.00	1.00
Albite	0.0024	524	= 1.26	1.26
Anorthoclase	0.0046	279	= 1.28	1.28
Kaolinite	0.2265	258	= 58.47	58.47
Quartz	0.5121	60.1	= 30.78	30.78
Limonite	0.0153	178.0	= 2.72	2.72
Water	0.0795	18.0	= 1.43	1.43
Total			96.94	